Magnetic Thin Films For Spintronic Memory

by

Parnika Agrawal

B.Tech., Indian Institute of Technology, Kanpur (2012)

Submitted to the Department of Materials Science and Engineering
in partial fulfillment of the requirements for the degree of

Doctor of Philosophy in Materials Science and Engineering

at the

MASSACHUSETTS INSTITUTE OF TECHNOLOGY

February 2018

Signature redacted

Author .....
Department of Materials Science and Engineering
September 25, 2017

Signature redacted

Certified by .....
Geoffrey S.D. Beach
Associate Professor
Thesis Supervisor

Signature redacted

Accepted by .....
Donald R. Sadoway
Chairman, Department Committee on Graduate Theses

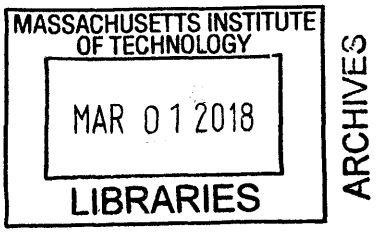

To Papa who inculcated curiosity as a way of life and Ma who encouraged me to create my own paths

Magnetic Thin Films For Spintronic Memory

by

Parnika Agrawal

Submitted to the Department of Materials Science and Engineering
on September 25, 2017, in partial fulfillment of the
requirements for the degree of
Doctor of Philosophy in Materials Science and Engineering

Abstract

Domain walls are regions of spatially non-uniform magnetizations in magnetic materials. They form the boundaries between two or more uniformly magnetized regions called domains. Skyrmions are circular magnetic domains with chiral domain walls that are interesting due to their stability and potential for fast motion. These spin structures can be used to encode 0s and 1s in spintronic memory. Chiral domain walls and skyrmions have been seen in magnetic thin films sandwiched between non-identical non-magnetic materials which have high spin-orbit coupling and Dzyaloshinskii-Moriya interaction. An optimization of the different physical interactions involved in magnetic thin films can result in stripe and labyrinth domain patterns which can then be transformed into skyrmion lattices.

In this thesis, we present a detailed understanding of single- and multi-layer magnetic thin films along with all the relevant physical interactions. We show that in-plane magnetic fields stabilize domain walls in thin films with Dzyaloshinskii-Moriya interaction. The application of in-plane magnetic fields is shown to create multi-domain patterns in films where the ground state is uniform magnetization. Next, we study the formation of stripe and labyrinth domain patterns in magnetic films. The domain widths obtained are compared with the predictions of several theoretical models developed over the last 50 years. The appropriate model that works for thin films with strong Dzyaloshinskii-Moriya interaction is identified with the help of micromagnetic simulations. The appropriate model includes effects of finite domain wall width and volume charges inside Néel domain walls. This model is then used to measure the Dzyaloshinskii-Moriya interaction in experimentally grown magnetic thin films. Thereafter, we highlight the role of other design variables such as the thickness of magnetic and non-magnetic layers, the choice of materials, and the role of geometrical confinement in controlling the length scale of the domain patterns. This work generates the necessary knowledge and develops techniques to engineer chiral spin textures in single- and multi-layer magnetic thin films.

Thesis Supervisor: Geoffrey S.D. Beach
Title: Associate Professor

Acknowledgments

A PhD is a long journey and it cannot be made alone. The people around me have played a huge part in helping me grow as a researcher and as a person and I would like to thank everyone who contributed to my progress.

Thank You very much, Geoff, for inviting me with open arms into your group and research field. Even though I had not considered magnetism as my focus area when I entered MIT, I was extremely inspired by your passion for the subject that you also brought with you to the 3.23 classes. I have learnt a lot from working with you - everything about spintronics, how to do design experiments, formulate hypotheses, ask the right questions, and also practical things like making good presentations and writing effective papers. As Morpheus says in the Matrix, "I'm trying to free your mind, Neo. But I can only show you the door. You're the one that has to walk through it.", you have truly developed in me capabilities of opening many doors, and I am extremely grateful to you for that.

I would like to thank my committee members, Prof Ross and Prof Gradečak, for their guidance and support for the last five years. Prof Ross, your class on Magnetism was my first in-depth exposure to the field and gave me a lot of research ideas. Your insightful questions have always made me look more deeply at my work and consider possibilities that I hadn't imagined. Prof Gradečak, I really enjoyed your imaging class. Learning about the multitude of ways to look at atoms and their properties was very inspiring and kindled my interest for Magnetic Force Microscopy, which I ended up using heavily in my research. Thanks, Prof Ross and Prof Gradečak, also for being excellent role models as trailblazing women in science.

The Beach Group has been an integral part of my PhD experience. Thanks to Satoru Emori, Liz (Elizabeth Rapoport), Uwe Bauer and Shwoo (Seonghoon Woo) for initiating me into the group and teaching me several experimental techniques and best practices. Thanks to Min ae Ouk, Sarah Schlotter, Lucas Caretta, Max Mann, Aik Jun Tan, Ivan Lemesh, Mantao Huang, Sasha Churikova, Chi-Feng Pai, Can Onur Avci, Felix Büttner, and Kohei Ueda for the countless research discussions,

brainstorming sessions, group retreats and musings over where Geoff might be traveling. Thanks in particular to Sarah for growing the wedge samples for me that made a lot of interesting research in this thesis possible, and for proof-reading this thesis. Thanks to Felix for the guidance on writing papers, making effective presentations and for collaboration on the measurement of DMI project.

Thanks to David Bono for his vast knowledge and willingness to help build things. Thanks for helping out with designing electromagnets, stage, fixing the VSM and setting up experiments for Undergraduate Teaching Lab. Your tinkering spirit is an inspiration! Thanks to Mike Tarkanian, Chris Di Perna and Franklin Hobbs for teaching me how to use the machine shop. Thanks to Tara Fadenrecht for showing me how to be creative and artistic with metal working. You made hammering fun for me! Thanks to Charlie Settens for patiently teaching me about X-Ray measurements and Libby Shaw for her expertise in Magnetic Force Microscopy. Thanks to DMSE staff members Angelita Mireles, Elissa Haverty and Julia Hollingsworth and Gina Franzetta from CMSE for always promptly helping out with logistics and reminding me to fill out all the paperwork in time.

I have been blessed to have a large extended family in the US who helped me out whenever I was feeling homesick. Thank You Hridaya Uncle and Kusum Aunty for being my first guardians in Boston and for easing my transition into the US culture. Thank You Nibha Aunty and Umesh Uncle for taking care of me like your own kid and for all the yummy food at Diwali celebrations. Many thanks to Anita Chachi and Narayan Uncle for their infinite love and support. Thanks to Anjali Didi, Vibhor Jeeju, Cheena Didi, Khajan Jeeju, Ashu Mama, Priyanka Mami, Charu Mausi, Ruchika Didi, Saurabh Jeeju, Ruchi Didi and Dhruv Jeeju for providing me for the home-away-from-home feeling.

Rushabh and Sanket, studying with you for classes and qualifiers and navigating through the maze of the department was a lot of fun. Thanks to my friends from Indian Students' Association at MIT for sharing my passion for India, Bollywood and dance - Radhika, Sameer, Divya, Vaibhav, Siva, Ankur, Himani, Rasha, Rinal, Krishna, and Pawan. Thanks to Siva for his wisdom on life as a PhD student

at MIT. Thanks to Yash, Devendra, Pritish and Apoorvaa for the many hangouts, board games and 'chai pe charchas' at 8D. Special thanks to Yash for boosting me up in my lowest moments and encouraging me to workout every morning. Thanks to Devendra for teaching me various sports. Working as part of the Tang Hall Residents' Association was an enriching experience. Through this, I got to meet several wonderful inspirational people. I am grateful for the friendship of Dawn Anderson, who has been a wise sounding board and support over the course of many a tough moments. Thanks to Florian Feppon for very interesting conversations in English, Hindi and French about math, meringue, yoga, fasting, traveling, and the sounds in different languages. Thanks to Shubhayu for sharing the finer pleasures of life - music, art, nature, poetry, philosophy, physics and literature. Thanks to Bhavna, Maike and Terez for being there for me when I was lost and cheering me up with your love and grace. Thanks to Viral and Dragos for making hiking fun for me. Akhilesh and Vidhi, you have been such a huge support during my thesis writing phase making sure I ate and exercised and didn't lose my sanity. Thanks to Rameech for your fun attitude and reminding me to count my blessings. Thanks to the fun gang at IBM - Josh, Marianna, Maria, Zi, Qiancheng, Adham and Arzoo for some very memorable trips. Thanks a lot to my friends from IIT-K, Surbhi, Asmita, Tanya, Harshal, Ardhendhu, Anusha, Swetha, Sankalp and Siddharth, who have stuck by me all these years despite the long distances.

A big credit for my happiness and confidence goes to Navin Bhatera for having faith in my capabilities and helping me out with all kinds of support. Finally, I would like to thank my family for their unconditional endless forgiving nurturing love.

Contents

Nomenclature

List of Abbreviations

AFM Atomic Force Microscopy

DMI Dzyaloshinskii-Moriya Interaction

EBL Electron Beam Lithography

MFM Magnetic Force Microscopy

MIBK Methyl IsoButyl Ketone

MOKE Magneto-Optic Kerr Effect

NMP N-Methyl-2-pyrrolidone

PMA Perpendicular Magnetic Anisotropy

PMMA Poly-Methy Methacrylate

SHE Spin Hall Effect

SOC Spin Orbit Coupling

STXM Scanning Transmission X-ray Microscopy

TI Topological Insulators

VSM Vibrating Sample Magnetometry

List of Symbols

$\boldsymbol{S}$	Spin magnetic moment
Δ	Domain wall width
λ	Thickness of each repeat in a multi-layer film
$\mathcal{E}_s$	Surface stray field energy per unit volume of magnetic film
$\mathcal{E}_{tot}$	Total energy per unit volume of magnetic film
$\mathcal{E}_v$	Volume stray field energy per unit volume of magnetic film
μ_0	Vacuum permeability
ψ	Domain wall angle
σ	Domain wall energy per unit area
$\vec{H}$	Magnetic field
A_{ex}	Exchange stiffness
A'_{ex}	Scaled exchange stiffness for multi-layer film
D	Dzyaloshinskii-Moriya interaction parameter
d	Domain width in demagnetized state
D'	Scaled DMI parameter for multi-layer film
D_{thr}	Threshold DMI for Néel walls
E_d	Demagnetizing energy
E_{DW}	Domain wall energy
f	Scaling factor
H_C	Coercivity or coercive field

H_K Anisotropy field

H_D Effective DMI field

H_X Magnetic field parallel to film plane

H_Z Magnetic field perpendicular to film plane

K'_U Scaled anisotropy for multi-layer film

$K_\perp$ Bloch-Néel transverse anisotropy

K_{eff} Effective anisotropy

K_{hys} Anisotropy energy measured from area between easy- and hard- axes hysteresis loops

K_S Surface anisotropy

K_U Uniaxial anisotropy

K_V Volume anisotropy

M_i Magnetic moment after demagnetization

M_R Remanence or remanent magnetization

M'_S Scaled saturation magnetization for multi-layer film

M_Z Component of magnetic moment perpendicular to film plane

M_S Saturation magnetization

N Number of repeats

Q Quality factor

T Thickness of each magnetic layer in a multi-layer film

t Total thickness of magnetic film

Ar	Argon gas
Co	Cobalt
CoFeB	Cobalt-Iron-Boron
Fe	Iron
GdOx	Gadolinium oxide
Ir	Iridium
MgO	Magnesium oxide
Ni	Nickel
Pt	Platinum
Si	Silicon
SiO_2	Silicon dioxide
Ta	Tantalum
W	Tungsten

List of Figures

Chapter 1

Introduction

This chapter serves as an introduction to the field of spintronics and highlights the importance of studying magnetic multi-layer films for applications in magnetic memory and logic devices. The scope of this thesis along with the specific questions answered are outlined.

1.1 Motivation

The physical realization of any computer memory device is based on the existence of two distinct physical states that can be used to encode 0 and 1, and a deterministic way to switch between these two states. A magnet with its distinct north and south pole represents an excellent system for use in memory devices. Traditionally, magnetic tapes, floppy disks and hard disks have used magnetic materials to store information. These devices are limited in their speeds of operation by the requirement to physically move the read/write head with respect to the bit-storing magnetic medium. What if there was a device where one could move a series of bits inside the magnetic medium without mechanically moving either the read/write head or the medium itself? The speed of operation in such a device would be determined by the speed of electron spins inside a magnetic material, which is orders of magnitude higher than speeds achievable by mechanical motion of objects. This is the fundamental motivation behind the development of spintronic memory which is based on

the concept of manipulation of electron spins with a variety of physical interactions such as exchange and Dzyaloshinskii-Moriya interaction within the magnetic materials as well as external stimuli such as currents, temperature, electric and magnetic fields. Other than speed, spintronic memory technology offers several other advantages [1]–[6] over conventional memory technologies. It is a non-volatile technology, i.e., it does not require any external energy to maintain its state and preserves its state even after the device is turned off. Spintronic memory also offers a high density of storage comparable to currently used solid-state memory.

In spintronic memory, chiral spin textures such as skyrmions and chiral domain walls (Figure 2-8) are used to encode bits. Until a few years ago, the concept of such a device was based on domain walls and the key bottle neck was the realization of fast current-induced domain wall motion [7]–[10]. In the last few years, the focus has shifted to creation and manipulation of skyrmions. Skyrmions are circular regions of chiral spin textures in magnetic thin films that offer several advantages over magnetic domain walls, such as a smaller size than magnetic domains, higher mobility, and topological protection [11]–[17]. Figure 1-1 shows a schematic of skyrmion-based racetrack memory device. The direction of spins (up or down) at the skyrmion core represents 0s or 1s.

The key requirement of realizing a spintronic memory device is to understand the formation of chiral spin structures such as skyrmions and chiral domain walls in magnetic materials, as well as to develop the ability to create and move these spin structures in a reliable and efficient manner. Earlier work showed that skyrmions could be found only in bulk single crystals [18] and single-crystalline thin films [19], [20]. Recent work, however, has also observed chiral domain walls [21], [22] and skyrmions [11]–[13] in poly-crystalline sputtered magnetic thin films with sizable perpendicular magnetic anisotropy (PMA, Section 2.1.2) and Dzyaloshinskii-Moriya interaction (DMI, Section 2.1.6). Both of these interactions are particularly strong in asymmetric thin films of ferromagnetic materials sandwiched between non-magnetic materials with high spin orbit coupling (SOC, Section 2.1.5) such as heavy metals. Since polycrystalline thin films are readily grown in lab and industry via physical va-

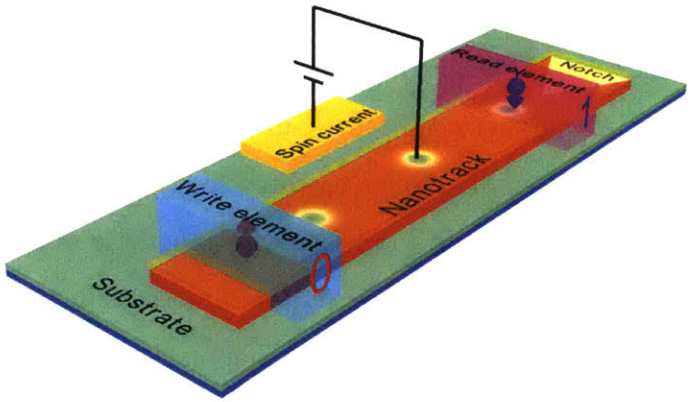

Figure 1-1: Skyrmion-based racetrack memory storage device. The small circular domains on the nanotrack are skyrmions. Opposite spin polarities represent 0 and 1. Reproduced from [23].

por deposition techniques like sputtering, this finding makes the materials of interest more accessible and scalable.

In this thesis, we look at magnetic thin films, both single- and multi-layered, which are of interest for skyrmionic memory applications. We explain what makes these materials exhibit chiral spin structures and how we can understand the interaction of different physical energy terms to predict the length scales of chiral spin textures observed in these materials. We then develop a framework to control the relative strengths of these physical interactions in the system to engineer magnetic thin films with desirable properties.

1.2 Scope of this thesis

We start with laying the groundwork to talk about the materials of interest, magnetic thin films, in Chapter 2. The fundamental physical concepts involved in magnetic thin films are introduced, starting with the origin of ferromagnetism in materials and other interesting phenomena like perpendicular magnetic anisotropy, spin-orbit coupling and Dzyaloshinskii-Moriya interaction. These interactions become important in thin films with high surface area to volume ratio and give rise to chiral spin textures which are required for realizing spintronic memory devices. This chapter ends with

identifying magnetic thin films as the materials of interest and highlights the key attributes in these films. Chapter 3 then presents an overview of the fabrication methods that were used in growing magnetic thin films and creating sub-micrometer sized patterns in them, characterization techniques used to investigate the magnetic properties of thin films, and imaging technique to observe the magnetic domain patterns. This chapter also explains the micromagnetic simulation methods used to understand the basis of the experimental results obtained. In Chapter 4, we describe a technique to create metastable multi-domain patterns in single and multi-layered magnetic films, which we later use in Chapters 5 and 6. In Chapter 5, we look in detail at magnetic thin films and go over the different theoretical models to explain domain patterns in thin films. We then show how the Dzyaloshinskii-Moriya interaction parameter, which represents the strength of chirality of spins in magnetic films, can be measured in experimental magnetic multi-layer films using the models outlined earlier. Finally, in Chapter 6, we map out the entire parameter space accessible to materials scientists designing multi-layer magnetic films and highlight the role of each design variable in controlling the size of magnetic domains. Chapter 7 summarizes the results of this thesis and gives an outlook for future work.

Chapter 2

Background

This chapter describes the fundamental physical concepts relevant in magnetic materials for spintronic memory devices and introduces magnetic thin films as the materials of interest. The key attributes of magnetic thin films that make them suitable for spintronic memory are highlighted.

2.1 Relevant physical concepts

2.1.1 Ferromagnetism

What makes a material magnetic? Why are there only a few magnetic elements in the periodic table? The answer lies in the behavior of electrons within a material. One might recall from high school physics that electrons have spin and orbital angular momenta that affect their arrangement within the various shells in an atom. The spin angular momentum is quantized and can take only two values, parallel and anti-parallel to an external magnetic field. It is the phenomenon of collective alignment of spin angular momenta over several electrons in a material that gives rise to magnetism. The presence of unpaired electrons in an atom gives rise to paramagnetic behavior (alignment of spins parallel to external magnetic field) as opposed to diamagnetic behavior (repulsion of external magnetic field) displayed by a majority of elements with paired electrons. However, in some materials (ferromagnets, ferrimagnets and

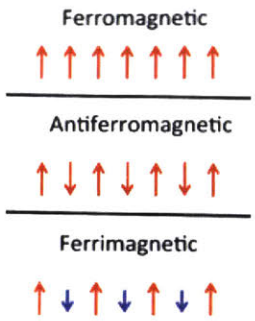

Figure 2-1: Illustration of alignment of magnetic moments in different kinds of magnetic materials.[1]

anti-ferromagnets), the electrons on neighboring atoms interact with each other to produce a long-range ordering that gives rise to an intrinsic magnetic field. This long-range ordering gives rise to spontaneous magnetization in these materials. The difference between ferro-, ferri- and antiferromagnets lies in the arrangement of their atoms. In ferromagnets, magnetic moments of all atoms in a region align in parallel to produce a net magnetic field. In antiferromagnets, the atoms are arranged such that the magnetic moments of neighboring atoms are aligned anti-parallel so there is no net external magnetic field. In ferrimagnets, there is partial cancellation of magnetic moments. There are usually two kinds of atoms with opposite but unequal magnetic moments, as a result of which there exists an overall magnetic field but which is weaker than that in ferromagnets. The intrinsic magnetic energy that comes from the interaction between electrons in neighboring atoms in magnetic materials is called exchange energy and is denoted by J. For ferromagnets, this energy is positive and causes the neighboring magnetic moments to be aligned parallel to each other while for antiferromagnets, the situation is reversed and anti-parallel alignment on neighboring atoms is preferred. This energy is measured macroscopically in magnetic materials through the exchange stiffness parameter A_{ex} which takes the value of $1-2\times10^{11}\,J/m$ in most ferromagnets [24]. For the purpose of this thesis, we will focus only on ferromagnetic materials and refer to them only as magnetic materials.

[1]Source: https://chem.libretexts.org/Textbook_Maps/Inorganic_Chemistry_Textbook_Maps/Map%3A_Inorganic_Chemistry_(Wikibook)/Chapter_06%3A_Metals_and_Alloys_-_Structure%2C_Bonding%2C_Electronic_and_Magnetic_Properties/6.7%3A_Ferro-%2C_ferri-_and_antiferromagnetism

2.1.2 Magnetic anisotropy

Magnetic anisotropy is the property of magnetic materials to have a preferred direction of magnetization. The preferred direction of magnetization is known as the easy axis while hard axes are any directions not along the easy axis. Anisotropy in magnetic materials could come from the underlying crystal structure (magnetocrystalline), strain (magnetoelastic), interfacial interactions (surface anisotropy), or sample shape (magnetostatic). In this thesis, we will largely focus on magnetic thin films (thickness of $\sim$ 1 nm) with very large surface area to volume ratios. The dominant anisotropy in these films is the interfacial anisotropy which makes the total magnetic moment point perpendicular to the film plane. The total anisotropy energy density K_U in thin films is strongly correlated with the thickness of the film[2]. The two are related as:

$$K_U = K_V + 2\frac{K_S}{t} \tag{2.1}$$

where K_V is the volume anisotropy energy density which consists of magnetocrystalline, magnetoelastic and magnetostatic contributions. K_S is the surface anisotropy energy per unit area which arises from spin-orbit interactions between the surface atoms of magnetic material and the atoms of the adjacent materials. The factor of 2 comes because of two interfaces (top and bottom) of the magnetic thin film. For thicker films, the bulk contribution to total anisotropy energy is stronger, hence the preferred direction of magnetization is in the plane of film. As the thickness of magnetic film decreases, the contribution of surface anisotropy to total anisotropy increases. Therefore a perpendicular magnetization is preferred below a threshold thickness. Perpendicular magnetic anisotropy (PMA) is highly desirable in magnetic recording media since it enables multiple bits to be packed in a small area on the recording disk [25]. Figure 2-2 shows the variation of total anisotropy energy per unit area with change in thickness of a cobalt film with threshold film thickness around 13 Å. As we will see later in this chapter as well as in Chapter 5 and Chapter 6, this

[2]Note that total anisotropy energy density is often represented in the literature as K_{eff} and K_U is reserved for magnetocrystaline anisotropy only. However we refrain from using this terminology to avoid confusion with K_{eff} in stripe-domain models discussed in Chapter 5.

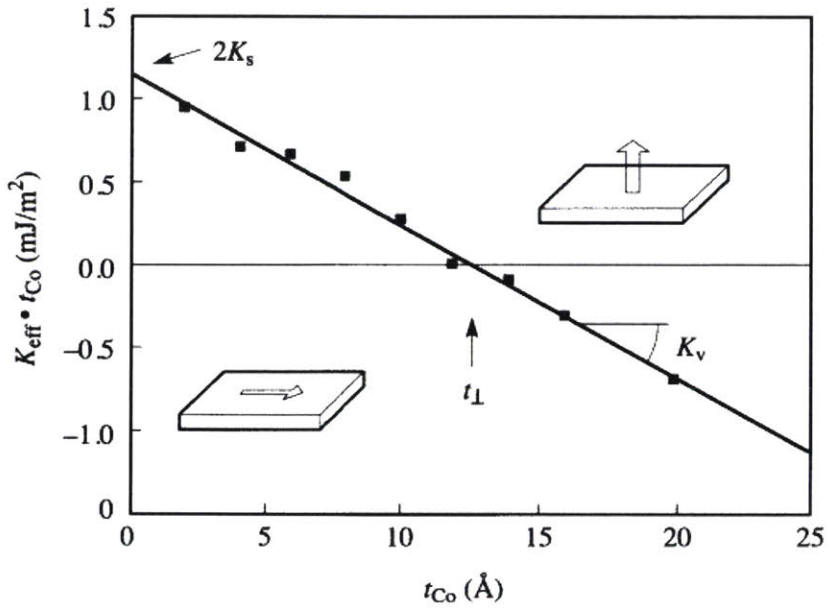

Figure 2-2: Effective anisotropy energy density per unit area as a function of magnetic film thickness. Adapted from [26].

anisotropy energy plays a very important role in determining several lengthscales in the magnetic films such as magnetic domain width, domain wall width and skyrmion diameter. Therefore, an accurate estimation of anisotropy energy is critical to determining the length scales in the system. Section 2.1.7 describes several methods of measuring anisotropy energy and the errors associated with each of them.

2.1.3 Magnetostatics and domain formation

A bar magnet can be seen to be composed of several tiny magnets with the north pole of one tiny magnet next to the south pole of the neighboring tiny magnet, such that their magnetic field lines are aligned. At the surface of the bar magnet, however, there are no neighboring tiny magnets, and we are left with free magnetic poles, north and south, at either end of the bar magnet. Magnetostatic energy, also known as demagnetizing energy or stray field energy, is the magnetic potential energy or the amount of work required for the magnetic poles to exist in the internal magnetic field [24]. The internal magnetic field is given by $-\mu_0\vec{M}$. The magnetostatic energy per

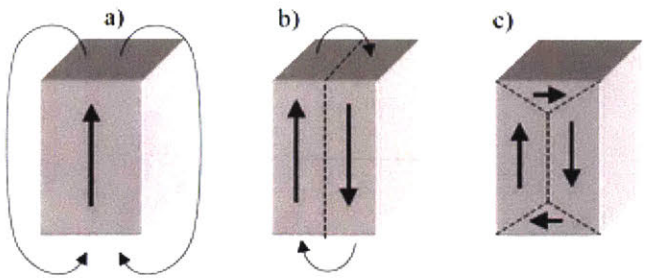

Figure 2-3: The magnetization inside a bar of iron getting rearranged from a-c into smaller domains to minimize stray fields (curvy lines outside the bar with arrows) at the expense of introducing domain walls.[3]

unit volume then is

$$U = -\vec{M} \cdot \vec{H} = -\frac{\mu_0 M_s^2}{2} \tag{2.2}$$

where M_S is the saturation magnetization per unit volume, which is the total magnetic moment when all internal moments are aligned in parallel.

External stray field energy associated with a magnet can be minimized by lowering the density of free poles. That is why, in a large piece of magnet, the surfaces with the smallest area are chosen as the free poles. Further lowering of energy in the system is achieved by the formation of magnetic domains within the bulk. A magnetic domain is a region within a magnetic material within which all magnetic moments are aligned parallel to each other. If all magnetic domains are aligned parallel to each other, there is a strong external stray field energy (magnetostatic energy) associated with the material. It is therefore energetically favorable for the system to arrange the magnetic domains such that there is no net magnetization and hence no external stray field as shown in Figure 2-3. Domain formation in a material comes at the cost of introduction of domain walls in the system which are described in the next section.

2.1.4 Domain walls

Domain walls are planar regions between two neighboring magnetic domains through which the magnetization changes from one direction to another (Figure 2-4). The width of the region is called the domain wall width and is denoted by Δ. The exchange

[3]Source: `https://commons.wikimedia.org/wiki/File:Powstawanie_domen_by_Zureks.png`

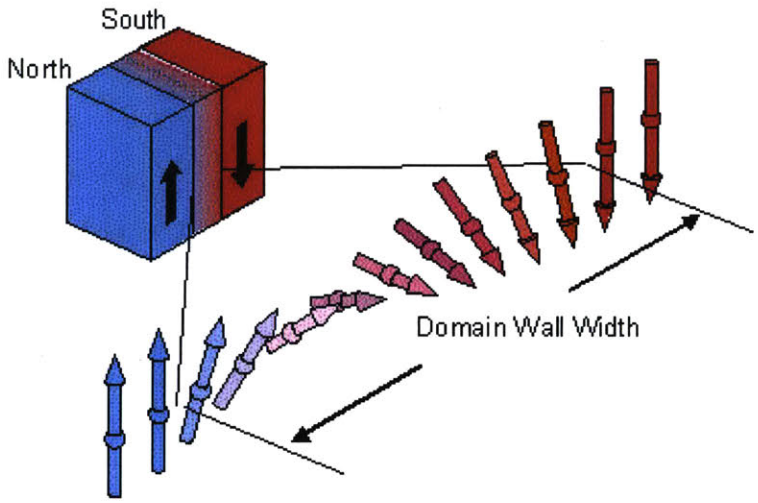

Figure 2-4: 180° domain wall in a bar of iron. [4]

energy (Section 2.1.1) prefers to minimize the angle between neighboring magnetic moments inside a domain wall thereby preferring a larger domain wall width. The anisotropy energy (Section 2.1.2), on the other hand, prefers to minimize the number of magnetic moments that are not aligned with the easy axis, and therefore prefers a narrow domain wall. The magnetic moments inside the domain wall must fight both these energies. Thus, the energy of formation of a domain wall per unit area σ is given by

$$\sigma = 4\sqrt{A_{ex}K_{eff}} \tag{2.3}$$

K_{eff} includes contributions from K_U as well as magnetostatic energy. The domain wall width Δ is given by

$$\Delta = 2\sqrt{\frac{A_{ex}}{K_{eff}}} \tag{2.4}$$

Typical domain wall energies are of the order of 0.1 mJ/m^2 [24]. The domain wall width varies from a few nm in high anisotropy materials, such as permanent magnets and ultrathin Co and CoFe films, to a few 100 nm in soft magnetic materials with low anisotropy, such as permalloy [27].

Magnetic materials can have many different kinds of domain walls, some of which are shown in Figure 2-5, depending on the film anisotropy, interface characteristics

[4]Source: `https://goo.gl/images/K5rqSz`

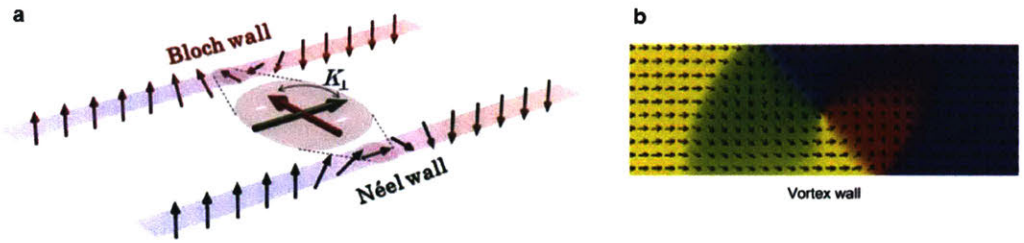

Figure 2-5: Different kinds of domain walls in magnetic thin films. a) Bloch and Néel domain walls in perpendicularly magnetized thin films. $K_\perp$ represents the domain wall anisotropy associated with volume charges due to change in the domain wall angle. Adapted from [28]. b) Vortex domain wall found in in-plane magnetized wide nanowires. Adapted from [7].

and aspect ratio of film. We describe only Bloch and Néel walls which are found in perpendicularly magnetized thin films and are the focus of this thesis.

The difference between Bloch and Néel walls lies in their axes of rotation as seen in Figure 2-5. In a Bloch wall, the magnetic moments rotate around an axis in the plane of the domain wall, while in a Néel wall the magnetic moments rotate around an axis perpendicular to the plane of the domain wall. The magnetic poles in Néel walls are much closer to each other (the distance between them is the domain wall width, Δ) than those in Bloch walls (the distance in this case is the length of domain wall which can be in cm). Thus, the stray field associated with the separation of magnetic charges by a domain wall is higher in the case of a Néel domain wall, as seen in Figure 2-6. This extra stray field energy in the volume charges of a Néel wall is represented as $K_\perp$. Bloch walls are more common in perpendicular films since they have lower energy than Néel domain walls. However, certain interactions like DMI (Section 2.1.6) can lower the energy of Néel domain walls, stabilizing their formation.

The domain wall energy calculated in Equation (2.3) is that of a Bloch domain wall. The energy of a Néel domain wall stabilized by interfacial DMI, D, is given by

$$\sigma = 4\sqrt{A_{ex}(K_{eff} + K_\perp)} + \pi D \sin(\psi) \tag{2.5}$$

where $K_\perp$ represents the extra energy associated with volume charges in a Néel domain wall compared to a Bloch domain wall, and ψ is the domain wall angle

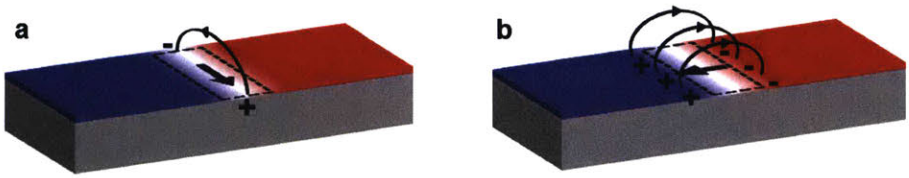

Figure 2-6: Volume charges associated with Bloch and Néel domain walls. Blue and red regions represent oppositely magnetized domains. a) Bloch wall with its effective magnetic moment in the plane of the domain wall. b) Néel wall with its effective magnetic moment perpendicular to the plane of the domain wall. Curved lines represent direction and strength of volume stray field associated with separation of magnetic charges across the domain walls.

representing deviation from Bloch wall. ψ is 0° for a Bloch wall, -90° for a Néel wall, and in between for walls showing partial Néel character.

Néel domain walls stabilized by interfacial DMI are chiral spin textures which are necessary for spintronic memory applications. Materials that exhibit these Néel domain walls are also well suited to exhibit skyrmions. Thus, looking for signatures of chiral Néel domain walls in magnetic films, via domain wall dynamics or by estimating the energy of domain walls, is a way of screening and identifying materials suitable for spintronic memory. In this thesis, we use the latter method.

2.1.5 Spin-orbit coupling

Spin-orbit coupling (SOC) is the phenomenon of interaction of spin angular momentum and orbital angular momentum of electrons which gives rise to a host of interesting physical phenomena including magnetocrystalline anisotropy (Section 2.1.2), anisotropic magnetoresistance, magnetooptic effects (Section 3.2.2), splitting of energy bands in the band diagram of electrons in solids, the Spin Hall Effect (SHE) and the Dzyaloshinskii-Moriya interaction (Section 2.1.6). To understand SOC, we must go into the rest frame of electron. In this frame, the positively charged nucleus seems to go around the electron just like the sun seems to go around the earth to an observer on earth. A moving positive charge (nucleus) appears to exert a magnetic field that creates a preferred direction of orientation of spin magnetic moment of electron. This preference of orientation of spin angular momentum with respect to the orbital

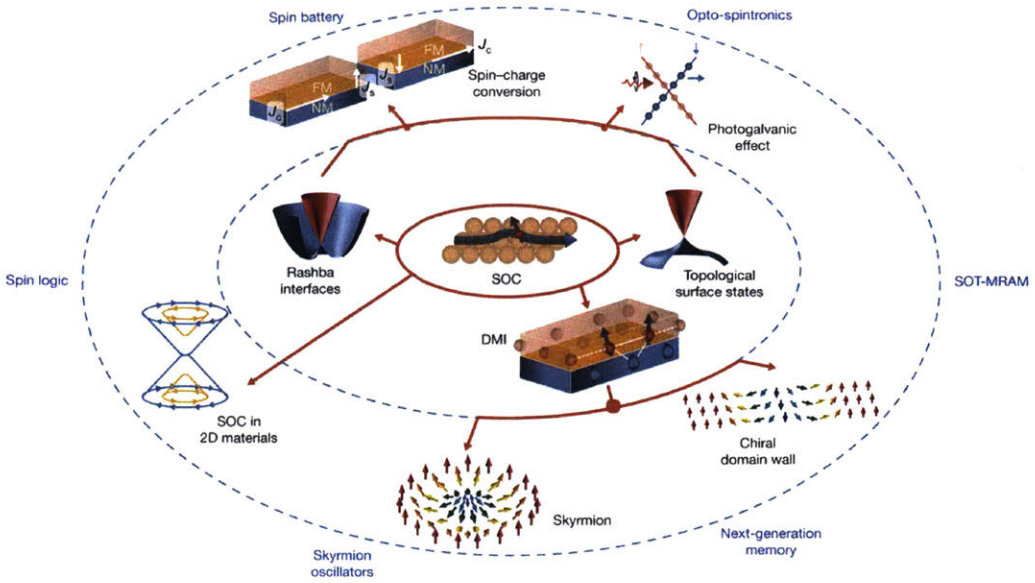

Figure 2-7: Spin-orbit coupling and the resultant physical phenomena (inner ellipse), Rashba interfaces, topological surface states and Dzyaloshinskii-Moriya interaction with applications (outer ellipse) in the creation of skyrmions and chiral domain walls, opto-spintronic effects and spin-charge conversion. Reproduced from [31].

angular momentum is SOC. The strength of SOC is around 10^{-4} eV/atom. Another way to express the strength of SOC is in terms of the magnetic field experienced by the electron, which is $\sim$ 1 Tesla [24].

The strength of spin-orbit coupling is proportional to Z^4 where Z is the nuclear charge. As Z increases, there are two effects - increase of nuclear charge as well as reduction in size of atom - both of which contribute favorably to spin-orbit coupling. The strong Z dependence of spin-orbit coupling strength makes heavy metals excellent candidates for high spin-orbit coupling. Indeed, heavy metals like Pt, Ta, Gd, Ir, and W are used extensively in magnetic multi-layers [29]–[32] as the non-magnetic layer that contributes with its high SOC and DMI. An extreme example of spin-orbit coupling is seen in 2D topological insulators, like Bi_2Se_3, where the spin and angular momentum are locked at 90^{circ} to each other allowing very efficient charge-spin conversion at the interface of topological insulators and magnetic materials [33]–[35].

2.1.6 Dzyaloshinskii-Moriya interaction

The Dzyaloshinskii-Moriya interaction (DMI) is an anti-symmetric exchange interaction [36], [37] that favors canting of neighboring spins in magnetically ordered systems (Section 2.1.1). It results in forming whirling spin structures such as chiral domain walls and skyrmions (Figure 2-8). This interaction was originally observed in bulk non-centrosymmetric crystals like MnSi [18] and later imaged via Lorentz transmission electron microscopy (TEM) in single-crystalline thin films of $Fe_{0.5}Co_{0.5}Si$ [19] and via spin-polarized scanning tunneling microscopy (STM) in a monolayer of Fe on Ir(111) surface [20]. Around the same time, chiral spin structures were also observed in polycrystalline sputtered thin films of Pt/Co [22], Ta/CoFe and Pt/CoFe [21]. This finding opened up the potential of using skyrmions in magnetic memory devices since sputtering is a widely used tool in magnetic tunnel junctions (MTJs) and allows for industrial scaling of film growth.

In thin films, DMI has been found to originate from a lack of inversion symmetry at the material interfaces and strong spin-orbit coupling (SOC). SOC comes from the heavy metal (like Pt, Ta) under-layer (as explained in Section 2.1.5) which have been traditionally used to promote PMA in magnetic thin films. The mechanism of DMI as illustrated in Figure 2-8d is a 3-site indirect exchange mechanism [38] between two atomic spins $\boldsymbol{S}_1$ and $\boldsymbol{S}_2$ with a neighboring atom having a large SOC. The DMI vector $\boldsymbol{D}_{12}$ is perpendicular to the plane of the triangle formed by these three atoms and makes the spins deviate from their perpendicular orientation (determined by anisotropy) and curl around the axis of $\boldsymbol{D}_{12}$. Inversion symmetry is broken by having two different materials on either side of the ferromagnetic film as a result of which the DMI from the bottom layer is not compensated by the DMI from the top layer.

DMI is the key factor in determining the size and shape of skyrmions in a ferromagnet and therefore characterizing it accurately is important to reliably predict the performance of the ferromagnetic material in memory devices. In Chapter 5, we will outline a simple method to calculate DMI reliably in demagnetized thin films.

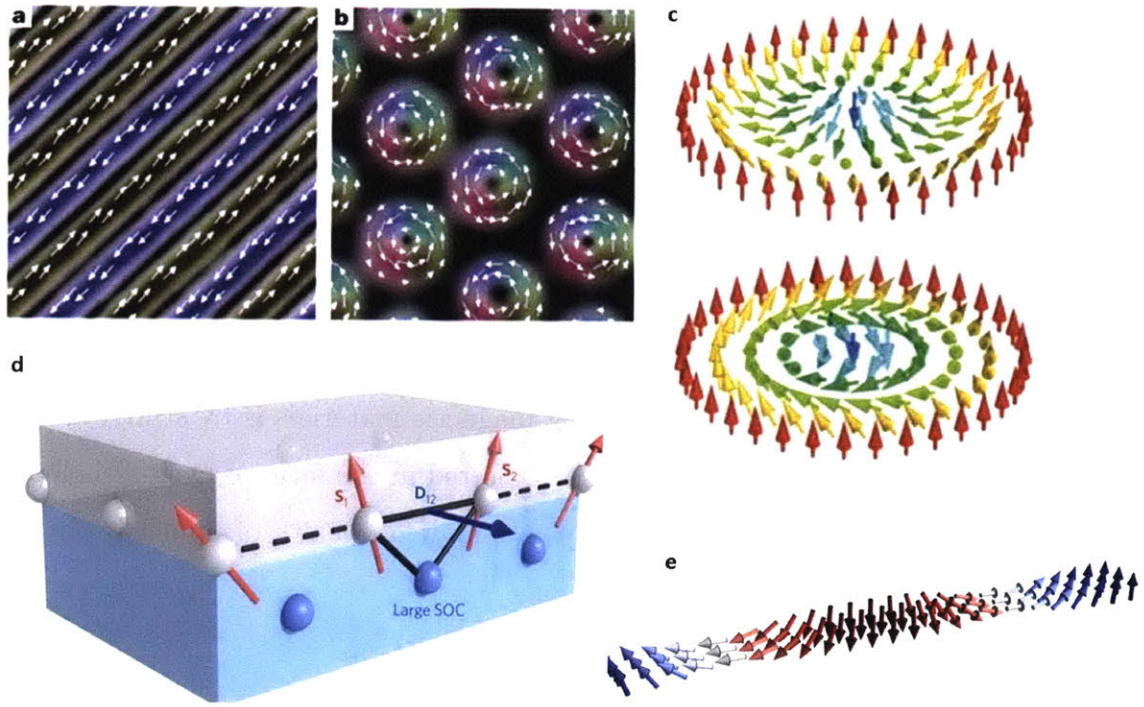

Figure 2-8: Helical (a) and skyrmion (b) structures in $Fe_{0.5}Co_{0.5}Si$ [19], c) Different skyrmion configurations in 2D ferromagnet with perpendicular magnetic anisotropy [16], d) Schematic of interfacial DMI between a ferromagnet (grey) and a metal with high spin-orbit coupling (blue). The DMI vector $\boldsymbol{D}_{12}$ acting on spins $\boldsymbol{S}_1$ and $\boldsymbol{S}_2$ in the ferromagnet makes them curl around its axis [16], e) Illustration of a chiral Néel domain wall [21].

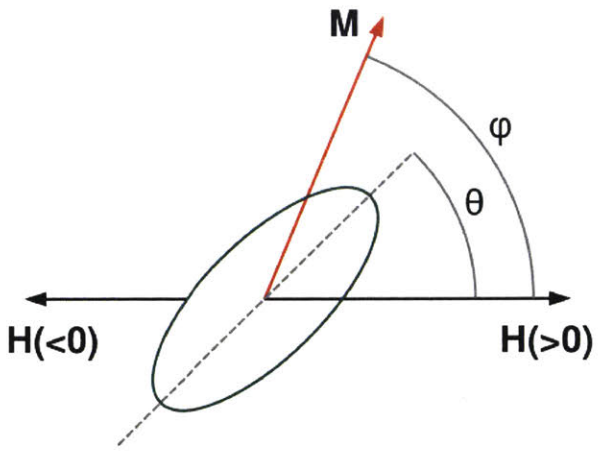

Figure 2-9: Key parameters in the Stoner-Wohlfarth model. Easy axis is shown as the dashed line. The magnetic moment $\vec{M}$ is shown by the red arrow and the direction of external magnetic field $\vec{H}$ is along the black arrows.[5]

2.1.7 Magnetic characterization via hysteresis loops

The most common method of characterizing magnetic materials is by studying their response to external magnetic fields, which is plotted in the form of hysteresis loops. This section describes what hysteresis loops are and the wealth of information that can be extracted from these loops.

Stoner-Wohlfarth model

The behavior of a single-domain magnet placed in a magnetic field is explained by the Stoner-Wohlfarth model [39]. Figure 2-9 illustrates the key variables involved in the Stoner-Wohlfarth model.

The total energy per unit volume of a single-domain magnet with magnetization $\vec{M}$ in the presence of a magnetic field $\vec{H}$ can be written as

$$E = K_U \sin(\phi - \theta)^2 - \mu_0 M H \cos(\phi) \tag{2.6}$$

where $\phi - \theta$ is the angle between $\vec{M}$ and the easy axis, ϕ is the angle between applied magnetic field $\vec{H}$ and $\vec{M}$ and μ_0 is vacuum permeability. The first term in Equa-

[5]Source: `https://commons.wikimedia.org/w/index.php?curid=11545289`

tion (2.6) comes from deviation of $\vec{M}$ from the direction of magnetic anisotropy and is proportional to the square of the angle of deviation. The second term is called the Zeeman energy and comes from interaction with the external field. The equilibrium angle of the magnetization vector can be derived from the partial derivative of total energy of Equation (2.6) with respect to ϕ.

This behavior can be pictorially seen in a hysteresis loop which is a plot of the component of magnetization vector in the direction of applied field as a function of applied field (Figure 2-10). When the field is applied parallel to the easy axis, i.e., $\theta = 0°$ (Figure 2-10a), the magnetization doesn't change until the field reaches the coercive field, or H_C, where it flips by 180°. The magnetization stays constant with further increase in field. When reducing the field, the magnetization doesn't retrace its path but stays constant until H_C is reached in the reverse direction at which point it switches again by 180°. The behavior is quite different when the field applied is along the hard axis, i.e. $\theta = 90°$ (Figure 2-10b). At zero external magnetic field, there is no component of the magnetic moment along the hard axis. As the field is increased, the component of magnetic moment along the field grows linearly in the direction of the field until the anisotropy field, or H_K, is reached. Beyond this field, the magnetic moment is completely saturated in the direction of the field. Ideally, this path is traced back on reversing the direction of the field. The magnetic moment starts tilting back towards the easy axis as the external magnetic field is reduced, thereby reducing magnetization along the field. The tilting continues until H_K is reached, this time in the reverse direction, when the magnetic moment completely points in the direction of applied field.

In real materials, the switching of magnetic moment occurs via nucleation of reverse domain and the growth of this domain with field rather than coherent switching of all the magnetic moments as predicted by Stoner-Wohlfarth model. This results in a switching field, H_{prop} (domain wall propagation field), which is typically lower than the coercive field, H_C. M_R represents the remanence or remanent magnetization, which is the magnetization that remains in the sample when external fields are removed. Experimentally measured easy- and hard- axis hysteresis loops of

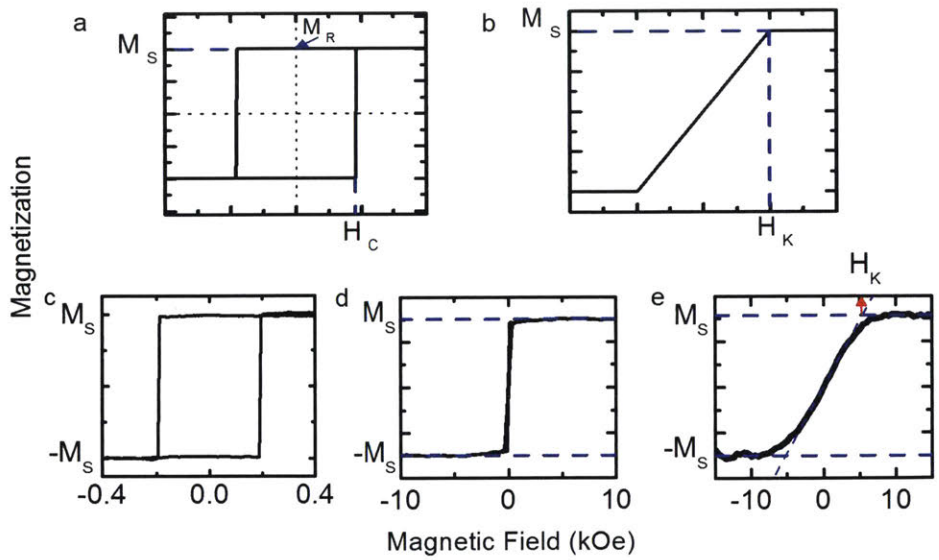

Figure 2-10: Expected easy-axis (a) and hard-axis(b) hysteresis loops from Stoner-Wohlfarth model with key parameters - saturation magnetization M_S, remanent magnetization M_R, coercive field H_C, and anisotropy field H_K marked. Measured easy-axis (c,d) and hard-axis(e) hysteresis loops for Pt/Co/GdOx films with easy-axis perpendicular to the plane of the film and hard-axis in the film plane. Loop c has been measured using Magneto-optic Kerr Polarimetry (Section 3.2.2) and loops d and e have been measured using Vibrating Sample Magnetometry (Section 3.2.1).

Pt/Co/GdOx films can be seen in Figure 2-10c-e. In this case, the film has an easy axis in the film plane and hard axis perpendicular to the film plane. Figure 2-10c shows $H_{prop} \sim 200$ Oe while Figure 2-10 e reveals H_K to be ~ 5000 Oe.

Determination of anisotropy

There are two methods of measuring effective anisotropy energy K_{eff} from hysteresis loops [26]. The first involves linear interpolation of the central part of the hard axis loops, as seen in Figure 2-10e and measuring the field at the intersection of this line with the saturation magnetization. This method comes from comparison of the hysteresis loop (Section 2.1.7e) with the expectation from the Stoner-Wohlfarth model (Figure 2-10b). The field H_K thus obtained is related to the effective anisotropy field K_{eff} as

$$H_K = -2\frac{K_{eff}}{\mu_0 M_S} \tag{2.7}$$

This is only an approximate method of estimating anisotropy and does not work for films which have a domain structure at equilibrium (thick films or multi-layer films).

The other method involves measuring the area between the easy- and hard- axis loops. This area represents the energy difference between saturating the magnetic film in the easy direction and the hard direction, which is the definition of the total anisotropy in the film. Irrespective of the equilibrium domain structure and thickness of the film, this relation is always true. The area between the loops is equal to $K_{eff} - \frac{\mu_0 M_S^2}{2}$. When using this relation to derive K_U for multilayer films, one must ensure to use the unscaled quantities, i.e. energy (area) or magnetization per unit magnetic volume (and not total volume of all the layers). Due to its universal applicability and accuracy, this method is the one primarily used in this thesis for estimating anisotropy energy from hysteresis loops.

2.2 Materials of interest - magnetic thin films

The magnetic materials relevant for memory applications are magnetic thin films which are 2D systems with thickness in nm and lateral dimensions in cm. These have been used for decades in many types of magnetic memory devices such as hard disks [40], magneto-resistive memory [41], magneto-optic memory [42], [43], ferroelectric memory [44], [45], and magnetic tunnel junctions [46], [47].

Out of plane magnetized thin films which are sandwiched between a heavy metal and an oxide, as seen in Figure 2-11, can exhibit chiral spin textures such as Néel domain walls and skyrmions, which are required for spintronic memory applications. The chiral spin textures arise due to a combination of the Dzyaloshinskii-Moriya Interaction (DMI) that comes from broken inversion symmetry and a strong spin orbit coupling in these systems [18], [21], [22], [48], [49]. In these sandwich structures, the heavy metal under-layer contributes to the strong spin orbit coupling [20], [50], [51]. The inversion symmetry is broken because the magnetic layer has different layers at its top and bottom giving rise to two different kinds of interfaces. The magnetic thin films we study in this thesis are single or multiple layers of these sandwich structures.

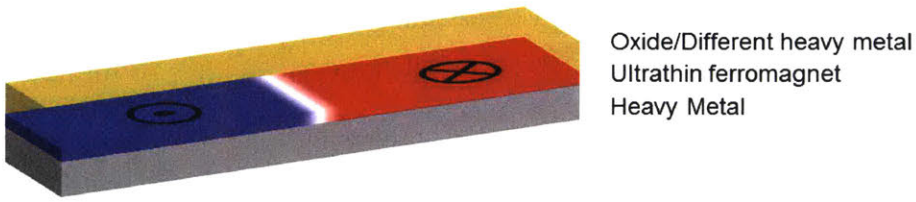

Figure 2-11: A single ultra-thin layer of magnetic film sandwiched between a heavy metal and an oxide or a different heavy metal is the basic material of study in memory applications.

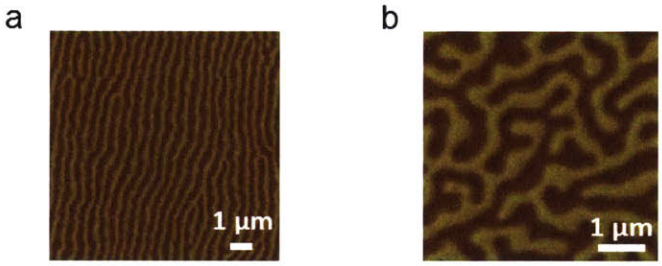

Figure 2-12: Magnetic force microscopy (MFM) images showing a) stripe and b) labyrinth domains in perpendicularly magnetized thin films. The light and dark regions represent magnetization pointing out and in to the plane of the film.

The shape anisotropy prefers magnetic thin films to have their magnetic moments pointing in the plane of the film to keep the north and south poles as far apart as possible. The surface anisotropy prefers perpendicular magnetization. Thick films see a stronger contribution from shape anisotropy and are therefore in-plane magnetized. When the thickness of a film is reduced to ≤ 1 nm, the surface to volume ratio of the film becomes high enough that the surface anisotropy coming from the top and bottom interfaces dominates, giving rise to perpendicularly magnetized thin films. Nominal hysteresis loops for perpendicularly magnetized films are shown in Figure 2-10.

For films of intermediate thickness (few nm to hundreds of µm) where Q, the ratio of perpendicular magnetic anisotropy K_U to the shape anisotropy $\frac{\mu_0 M_S^2}{2}$, is greater than 1, the magnetic films exhibit perpendicularly magnetized stripe or labyrinth domain patterns (Figure 2-12). These domain patterns have been seen in several single- and poly-crystalline films such as $BaFe_{12}O_{19}$ [52], MnBi [53] , Co [54], [55], NiFe [56], multi-layer films of Co/Pd [57] and Fe/Ni [58]. Most of these films exhibited

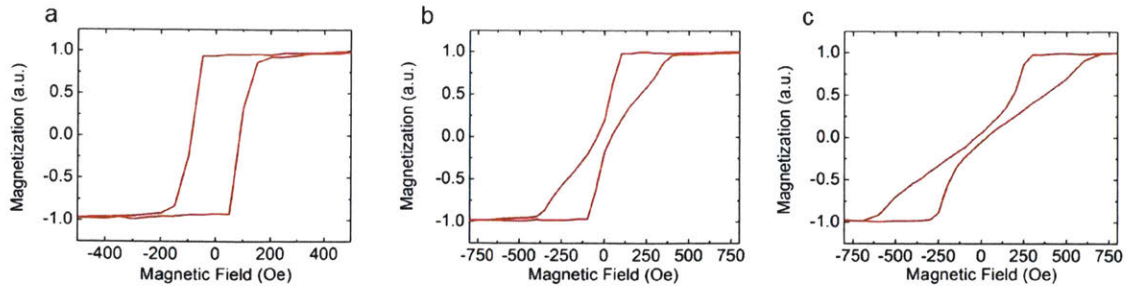

Figure 2-13: Easy axis hysteresis loops for [Pt/Co/GdOx] films of different thicknesses: a)[Pt(3 nm)/Co(0.9 nm)/GdOx(3 nm)$_5$, b)[Pt(3 nm)/Co(0.9 nm)/GdOx(3 nm)$_{15}$, c) [Pt(3 nm)/Co(1.2 nm)/GdOx(3 nm)$_{15}$].

Bloch domain walls except for the last one which highlighted, for the first time, the role of DMI in changing domain walls to Néel type, thereby changing the width of magnetic domains obtained in the film.

Figure 2-13 shows characteristic easy axis hysteresis loops for films that exhibit stripe or labyrinth domain pattern, in this case, multi-layer thin films of [Pt/Co/GdOx]. Remanence of less than 1 is an indication of formation of a multi-domain state in the absence of external fields. As the thickness of the film increases (by increase of either magnetic layer thickness or number of repeats), the saturation field increases resulting in shearing of hysteresis loops. This is because thicker films have higher demagnetizing energy giving rise to smaller domains and more domain walls in the system. The external magnetic field must be strong enough to overcome pinning of these domain walls to defects in the film. Thus higher fields are required to drive all the domain walls out of the system.

Chapter 3

Methods

This chapter describes how the materials studied in this thesis are made and characterized for their magnetic properties. The fabrication of thin films has primarily been carried out by magnetron sputtering (Section 3.1.1). The films have been patterned into dots and nano-wires with a combination of masks, Electron beam Lithography (EBL), and Ion Beam Etching (subsection 3.1.2). The last section of this chapter describes micromagnetic simulation methods (Section 3.3) that allow us to explore the magnetic behaviors of a wide variety of materials and to verify the phenomena observed experimentally.

3.1 Fabrication

3.1.1 Thin film deposition

Thin films of magnetic metals (Fe, Co, Ni), magnetic alloys (CoFe, CoFeB), non-magnetic metals (Ta, Pt) and metal oxides (MgO, GdOx) were deposited on substrates of Si(100) wafers with 50 nm thermally-grown SiO_2. The thickness of the magnetic films grown varied between 0.6 - 1.5 nm while those of non-magnetic metals and oxides varied from 1-8 nm. The films were grown via a physical vapor deposition (PVD) technique called magnetron sputtering wherein a plasma of ionized Ar gas bombards the target made out of the material which is to be deposited. The

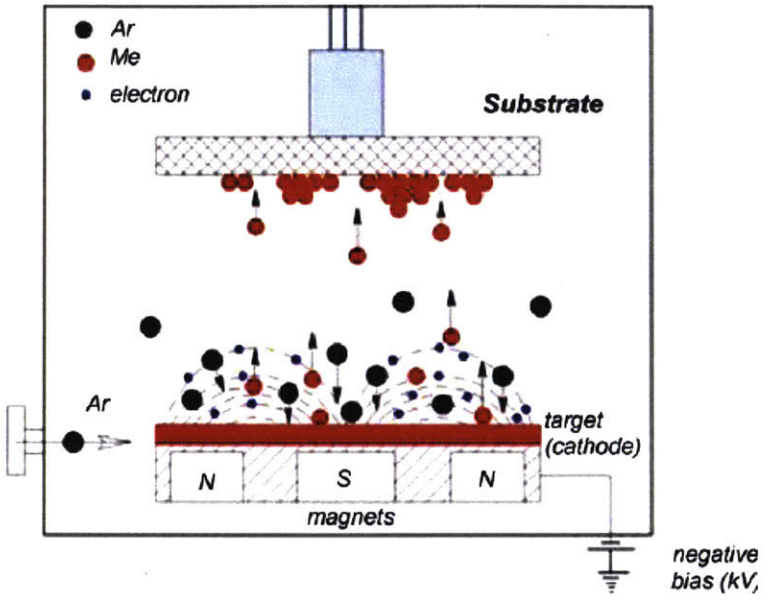

Figure 3-1: Schematic illustration of DC magnetron sputtering. The black dots represent argon gas atoms that bombard on the target made of material Me which is deposited on the susbstrate rotating at the top. Adapted from [59].

bombardment causes several atoms of the target to eject with high speeds (sputter) and cover all the nearby surfaces, one of which is the substrate. Figure 3-1 shows a schematic of the magnetron sputtering process with material Me being deposited on the substrate. In this thesis, the metal layers were deposited via DC sputtering and the oxide layers were deposited reactively under a partial pressure of high purity oxygen gas (99.993%). A uniform thickness with sub-nm homogeneity was achieved via rotation of the substrate table with a period of $\sim$ 1.7 seconds. For the wedge samples studied in Chapter 5, RF sputtering was used for the deposition of CoFeB and MgO layers.

The single and multi-layer magnetic films in Chapters 4 and 6 are deposited in the sputtering chamber in the Beach Lab. The chamber is first cleared of all gases to achieve a vacuum of the order of 10^{-7} Torr or less which is created with a combination of a mechanical pump, a turbomolecular pump and liquid nitrogen cold traps. Thereafter, ultra-high purity Ar (99.999%) gas is flowed through the chamber at a pressure of $\sim$ 2-3 mTorr at constant Ar inflow of 30.0 sccm. The wedge samples in Chapter 5 are grown in an AJA sputter system with 6 guns (3 RF and 3 DC)

placed in a confocal arrangement. The operating base pressure is around 10^{-8} Torr and the deposition is carried out $\sim$ 4 mTorr Ar pressure. The layers with uniform thickness across the wafer were deposited via rotational sputtering, while the wedge layers were deposited via stationary sputtering where the thickness of the film was inversely correlated with the distance from the target.

The thickness of the film deposited is determined by the deposition rate and the deposition time. X-ray reflectivity (XRR) is used periodically to correlate the thickness of film deposited with deposition conditions and deposition time to calculate the deposition rate.

3.1.2 Creation of sub-micron patterns in thin films

The thin films deposited in Section 3.1.1 were patterned into µm and nm sized dots via electron-beam lithography (EBL). To create patterned structures, a positive resist is first spin-coated on the substrate. A positive resist is a polymer that gets chemically modified when it comes in contact with an electron-beam. The wavelength of accelerated electrons is very small which allows for making patterns of small dimensions ($\sim$ 10 nm). The thickness of the resist spin-coated is chosen based on the thickness of the film to be deposited. For our samples, we coated poly-methy methacrylate (PMMA) of $\sim$ 100 - 200 nm. Resist-coated substrates are then baked on a hot plate at 180 - 185 °C for 90 seconds. A Raith 150 scanning electron beam (10 keV) with aperture size of between 30-120 µm was used to pattern the resist into arrays of dots. The exposed resist was then removed by developing in 3:1 (by volume) isopropanol:methyl isobutyl ketone (MIBK) solution and rinsed with isopropanol and dried with nitrogen gas. Thin films were then sputter-deposited on the patterned resist layer as described in Section 3.1.1. Excess PMMA resist was removed by immersing the sputtered sample in n-methyl-2-pyrrolidone (NMP) and ultra-sonicated. At the end, we are left with a magnetic film only in those regions where the resist had been exposed to electron-beam. Figure 3-2 shows an illustration of all the steps involved in the creation of patterned magnetic films.

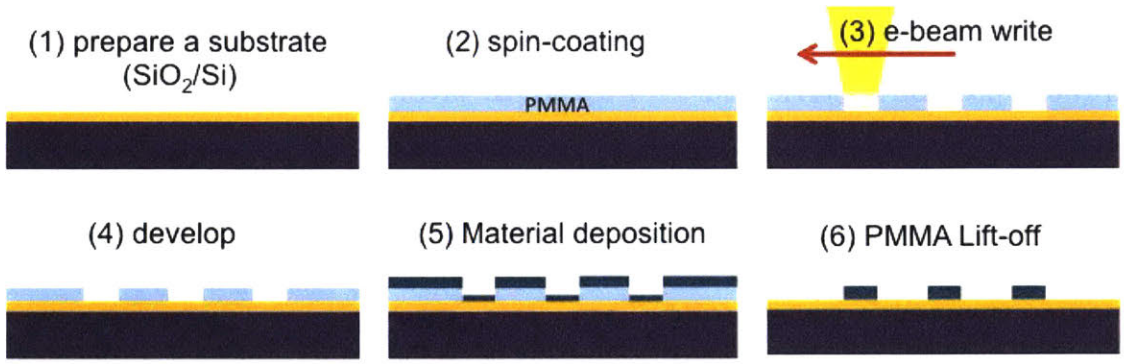

Figure 3-2: Step-by-step creation of patterned structures in magnetic thin films. Reproduced from [60].

3.2 Magnetic characterization

Magnetic characterization techniques described in this section are used to identify the key magnetic properties of materials, namely saturation magnetization M_S, a measure of the total magnetic moment per unit volume in the material; magnetic anisotropy, K_U, a measure of the preference of the magnetization to point along the easy axis of the material; coercivity, H_C, the field required to switch the magnetization by 180° along the easy axis as well as an imaging technique to visualize the magnetic domain pattern.

3.2.1 Vibrating sample magnetometry

Vibrating sample magnetometry (VSM) is a ubiquitous technique to measure magnetization as small as 10^{-5} emu [61] with high precision in magnetic films, particles and bulk pieces. The instrument is based on the Faraday's Law which states that a change in magnetic flux across a closed circuit induces an electromotive force in it, the direction of which opposes the change in flux and the magnitude of which is proportional to the rate of change of flux [62], [63]. In a VSM, a magnetic sample is oscillated at frequencies of $\sim$ 60-80 Hz with amplitudes of $<$ 1 mm between two magnetic poles that create uniform magnetic field. There are two pickup coils, one at each pole, that sense the change in flux passing through them and convert it to voltage. The coils are sensitive to only the magnetization component along their area

normal. A measurement of this component of magnetization as the magnetic field is swept gives a hysteresis loop. The sample orientation can be changed to obtain an easy or hard axis hysteresis loop.

In this thesis, we have looked at single and multiple layers of magnetic films of $\sim$ 1 nm thickness deposited on Si(100)wafers. The wafer was broken into several pieces, each piece about 1 cm $\times$ 1 cm. 3-5 pieces were then stacked on top of each other, stuck together with vacuum grease and mounted on a glass rod which was inserted in the VSM assembly. The rod was manually aligned to ensure that the magnetic sample was at the geometric center of the line connecting the center of the magnetic poles. The instrument was calibrated with a Ni sample of known magnetization. The normalized magnetization (emu/cc) was calculated by dividing the measured emu with the magnetic volume, which is calculated by multiplying known thickness of magnetic layer (from deposition parameters) with the area of the sample. The area was calculated by measuring the weight of the wafers and dividing it by the density of Si, which is the bulk constituent of the wafer, and the thickness of Si wafer. Since the hard axis hysteresis loops were used to measure anisotropy (Section 2.1.7), it was critical to ensure that the hard axis of samples was perfectly aligned with the magnetic field to ensure accurate calculation of anisotropy. This was carried out via a binary search for the closest alignment within 5 degrees on either side of the supposed hard axis until the most straight line was obtained (similar to Figure 2-10b). All measurements were carried out at room temperature.

3.2.2 Magneto-optic Kerr effect polarimetry

Magneto-optic Kerr effect (MOKE) polarimetry [64], [65] is a quick and versatile technique for measurement of hysteresis loops (Section 2.1.7) in magnetic thin films. While MOKE polarimetry cannot be used to measure the absolute magnetization in a sample, it can measure the shape of hysteresis loops accurately. In a MOKE setup, a linearly polarized laser beam is incident on the magnetic sample. The magnetization of the sample rotates the plane of polarization of the reflected light which passes through an analyzer and reaches the photo-detector. The analyzer is set up almost

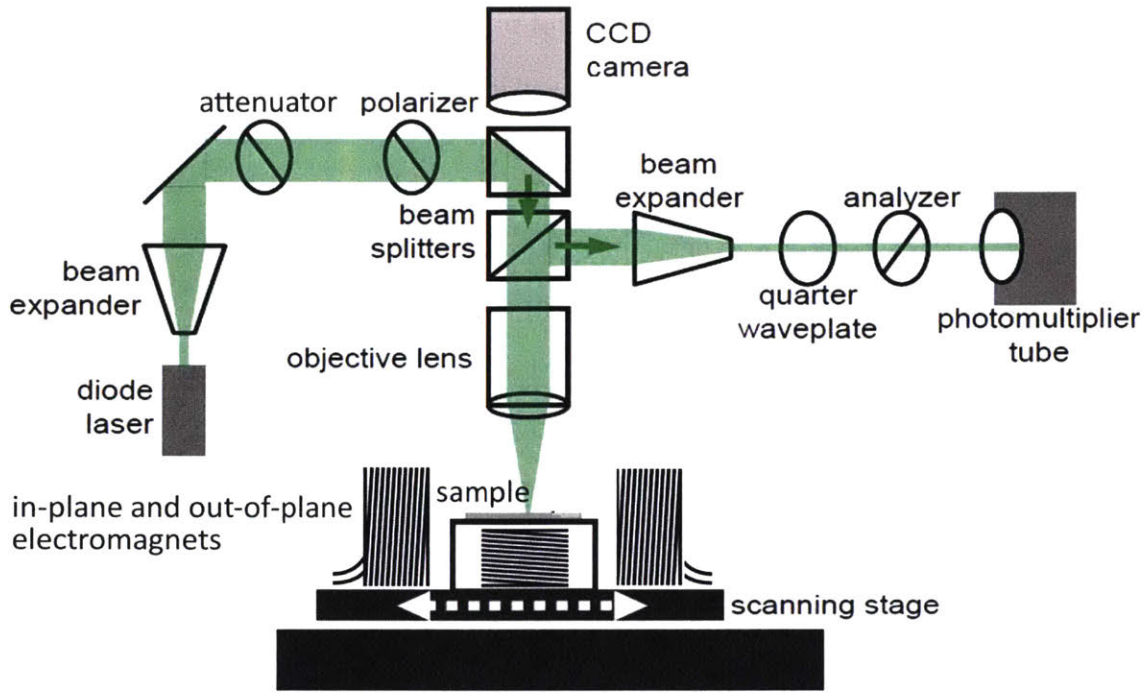

Figure 3-3: Schematic illustration of polar Magneto-optic Kerr effect polarimeter with important parts labeled. The path of laser is highlighted in green. Adapted from [66].

cross-polarized to the incident polarization and is thus sensitive to only the shift in polarization which is proportional to the magnetization of the sample. Measurement of this polarization shift is carried out as the magnetic field is swept to generate hysteresis loops.

MOKE polarimetry setups can have three configurations - transverse MOKE and longitudinal MOKE to measure magnetization in the plane of the film, and polar MOKE to measure magnetization perpendicular to the film. In particular, polar MOKE is very sensitive to out-of-plane magnetization which enables it to scan magnetic films as thin as an atomic monolayers. In this thesis, we look at only perpendicularly magnetized thin films for which we use polar MOKE to measure hsyteresis loops. The polar MOKE polarimeter used in this thesis (Figure 3-3) used collimated green laser with a spot size of $\sim$ 3 µm as the incident beam. The magnetic field was generated via iron-core electromagnets custom-fabricated for the MOKE setup. The out-of-plane magnet could apply fields up to $\sim$ 1000 Oe and the in-plane magnet up to $\sim$ 6000 Oe in pulsing mode. The setup was placed on a vibration isolated optical

table.

3.2.3 Magnetic force microscopy

Magnetic force microscopy (MFM) [67] is a magnetic-domain imaging technique that is similar to Atomic Force Microscopy (AFM) but is only sensitive to magnetic stray fields on the surface of the sample. Figure 3-4 shows a schematic of a magnetic tip scanning a magnetic film with perpendicular domains. A cantilever carrying a micrometer-sized tip with radius of 25 nm, coated with a magnetic CoCr alloy, scans at a height of $\sim$ 50 nm above the sample surface. As the tip moves across the surface of the sample, it interacts with the magnetic stray fields and gets attracted (or repelled) by it. The same tip can be used to measure surface topography (AFM mode) as well as magnetic domains (MFM mode) thus allowing correlation of domain pattern with geometrical structures. The tips can be, a) magnetized in-plane or out-of-plane, b) have low or high moment, and c) have low or high coercivity. The choice of the tip is governed by the magnetic characteristics of the sample to be imaged. The interaction of the tip with the magnetic stray field gradient causes changes in its resonant frequency (or phase) proportional to the strength of the magnetic field. These frequency changes are captured via optical interferometry using a focused laser beam and a photodiode to generate a real-time image.

Ultra-thin ($\sim$ 1 nm) magnetic films (with at least 5 repeats) were imaged in this thesis using a Veeco Metrology Nanoscope IV Scanned Probe Microscope. For less than 5 repeats, we found that the MFM signal to noise ratio was small giving poor quality images. The magnetic tips used were low moment Bruker MESP-LM tips with coercivity < 400 Oe and magnetic moment 0.3×10^{-13} emu[1]. Low moment tips were used since the magnetic stray fields generated by ultra-thin films imaged in this thesis were weak and we wanted to avoid the writing of magnetic domains on our films by strong magnetic stray fields from the MFM tip. In comparison with the tip, the samples we studied had magnetic moments of the order of 10^{-5} emu, many orders of magnitude higher than that of the tip. The image acquisition was carried

[1]Source: `http://www.brukerafmprobes.com/p-3315-mesp-lm.aspx`

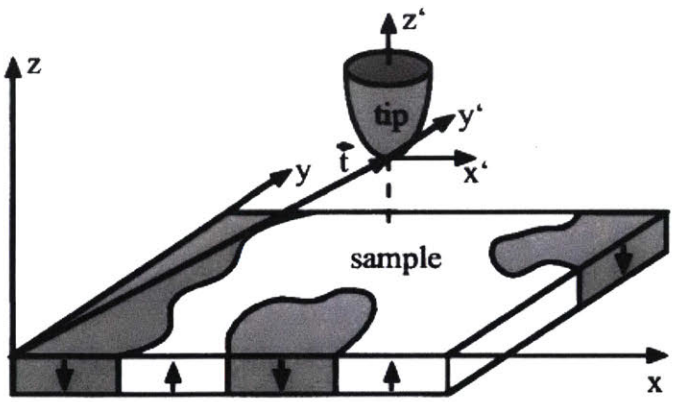

Figure 3-4: Schematic illustration of magnetic force microscopy technique. The magnetic tip scans at a small height above the sample surface and is only sensitive to perpendicular components of magnetization. Reproduced from [24].

out in the dual mode where the tip first acquired surface topography by scanning across a line in the tapping mode. The same line was scanned again to capture magnetic contrast. This time the tip was lifted up by $\sim$ 50 nm and retraced the surface profile maintaining constant tip-surface separation. Figure 6-2 shows some typical perpendicular magnetic domains imaged using MFM.

3.3 Micromagnetic simulations

Micromagnetics [68] is a semi-classical approach to studying magnetic phenomena in magnetic materials at sub micrometer levels where magnetic properties such as exchange, anisotropy and magnetization can be treated as continuous. Micromagnetics avoids the complications of quantum mechanical description of magnetism at the level of individual atoms but allows enough resolution to observe the variations in structures of domain walls. The stable configuration of magnetic domains can be calculated by minimizing the total energy including exchange (Section 2.1.1), anisotropy (Section 2.1.2), magnetostatic energy (Section 2.1.3), Dzyaloshinskii-Moriya interaction (Section 2.1.6) and Zeeman energy (interaction of magnetization with external field) as a function of several possible domain patterns. Magnetization dynamics can also be modeled using the Landau-Lifshitz-Gilbert equation [69], [70].

In this thesis, we used a GPU-accelerated micromagnetic simulation program,

MUMAX3 [71]. The simulations were run at Amazon web servers. The minimum energy configuration for μm sized regions with a lateral cell size of ~ 2 nm $\times$ 2 nm was obtained in a few hours. The third dimension of the cell size was set at the thickness of magnetic film (thickness of total film for multi-layers). The lateral dimensions of the simulation cell were chosen to be a few times smaller than the domain wall width, Δ, to ensure an accurate domain width could be calculated from simulated images. Multi-layer magnetic films were simulated using effective medium approach (Equation (5.4)). Figure 5-5a,b show typical micromagnetically simulated labyrinth domains for magnetic films covered in this thesis.

Chapter 4

Creation of multi-domain state with in-plane fields

Ferromagnetic thin films sandwiched between two heavy metals or a heavy metal and an oxide display chiral spin textures [15], [21], [22], [49], [73], as explained in Section 2.2. These chiral spin textures can be used to store information in the form of 0s and 1s. They can also be manipulated by combinations of currents, electric and magnetic fields to read/write information. The key parameter to characterize these materials is the Dzyaloshisnkii-Moriya interaction (DMI) (Section 2.1.6), which determines whether a material exhibits spin chirality. If DMI is strong, the system spontaneously exhibits stable chiral spin structures [48]. The critical strength required for spontaneous formation of chiral spin structures has been determined as:

$$\frac{H_D}{H_K} > \frac{2}{\pi} \tag{4.1}$$

where H_D is the DMI effective field and H_K is the anisotropy field (Section 2.1.7) [74]. The DMI effective field is defined as $H_D = \pm\frac{D}{\mu_0 M_s \Delta}$ directed normal to the

Sections of this chapter including figures have been published before in - P. Agrawal, U. Bauer, and G. S. D. Beach, "Spontaneous Domain Nucleation under In-Plane Fields in Ultrathin Films with Dzyaloshinskii-Moriya Interaction", *Journal of Applied Physics*, vol. 117, no. 17, p. 17C744, May 2015, ISSN: 0021-8979. DOI: 10.1063/1.4917057. [Online]. Available: http://dx.doi.org/10.1063/1.4917057%20http://scitation.aip.org/content/aip/journal/jap/117/17?ver=pdfcov%20http://scitation.aip.org/content/aip/journal/jap/117/17/10.1063/1.4917057

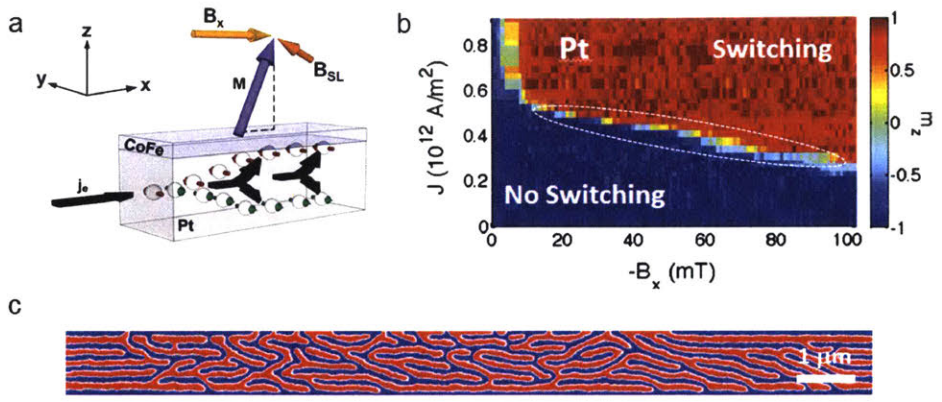

Figure 4-1: a) Schematic of current and field application in spin Hall switching experiment.The current j_e and field B_X are applied parallel to each other and in the film-plane along $\hat{x}$. B_{SL} denotes the effect field induced from the current-induced Slonczewski-like torque. At strong current and in-plane magnetic fields, the net torque produced switches magnetization from -$\hat{z}$ to $\hat{z}$. Adapted from [21]. b) Switching phase diagram for Pt/CoFe/MgO showing switching of magnetization in the upper right region with a combination of strong current density(y-axis) and in-plane mgnetic field (x-axis). The switching phase boundary is encircled showing intermediate multi-domain states as simulated in c. Adapted from [75].

domain wall where D is the DMI constant, Δ is domain wall width and the +(-) sign corresponds to up-down(down-up) domain walls.

While materials with high H_D show spontaneous chirality, one can also potentially generate metastable chiral states in magnetic thin films with weaker DMI by appropriate perturbation of the uniformly out-of-plane magnetized state. The existence of these metastable multi-domain states has been confirmed experimentally by spin Hall switching experiments in Pt/CoFe bilayer strips with a combination of magnetic field and pulsed currents applied parallel to each other and the film plane [75]. Micromagnetic simulations revealed this intermediate state to be a multi-domain with stripe domains as shown in Figure 4-1c. However, this intermediate multi-domain state could only be created within a narrow range of current and field values along the switching phase boundary (Figure 4-1b). Moreover, this process of creation of intermediate states involved additional complexity due to the need for simultaneous application of current pulses and an in-plane field. In this chapter, we describe a process where only in-plane fields are applied to create the metastable multi-domain

state in magnetic films where the ground state is uniform. The method requires no lithographic patterning of magnetic films. All that is needed is a strong magnet which can apply magnetic fields upto a few 1000 Oe parallel to the film plane.

4.1 Role of in-plane field

The energy required for domain formation in a magnetic film is lowered in the presence of a hard-axis or in-plane magnetic field, H_X. This can be mathematically seen by considering the domain wall energy as a function of in-plane field [76] as given by

$$\sigma_{DW}(H_X) = \sigma_0 + 2K_\perp\Delta - \pi\Delta M_S \mid H_X + H_D \mid \tag{4.2}$$

where σ_0 is the Bloch-type domain wall energy density, $K_\perp$ is domain wall anisotropy energy per unit volume associated with the conversion of domain walls from Bloch to Néel, and Δ is the domain wall width. At high in-plane fields, the third term on the right becomes larger and so the domain wall energy becomes negative. The demagnetizing energy then dominates the system energetics and a multi-domain state is preferred.

4.2 Experimental methods

Thin films of composition Ta(3 nm)/Pt(3 nm)/$Co_{80}Fe_{20}$(0.6 nm)/MgO(1.8 nm)/Ta(2 nm) were prepared by DC magnetron sputtering (Section 3.1.1) under 3 mTorr Ar with a background pressure of $\sim 1 \times 10^{-7}$ Torr, on thermally-oxidized Si(100) substrates at room temperature. MgO was RF sputtered at 3 mTorr Ar. Vibrating sample magnetometry (Section 3.2.1) measurements of these samples confirmed the presence of perpendicular anisotropy in these films with an in-plane anisotropy field $H_K \sim 5000$ Oe [21]. The magnetization was probed with a polar magneto-optic Kerr effect (MOKE) setup (Section 3.2.2) with a 532 nm diode laser focused on a 3 μm spot and attenuated to 1 mW. These films have a strong Dzyalonshinskii Moriya interaction (DMI) with a DMI-effective field, $H_D \sim 2200$ Oe [74]. Thus, the ratio of the

DMI-effective field, H_D, to the in-plane anisotropy field, H_K, in these films is 0.44, which is about 70% of the critical ratio required for spontaneous formation of chiral spin textures.

4.3 Shearing of hysteresis loops

Figure 4-2 shows a series of hysteresis loops measured with MOKE polarimetry in the presence of different in-plane (parallel to the film plane) fields, H_X. In the absence of any in-plane field, the hysteresis loop is square with a coercivity, H_C, of 40 Oe, which is characteristic of the single domain magnetic state pointing out of the film-plane expected in these thin films. H_C, in this case, corresponds to nucleation field of reverse domains, since the domain wall propagation field in these samples is $<$ 20 Oe [21]. As the magnitude of the in-plane field is increased, we find that the coercivity decreases with increasing in-plane field, showing that it becomes easier to nucleate reverse domains when an external in-plane field is present. The hysteresis loops start becoming more and more sheared and the remanent magnetization, M_R, at zero out-of-plane field, H_Z, also starts decreasing after a critical threshold of in-plane field is crossed (see Figure 4-2d, e, and f). Note that these in-plane fields are lower than the anisotropy field for these films, which is around 5000 Oe [74]. An M_R/M_S ratio of < 1 in the presence of in-plane fields lower than the anisotropy field is indicative of a multi-domain state with a stripe domain pattern [75], [77]. This stripe domain pattern is expected whenever the demagnetization field exceeds the threshold for nucleation of reverse domains.

4.4 Deviation from Stoner-Wohlfarth model

To probe the formation of the stripe domain state in detail, we measure the out-of-plane component of magnetization, M_Z, as a function of applied in-plane field, H_X. M_Z was measured with polar MOKE described in Section 3.2.2. Figure 4-3a shows a schematic for this measurement. An in-plane field, H_X, serves to cant the

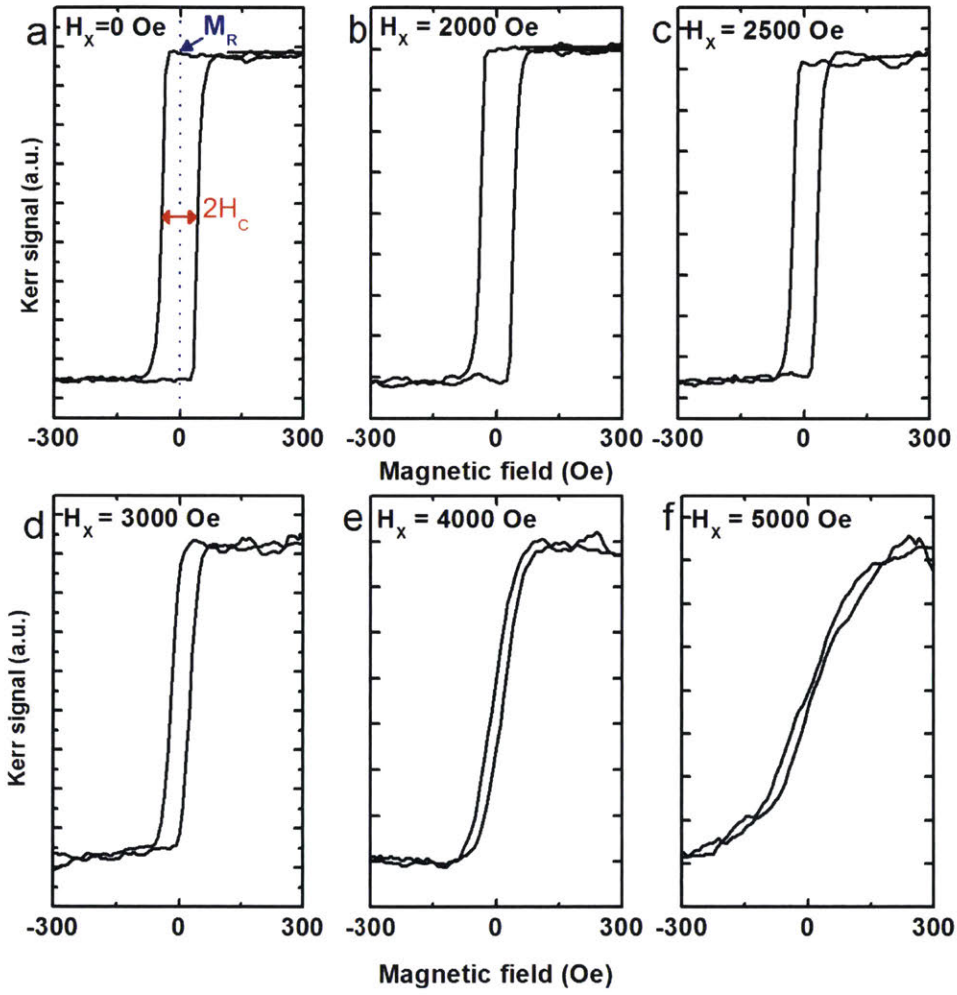

Figure 4-2: Easy axis hysteresis loops of Pt/CoFe/MgO measured with polar MOKE setup at in-plane field, H_X, of a) 0 Oe ; b) 2000 Oe ; c) 2500 Oe ; d) 3000 Oe ; e) 4000 Oe and f) 5000 Oe. Remanent magnetization, M_R, and coercivity, H_C, decrease progressively as in-plane field increases.

magnetization, $\vec{M}$, of the film such that the out-of-plane component of the magnetic moment vector, M_Z, is equal to $M_S\sin(\phi)$ where ϕ is the canting angle. According to the Stoner-Wohlfarth model, $\cos(\phi) = H_X/H_K$ for $H_X < H_K$. Therefore

$$\frac{M_Z}{M_S} = \sin(\arccos(\frac{H_X}{H_K})). \tag{4.3}$$

We measured M_Z as a function of H_X using a lock-in technique to improve the signal-to-noise ratio. In this measurement scheme, we applied pulses of out-of-plane field, H_Z, as shown in Figure 4-3b, to toggle the magnetic moment, $\vec{M}$, above and below the film plane. A lock-in amplifier, which was phase locked to the H_Z field pulses, was then used to extract M_Z as shown in Figure 4-3b. For a uniaxial system, M_Z vs H_X should take the form of Equation (4.3). Figure 4-3c shows a plot (blue dots) of the measured magnetization, M_Z, as a function of in-plane field, H_X. The red curve is the expected M_Z vs H_X plot simulated by using Equation (4.3) and using anisotropy field value H_K as 5000 Oe from [74]. The measured M_Z is significantly lower than the expected curve for in-plane field above 1500 Oe. This suggests spontaneous demagnetization and the formation of multi-domain state above the threshold in-plane field. The hysteresis loops in Figure 4-2 were measured at various in-plane field values higher than the threshold field but lower than the anisotropy field and show a steady decrease in remanence with increase in strength of applied fields.

4.5 Stability of multi-domain state

We found that the multi-domain state thus created persisted even after the in-plane field was removed. This was confirmed by performing another series of experiments where we applied an in-plane field to induce the formation of the multi-domain state, then turned it off and probed the out-of-plane magnetic moment, M_Z, using the polar MOKE. We then applied an out-of-plane field, H_Z, to find the field required to drive the multi-domain state to complete saturation. Figure 4-4a shows a schematic of

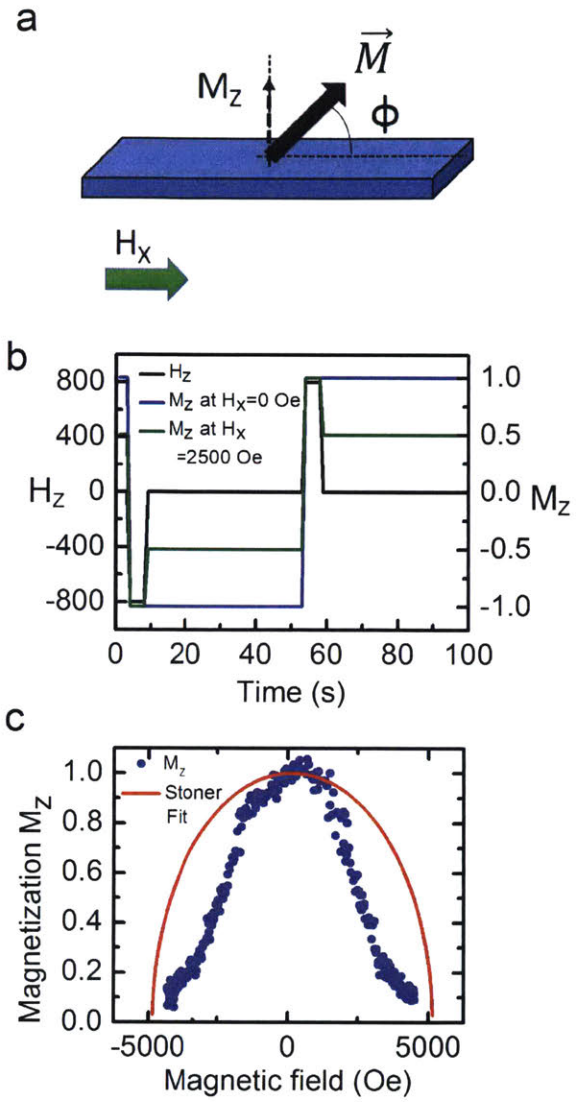

Figure 4-3: a) Schematic representation of canting of total magnetic moment, $\vec{M}$, of the film by the application of in-plane field, H_X. M_Z represents the out-of-plane component of $\vec{M}$. b) Out-of-plane field, H_Z, waveform used to toggle the net magnetic moment between up and down states. The blue and green curves show the toggling of M_Z with H_Z at in-plane fields of 0 Oe (blue) and 2000 Oe (green). c) Plot of out-of-plane magnetization, M_Z, as a function of in-plane field, measured by lock-in amplifier (blue curve) and theoretically predicted (red curve) by Stoner-Wohlfarth model.

this measurement. We see that the Kerr signal (which is proportional to M_Z) drops significantly on the application of in-plane field, H_X, and the demagnetized multi-domain state is retained until H_Z is swept. Figure 4-4b shows a plot of M_Z as a function of H_Z measured in the region where H_X is turned off. As seen from the plot, the initial magnetization (M_i in the figure) is close to zero immediately after the application of a high H_X, and gradually increases as out of plane field increases until it reaches saturation magnetization M_S. Note that the initial magnetization is not zero because of small misalignment of the in-plane field. The small out-of-plane component of the in-plane field biases the magnetic moment either up or down leading to some fractional remanence. Branch 1 of the loop corresponds to the initial magnetization curve of the sample which occurs through domain expansion. The saturation field starting from the demagnetized state is denoted by H^* in the figure and is a measure of the range of out-of-plane field required to drive domain walls. In repeated measurements, we found H^* to be systematically somewhat lower than H_C which is the field required to nucleate a reverse domain (branch 3). We also noticed that branch 1 is typically more spread out than branches 2 and 3. The spreading out behavior (switching of magnetization over a wide range of field as opposed to a sharp transition) is seen in hysteresis loops of films with multi-domain patterns (Figure 2-13) and comes from the pinning of domain walls as one set of domains expand with increasing magnetic field.

Figure 4-4c plots the absolute value of the initial magnetization, M_i, as a function of in-plane field, H_X, applied to generate the multi-domain state. This mimics the data shown in Figure 4-3c (which were measured by the lock-in technique), showing a sharp drop in M_i beyond an in-plane field of $\sim$ 1500 Oe and thus indicating the spontaneous formation of the multi-domain state beyond this threshold field.

4.6 Direct evidence of multi-domain state

A thin film of [Pt(3 nm)/Co(0.9 nm)/GdOx(3 nm)]$_5$ was investigated to see if a multi-domain state can be formed by the application of in-plane field. This film

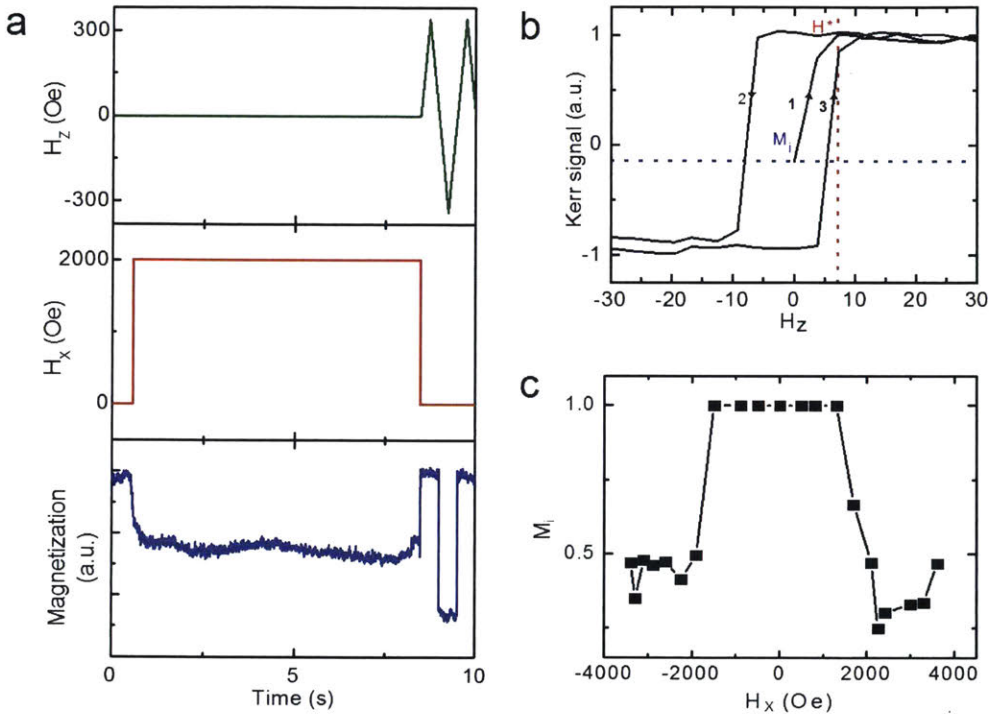

Figure 4-4: a) Applied in-plane field, H_X, out-of-plane field, H_Z, and the measured Kerr signal as a function of time. Kerr signal drops down significantly after the application of in-plane field denoting the formation of multi-domain state. b) Plot of Kerr signal against out-of-plane field, H_Z, measured after the in-plane field has been turned off to zero. Arrows denote the order of measurement starting from initial magnetization M_i. c) Initial magnetization after the application and removal of in-plane field, as a function of the in-plane field, H_X, applied to create the multi-domain state.

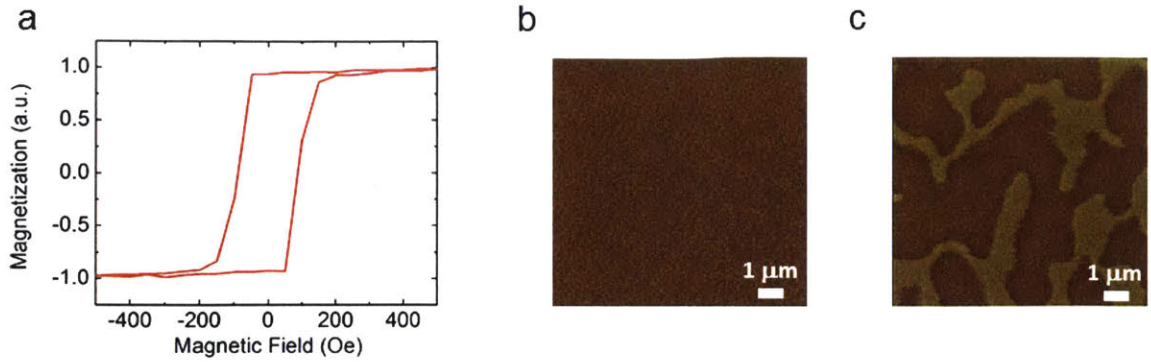

Figure 4-5: Magnetic force microscopy (MFM) images showing the formation of a multi-domain state with the application of an in-plane field. a) Hysteresis loop of thin film of $[Pt(3\ nm)/Co(0.9\ nm)/GdOx(3\ nm)]_5$ showing remanence of 1, b) MFM image of the film after growth showing no domain pattern, c) MFM image of the film after the application of an in-plane field showing interconnected domain patterns.

is expected to have significant DMI due to the Pt/Co interface and its structural inversion asymmetry. Figure 4-5a displays an easy-axis hysteresis loop, taken via VSM, showing a remanence of 1. This indicates that the ground state of this film is uniformly magnetized. Indeed, this is confirmed, via magnetic force microscopy (MFM), in Figure 4-5b which shows a single-domain in a 10×10 µm area of the film. MFM was repeated on the film after application of in-plane field of magnitude 4000 Oe. This time, a domain pattern was seen in the film (Figure 4-5c).

Note that the domains formed after the application of an in-plane field in Figure 4-5c are not stripe or labyrinth (Figure 2-12) which is expected in perpendicularly magnetized films where a multi-domain state is found, as discussed in Section 2.2. The stripe or labyrinth patterns represent the lowest energy configuration of the domain pattern. Thus, the method of application of in-plane fields to create multi-domain states in thin films with DMI does not necessarily create the lowest energy domain configuration. A standard method to randomize the domain pattern in a magnetic film is known as AC demagnetization where a decaying sinusoidal magnetic field is applied perpendicular to the film plane (along the easy axis). For our films, we have found the process of AC demagnetization to be more reliable in creating a stripe or labyrinth pattern. Figure 4-6a shows domain pattern in 10×10 µm area of

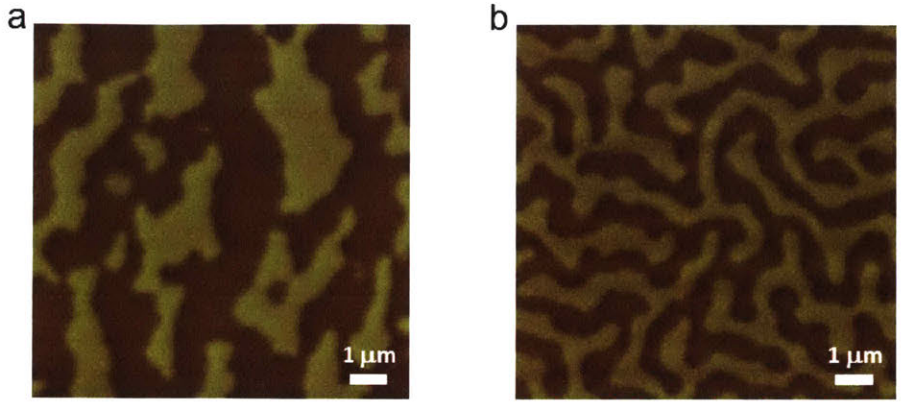

Figure 4-6: Magnetic force microscopy (MFM) images showing the domain pattern for $[Pt(2.5 - 7.5\ nm)/Co(0.8\ nm)/Pt(1.5\ nm)]_{13}$ film in a) as-grown state, b) after AC demagnetization.

a $[Pt(2.5 - 7.5\ nm)/Co(0.8\ nm)/Pt(1.5\ nm)]_{13}$ film right after film growth. After AC demagnetization, the domains reorient into a labyrinth pattern, as seen in Figure 4-6b, with equally spaced up and down domains. Due to its consistency in creating lowest energy stripe or labyrinth domain configurations, we use an AC demagnetization process to create multi-domain patterns for the films studied in the remainder of this thesis.

4.7 Conclusion

Chiral magnetic textures in thin films are of great interest for low-power data storage in magnetic memory devices [15], [16]. Magnetic thin films with perpendicular magnetic anisotropy, strong spin-orbit coupling and strong Dzyaloshinskii Moriya interaction promise to be excellent candidates for the creation and stabilization of these chiral textures. If the DMI effective field is strong enough, these chiral textures are spontaneously stabilized. However, even in systems with weaker DMI, perturbations can be introduced to create metastable non-uniform states and manipulate them [48]. We have shown that destabilization of the ferromagnetic state and formation of stripe or labyrinth domain textures can be achieved by applying an in-plane field or using AC demagnetization process. This approach could be used, for example, to generate

skyrmions in confined structures such as magnetic dots as shown in Section 6.4, rather than through current pulses as previously proposed [48], [75], [78].

Chapter 5

Measurement of DMI

As discussed in Chapter 1, the key motivation to studying perpendicularly magnetized thin films is in their application in skyrmion-based non-volatile memory devices. Skyrmions are chiral spin textures that have been found in materials with sizable PMA (Section 2.1.2) and DMI (Section 2.1.6). A common way to achieve both affects is by growing asymmetric thin films of ferromagnetic materials sandwiched between either two different non-magnetic heavy metals or between a heavy metal and an oxide (as described in Section 2.2). In multi-layers of these asymmetric stacks, the demagnetizing energy increases and therefore the uniform magnetization state breaks into multiple stripe or labyrinth domains. These stripe and labyrinth domains have been found to be useful in creating skyrmion lattices [11]–[13]. Figure 5-1 shows the transformation of stripe and labyrinth domains into skyrmion lattices in different magnetic single and multi-layers with a sandwich structure. Quantifying the DMI in magnetic single- and multi-layer films accurately and reliably is of critical importance for identifying potential materials for skyrmion-based devices. In this chapter, we describe a simple method to measure DMI using energy models of stripe domains and static magnetic characterization techniques.

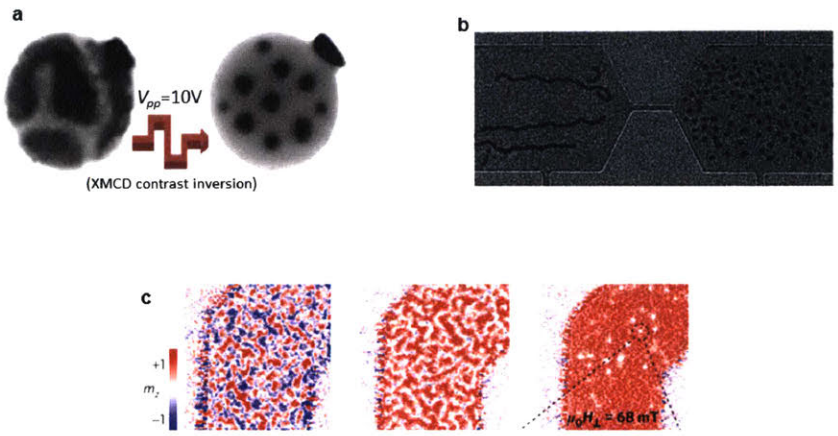

Figure 5-1: Labyrinth domains converted to skyrmion lattices in various single- and multi-layer magnetic films. a) Scanning transmission X-ray microscopy images showing transformation of labyrinth domains to hexagonal lattice of skyrmions after application of current pulses in dots of 2 µm diameter of [Pt(3 nm)/Co(0.9 nm)/Ta(4 nm)]$_{15}$. Adapted from reference [11]. b) Current flown through a nanowire in Ta(5 nm)/$Co_{20}Fe_{60}B_{20}$(1.1 nm)/TaOx(3 nm) generates elongated stripe domains on the left and a skyrmion lattice on the right. Adapted from reference [12]. c) Isolated skyrmions created from labyrinth domains by the application of out-of-plane magnetic fields in [Ir/Co/Pt]$_{10}$ multi-layers. Adapted from reference [13].

5.1 Limitations of existing methods

Existing methods of measuring DMI in magnetic thin films include first principle calculations [79], [80] or a combination of micromagnetic simulations and magnetization dynamics, i.e., motion of domain walls [21], [76], [81], [82], skyrmions or spin waves [83], [84]. All of these methods are limited in their applicability. While the first principles studies measure DMI for ideal systems with only a few magnetic monolayers grown on a sharp interface, the magnetization dynamics studies often involve poorly understood complications such as domain wall tilting [85] and pinning [28], [86] that make it hard to interpret the results reliably. Moreover, they can be used to analyze only those films which show square out-of-plane hysteresis loops (Section 2.1.7).

In this chapter, we propose a means to quantify DMI in single- and magnetic multilayer films using only static magnetic characterizations. Our method only requires that the samples be prepared in a global energy minimum demagnetized state, i.e., a state in which the domain width is determined by competing magnetic energies and

not by nucleation or pinning. There are no restrictions on the shape of the hysteresis loop as long as there is PMA. The domains should be large enough to be measured in standard domain imaging tools such as MFM (Section 3.2.3), Scanning Transmission X-ray Microscopy (STXM), X-ray Magnetic Circular Dichroism (XMCD) based imaging, or Small Angle X-ray Scattering (SAXS). Specifically, we show that measurement of remanent magnetic domain width, the perpendicular anisotropy constant, and the saturation magnetization can be used to calculate domain wall energy, and from that, the DMI strength.

5.2 Theory of stripe domains in magnetic thin films

Stripe and labyrinth domains have been seen in perpendicularly magnetized films [52]–[58] for many decades as described in Section 2.2. In this section, we start with describing well-established analytical models of stripe domain sizes as a function of total thickness and show how DMI can be calculated using these models for single- and multi-layer films. We then describe a revised model, developed recently by Lemesh, Büttner and Beach [87], that accounts for the effects of finite domain wall width as well as the stray field energies associated with volume charges in Néel domain walls. We show that the revised analytical model predicts DMI to within 1% of the preset value in micromagnetic simulations, and that the older models predict grossly inaccurate values of DMI. The revised model provides a simple and robust tool to determine the DMI strength of any material system that falls into its regime, as we demonstrate for two sputtered multi-layer magnetic films in Section 5.3 of this chapter. The theories discussed here have been developed for stripe domain patterns but also work well for labyrinth patterns [87].

5.2.1 Early models

The early models [52], [53], [88] describing stripe domains in magnetic films showed that there are two main energies that determine the equilibrium magnetic domain pattern. One of them is the demagnetizing energy per unit volume which is given by

$$\frac{E_d}{V} = \frac{4\mu_0 d}{\pi^3 t} M_S^2 \sum_{n=odd}^{\infty} \left[\frac{1}{n^3} \left(1 - \exp^{-\frac{n\pi t}{d}} \right) \right] \tag{5.1}$$

where M_S is saturation magnetization, d is stripe domain width, and t is the thickness of the magnetic film. The demagnetizing energy represents the stray field energy that the system saves in going from the single domain phase to the stripe domain phase (Section 2.1.3). The second energy is the cost associated with the creation of domain walls in the system. The energy required to create domain walls per unit volume is given by

$$\frac{E_{DW}}{V} = \frac{\sigma}{d} \tag{5.2}$$

where σ is the domain wall energy per unit area described in Section 2.1.4. The equilibrium domain width in the system can be calculated by taking the partial derivative of the total energy in the system, i.e., Equation (5.1) + Equation (5.2) with respect to the domain width, d. The resulting relation between equilibrium domain width, d, and total thickness of film, t, takes the form:

$$\frac{4\mu_0 d^2 M_S^2}{\pi^2 \sigma t} \sum_{n=odd}^{\infty} \left[\frac{1}{n^3} \left(1 - \exp^{-\frac{n\pi t}{d}} \left(1 + \frac{n\pi t}{d} \right) \right) \right] - 1 = 0 \tag{5.3}$$

For magnetic multilayers interspersed with non-magnetic layers, the characteristic quantities and relations must be modified to accommodate the dilution of magnetic energies in the system (since the total volume now has non-magnetic films which do not contribute to the total magnetic energy of the system). To do this, we define the scaling factor, f, as the ratio of thickness of magnetic layer, T, to the total thickness per repeat, λ, in the multilayer structure (Figure 5-2). The multi-layer film can be described as an effective magnetic medium [11], [89] with thickness equal to the total thickness of the multilayer film and magnetic characteristics, A_{ex}, D, K_{eff}, and M_S scaled linearly with f. The magnetostatic energy (which is proportional to M_S^2) of this effective medium would scale with f^2 while the domain wall energy, σ, would be scaled with f. The scaling laws are summarized in Equation (5.4) where A'_{ex}, D', M'_S and K'_U represent the scaled effective medium parameters.

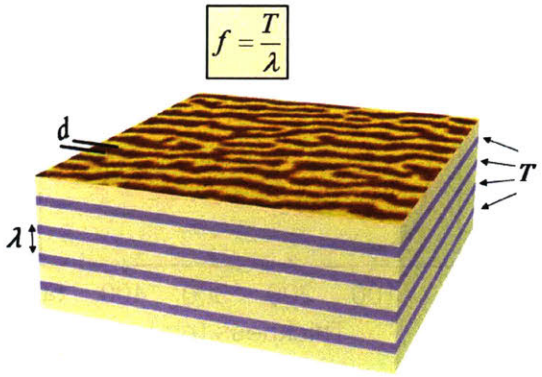

Figure 5-2: Schematic of magnetic multilayer film with stripe domains of width, d. The purple layers are magnetic films with thickness T, while the cream layers are non-magnetic. The thickness of each repeating set of layers is λ. A key structural parameter is the scaling factor, f, defined as the ratio of thickness of each magnetic layer to the thickness of a repeating set of layers, T/λ.

$$\begin{aligned} A'_{ex} &= A_{ex} f \\ D' &= Df \\ M'_S &= M_S f \\ K'_U &= K_U f - \frac{\mu_0 M_S^2}{2}(f - f^2) \end{aligned} \tag{5.4}$$

The modified relation between equilibrium domain width, d, and total thickness of film, t, for a multilayer film is given by [89]:

$$\frac{4\mu_0 d^2 M_S^2}{\pi^2 \sigma t} f \sum_{n=odd}^{\infty} \left[\frac{1}{n^3} \left(1 - \exp^{-\frac{n\pi t}{d}} \left(1 + \frac{n\pi t}{d} \right) \right) \right] - 1 = 0 \tag{5.5}$$

Equations (5.3) and (5.5) predict domain size to vary with film thickness as seen in Figure 5-3 with a characteristic minimum and an asymmetric increase of domain size for smaller and larger thicknesses. The total thickness, t, could change either by changing the number of repeats or by changing the thickness of any of the individual layers in one repeat. A detailed discussion of variation of domain size with several variables such as magnetic layer thickness, non-magnetic layer thickness, and scaling factor is given in Chapter 6.

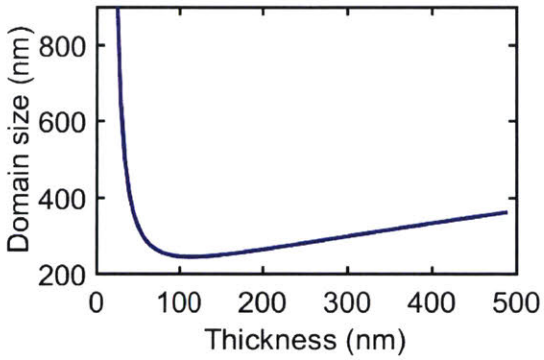

Figure 5-3: Domain width as a function of film thickness for perpendicularly magnetized thin films showing stripe or labyrinth domain patterns. This specific curve has been modeled for a film with $T = 0.9$ nm, $\lambda = 4.9$ nm, $M_S = 7 \times 10^5$ A/m, $A_{ex} = 10^{-11}$ J/m, $K_U = 5 \times 10^5$ J/m^3, and $D = 1$ mJ/m^2.

Equations (5.3) and (5.5) can be used to measure domain wall energy, σ, when equilibrium domain width, d, the layer thicknesses, and saturation magnetization, M_S, are known [11], [13], [57], [90]. The layer thicknesses can be obtained from film deposition rates (as described in Section 3.1.1) or X-ray reflectometry, d can be measured from domain pattern images, and M_S and K_U can be obtained from SQUID or VSM measurements. The DMI strength, D, can then be calculated from the domain wall energy, as outlined in the next section.

5.2.2 Role of domain wall energy

The models described in the previous section were derived for Bloch domain walls (Equation (2.3)). For films with strong DMI, the domain walls have a Néel orientation and their energy is given by Equation (2.5). The DMI, D, can be calculated if A_{ex}, K_{eff}, $K_\perp$, and ψ are known. Attempts to simplify Equation (2.5) have either ignored [11] $K_\perp$ in domain wall energy calculations, or approximated it to thick-film limit [91], $K_\perp = \frac{\mu_0 M_S^2}{2}$, or thin-film limit [49], [74], [82], $K_\perp = ln(2)t\frac{\mu_0 M_S^2}{2\pi\Delta_0}$. Büttner et al. [92] have shown that these approximations are significantly different from the transverse anisotropy, $K_\perp$, seen in perpendicularly magnetized multi-layer films which are studied for skyrmionic memory applications. For our films, we found $K_\perp$ to be of the same order of magnitude as other terms in Equation (2.5), and therefore it was

necessary to calculate an accurate expression for it in order to obtain an accurate value of DMI. According to reference [92], $K_\perp$ is given by:

$$K_\perp \approx \mu_0 M_S^2 \frac{\mathfrak{d}^2\mathfrak{f} + \mathfrak{d}\ln(2)}{2\mathfrak{d}^2\mathfrak{f} + \mathfrak{d}\mathfrak{g} + 1}$$

with

$$\begin{aligned} \mathfrak{f} &= (0.9\tau - 0.76)/N, \\ \mathfrak{g} &= \tau[1.8 - 0.05\ln(N + 12) + 0.05\ln(\tau)], \text{ and} \\ \mathfrak{d} &= \mathcal{T}N \end{aligned} \tag{5.6}$$

where Δ is the domain wall width (described in Section 2.1.4 and given by Equation (2.4)), N is the number of repeats in a multilayer structure, and the ratios involved are defined as:

$$\begin{aligned} \mathcal{P} &= \frac{\lambda}{2\pi\Delta}, \\ \mathcal{T} &= \frac{T}{2\pi\Delta}, \\ \tau &= \frac{\lambda}{T} = \frac{1}{f}. \end{aligned} \tag{5.7}$$

Here T, f, λ are as shown in Figure 5-2. For a single layer, $N = 1$, $T = t$, the total thickness of the film, and $\tau = 1$.

Figure 5-4 shows the influence of domain wall energy on the equilibrium domain size d in magnetic thin films. We find that d depends strongly on the nature of the domain wall. The presence of DMI in the system lowers the domain wall energy thus enabling multiple smaller domains to be formed (blue curve $\rightarrow$ red curve). The domain wall anisotropy energy, $K_\perp$ increases the domain wall energy thereby increasing the equilibrium domain width (red curve $\rightarrow$ green curve). However, in systems with DMI, the domain wall energy is still lower than Bloch walls. Hence, Néel walls are more stable.

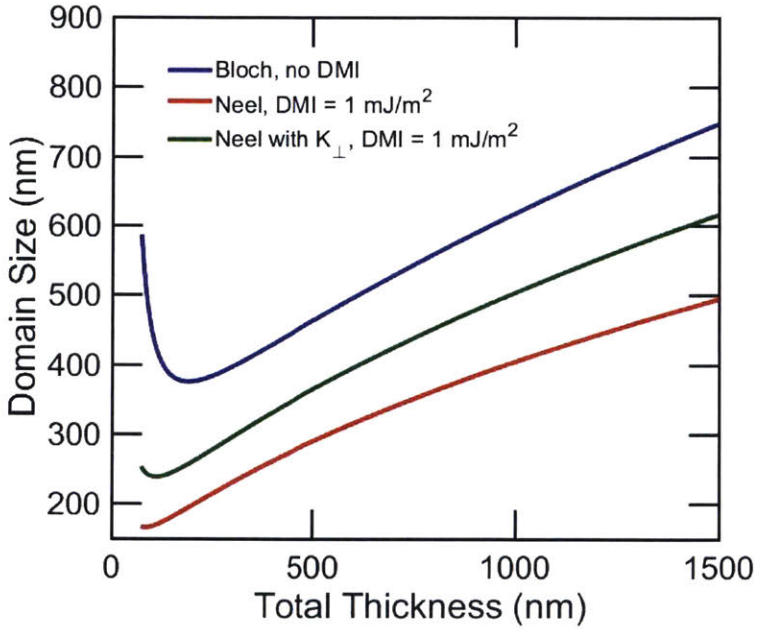

Figure 5-4: Domain size dependence on total thickness for different types of domain walls. The blue line represents a Bloch domain wall, the red line a Néel domain wall with $D = 1$ mJ/m^2 ignoring the effect of volume charges within the Néel domain wall, and the green line a Néel domain wall with $D = 1$ mJ/m^2 including the effect of volume charges.

5.2.3 Role of domain wall width

The models described in the previous section assume that $\Delta << d$ and $\Delta << t$ and hence ignore the interaction between neighboring domain walls. This is true for magnetic films with Bloch walls where domain sizes are in μm or cm, and are at least 100 times the domain wall widths on the order of tens of nm. However, these assumptions fail for several relevant films for skyrmion memory applications. A more elaborate model accounting for interaction between neighboring domain walls has been calculated in reference [87]. Specifically, this model shows that domain wall width, Δ, and domain wall angle, ψ, are functions of film thickness. According to this model, the total energy $\mathcal{E}_{tot}$ (in SI units) of a demagnetized magnetic multi-layer film is given by

$$\mathcal{E}_{tot} = \frac{1}{d}\left[\frac{2A_{ex}}{\Delta} + 2K_U\Delta + \pi D\sin(\psi)\right] + \mathcal{E}_s + \mathcal{E}_v + \frac{\mu_0 M_S^2}{2}(f - f^2) \tag{5.8}$$

where $\mathcal{E}_s$ and $\mathcal{E}_v$ are the surface and volume stray field energies per unit volume respectively given by

$$\begin{aligned}
\mathcal{E}_s &= \frac{\pi\mu_0 M_S^2 f^2\Delta^2}{dt}\sum_{n=1}^{\infty}\left[\frac{\sin^2\left(\frac{n\pi}{2}\right)}{\sinh^2\left(\frac{\pi^2 n\Delta}{2d}\right)}\frac{1-\exp(-\frac{\pi nt}{d})}{n}\right], \text{ and} \\
\mathcal{E}_v &= \frac{\pi\mu_0 M_S^2 f^2\Delta^2}{dt}\sin^2(\psi)\sum_{n=1}^{\infty}\left[\frac{\sin^2(\frac{n\pi}{2})}{\cosh^2\left(\frac{\pi^2 n\Delta}{2d}\right)}\frac{\exp\left(-\frac{\pi nt}{d}\right)+\frac{\pi nt}{d}-1}{n}\right].
\end{aligned} \tag{5.9}$$

The surface stray field energy, $\mathcal{E}_s$, is the stray field that comes from stripe domains (same as that of Equation (5.5)) but for a system with finite Δ. The volume stray field energy, $\mathcal{E}_v$, includes the stray field interactions between volume charges in the Néel domain walls of the magnetic multi-layer film. This term is therefore proportional to $\sin^2(\psi)$, where ψ is a measure of the Néel character of domain walls. Similar to the previous section, the equilibrium domain width, d, can be found from taking a partial derivative of $\mathcal{E}_{tot}$ with respect to d.

The thickness dependence of domain wall width, Δ, is given by Equations (5.10),

(5.12) and (5.13), and that of domain wall angle, ψ is given by Equation (5.15).

$$\Delta_0 = \sqrt{\frac{A_{ex}}{K_{eff}}} \tag{5.10}$$

where

$$K_{eff} = K_U - \frac{\mu_0 M_S^2}{2}. \tag{5.11}$$

$$\Delta_\infty = \sqrt{\frac{A_{ex}}{K_U + \frac{\mu_0 M_S^2}{2}\sin^2(\psi)}} \tag{5.12}$$

Then domain wall width Δ is given by

$$\Delta = \Delta_0 - \frac{1}{\frac{2\pi(Q-1)}{d} + \frac{1}{\Delta_0 - \Delta_\infty}} \tag{5.13}$$

with quality factor, Q, defined as

$$Q = \frac{2K_U}{\mu_0 M_S^2}. \tag{5.14}$$

$$\sin(\psi) = \begin{cases} -D/D_{thr} & \text{for} |D| < D_{thr} \\ -\text{sgn}(D) & \text{for} |D| \geq D_{thr} \end{cases} \tag{5.15}$$

where D_{thr} is the minimum DMI required in a given magnetic film (single or multi-layer) for it to have Néel domain walls, i.e., for the domain wall angle ψ to be -90°. It is given by

$$D_{thr} = \frac{2\mu_0 M_S^2}{\frac{\pi^2}{t\ln(2)} + \pi\sqrt{\frac{K_U + \frac{\mu_0 M_S^2}{2}}{A_{ex}}}} \tag{5.16}$$

The thickness dependence equations (Equations (5.10) to (5.16)) have been written for single-layer films. For magnetic multi-layer films, the scaled parameters (Equation (5.4)) should be used when calculating ψ and Δ.

5.2.4 Selection of the appropriate model

In this section, we verify the theories described in the previous section for a micromagnetically simulated thin film with DMI. Specifically, we show the degree of inaccuracy in measurement of DMI through the use of the following 3 models:

1. Model 1 is the original stripe-domain model [52], [53], [88], [89], [93] developed for single- and multi-layered films of intermediate thicnesses with PMA and Bloch domain walls. It assumes the domain walls to be sharp or $\Delta = 0$ (Eqs. (2.3) and (5.5)).

2. Model 2 is a modification of model 1 for Néel domain walls and includes domain wall transverse anisotropy, $K_\perp$ (Equation (5.6)). The stray field energy is the same but the domain wall energy includes effects of DMI and volume charges inside Néel walls (Equation (2.5)).

3. Model 3 is the model from reference [87] where the total energy includes effects of finite domain wall width, Δ, and interactions of volume charges inside Néel domain walls (Equation (5.8)).

We implement these three models on data obtained from micromagnetic simulations using the MUMAX3 software package [71]. Similar to experimental films [11]–[13] that have demonstrated skyrmions, the parameters used for simulations are: $M_S = 7 \times 10^5$ A/m, $A_{ex} = 10^{-11}$ J/m, $K_U = 5 \times 10^5$ J/m^3, $T = 0.9$ nm, $N = 15$, and $D = 1$ mJ/m^2. λ is systematically varied from 2.9 to 7.9 nm thereby varying f from 0.31 to 0.11. The initial magnetization state is chosen to be random. The magnetic thin film is relaxed in the presence of no external fields and the equilibrium labyrinth domain width in the relaxed magnetic contrast images is measured by taking a Fourier Transform (FT). Figure 5-5 a,b show 5×5 µm simulated magnetic contrast images at scaling factors, $f = 0.31$ and $f = 0.11$ respectively. The cell size chosen for the simulations is 2 nm × 2 nm × thickness of the film. The lateral dimensions of the simulation cell are chosen to be a few times smaller than the domain wall width for the magnetic film simulated, which in this case is $\Delta \sim 6$ nm.

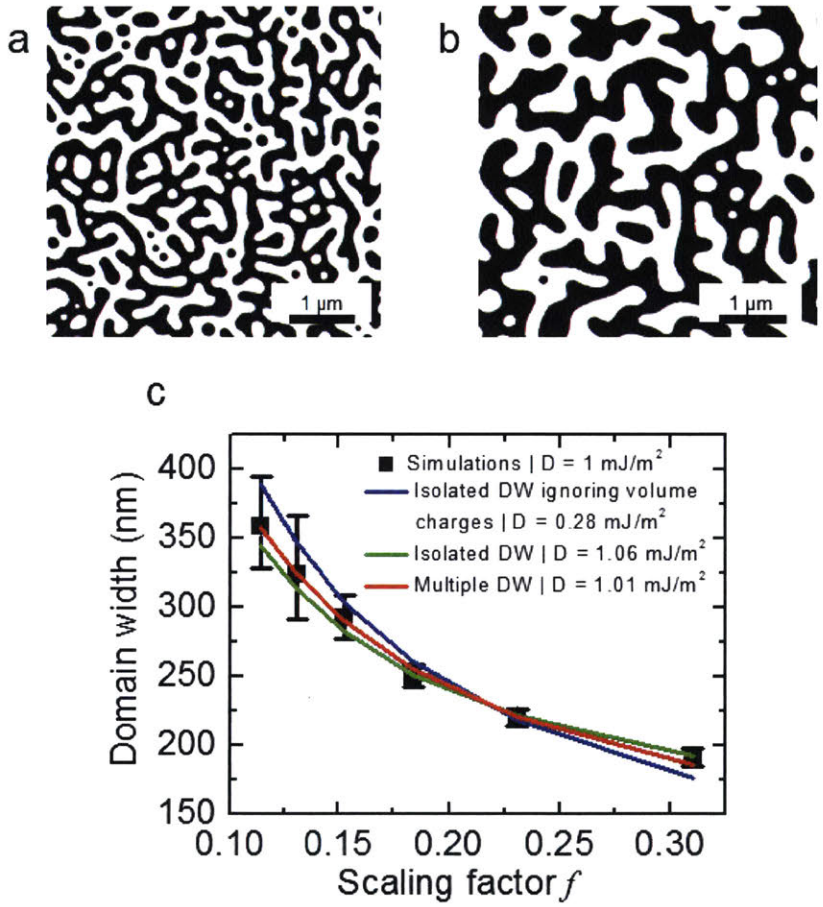

Figure 5-5: Measurement of DMI for micromagnetically simulated multi-layer film with DMI. a, b) 5×5 μm images simulated with MUMAX3 showing labyrinth domains for scaling factors 0.31 and 0.11 respectively. c) Domain size as a function of scaling factor extracted from simulated images (black squares); fit to the stripe domain model developed by Suna (blue curve), model accounting for volume charges in the domain wall (green curve) and the multiple domain wall model (red curve).The error bars on black squares correspond to errors in extraction of domain size from FT.

The resulting variation of domain size with f and the least-squared fit of the data with different stripe domain models is seen in Figure 5-5c. While a good fit is obtained with all models, the DMI value obtained from the three models are very different. The blue curve shows a fit to the isolated domain wall approximation that does not include the effect of volume charges in the domain wall via $K_\perp$ (model 1). It gives a very small value of $D = 0.28$ mJ/m^2. The green curve shows the fit obtained from using model 2 and gives a 6% error in estimation of DMI. This does not include the effect of a finite domain wall width Δ but includes effects of volume charges within domain walls via $K_\perp$. The red curve is the most accurate fit (model 3) with only 1% error. Note that this was a one parameter optimization with D as the only fitting parameter. Thus we show that given all other parameters of the film are known accurately, model 3 gives the DMI value to within 1% of the actual value. In the next section, we apply model 3 to measure DMI in experimentally grown magnetic thin films.

5.3 Application of model to experimental films

In this section, we apply model 3 to two films, one which has exhibited skyrmion lattices in reference [11] and the second with similar layer thicknesses but also inversion symmetry and hence an expected $D = 0$. We show that the measured DMI values indeed agree with expected values from theory and values obtained by other authors for similar films. We also find that the film growth mechanism imposes a variation in PMA with the thickness of the film which is reflected in the DMI values measured.

5.3.1 Experimental methods

Multi-layer thin films were grown with the compositions: Ta(3 nm)/[Pt(2.5 - 7.5 nm)/$Co_{60}Fe_{20}B_{20}$(0.8 nm)/MgO(1.5 nm)]$_{13}$/Ta(2 nm) and Ta(3 nm)/[Pt(2.5 - 7.5 nm)/Co(0.8 nm)/Pt(1.5 nm)]$_{13}$/Ta(2 nm) on 3" wafers each. Henceforth they are referred to as the asymmetric and symmetric stacks respectively. The deposition was done via sputtering in an AJA 6-target sputter deposition system at the Harvard

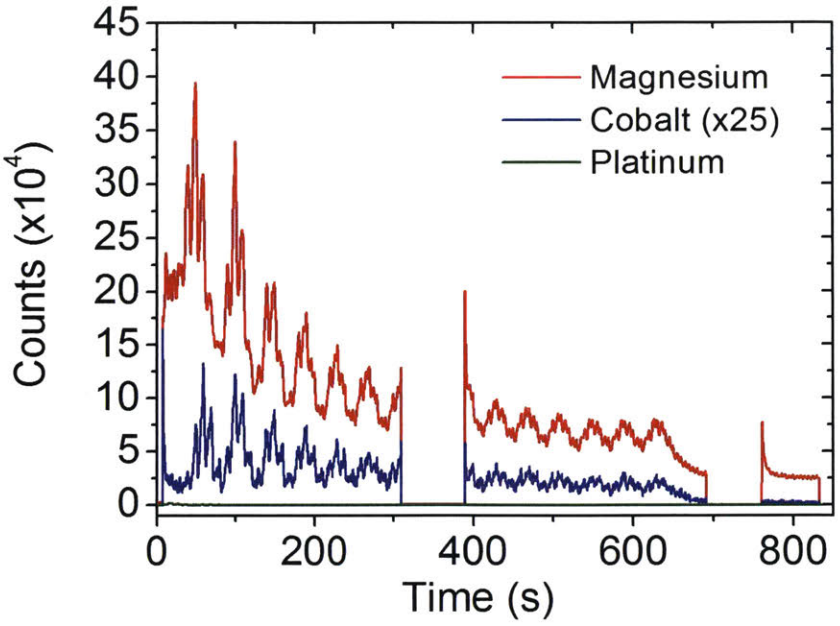

Figure 5-6: Secondary Ion Mass Spectrometry of $[Pt/CoFeB/MgO]_{13}$ wedge showing 13 fringes confirming 13 layers of repeats.

Center for Nanoscale Systems on Si(100) substrates with 50 nm thermally-grown SiO_2, at room temperature, with a base pressure of 2.9×10^{-8} Torr, and at Ar pressure of 4.7 mTorr. The CoFeB and MgO layers were deposited by rotational RF sputtering while the Ta and Co layers were deposited by rotational DC magnetron sputtering. Pt was deposited as a wedge where the thickness of the Pt layer was systematically varied from 2.5 nm to 7.5 nm, via stationary DC magnetron sputtering. The distance from the sputtering gun determined the thickness profile of the deposited Pt film.

Figure 5-6 shows Secondary Ion Mass Spectrometry (SIMS) data for the $[Pt/CoFeB/MgO]_{13}$ film showing 13 fringes. The mass spectrometer analyzed the chemical composition of ions as the film was milled down from the surface until the Si wafer was reached. This confirmed that we had 13 layers of the [Pt/CoFeB/MgO] film.

Domains were imaged in the as-prepared and AC-demagnetized states using MFM (Section 3.2.3) with the help of low moment CoCr magnetic tips (MESP-LM) from Bruker. The AC-demagnetization process served to reorient the domains from labyrinth to stripe-like (Figure 5-7 b-d) and ensured that the domain pattern thus obtained

was the lowest energy configuration. Domain widths were quantified from the Fourier Transforms (FT) of 10×10 μm MFM images (such as those shown in Figure 5-7 b-d and Figure 5-9 b-d) taken at different Pt thicknesses along the wedge. Figure 5-8b and Figure 5-10b show the domain size variation as a function of scaling factor for the asymmetric and symmetric stack respectively. Domain sizes reduce with increasing scaling factor for both the films as expected from theory and simulations.

5.3.2 Asymmetric film with DMI

Figure 5-7a shows a schematic of the asymmetric multilayer stack with the gradient of the wedge exaggerated for clarity. Each 3" wafer was broken down into 12 longitudinal pieces with each piece corresponding to a different Pt thickness along the wedge. Easy- and hard-axis hysteresis loops were measured for every piece using VSM (Section 3.2.1). The saturation magnetization, M_S, was averaged across different Pt thicknesses and measured to be 690 ± 60 emu/cc for the asymmetric stack. Figure 5-7 e-g show the variation in the shape of hysteresis loops of the asymmetric stack with changing Pt thickness. The multilayer film in the region of the thickest Pt layer (Figure 5-7g) shows a butterfly easy-axis hysteresis loop (typical of multilayer magnetic films with stripe domains) and almost-straight line hard axis loop. As Pt thickness is decreased, the easy axis hysteresis loops get more and more sheared while the hard-axis hysteresis loops get more and more S-like (Figure 5-7 g-e). This variation in hysteresis loops can be understood from the increase in density of magnetic layers with decreasing Pt thickness. As the magnetic layers come closer to each other, the interaction between them increases resulting in a stronger magnetostatic coupling which is manifested as more sheared hysteresis loops with higher saturation fields [93]. One can also see that domain widths are monotonically increasing with increasing Pt thickness.

For our symmetric Pt-wedge film we found that the anisotropy energy measured from the area between easy- and hard- axes hysteresis loops, K_{hys}, was not a constant and instead varied with the thickness of the Pt layer (Figure 5-8a). The experimen-

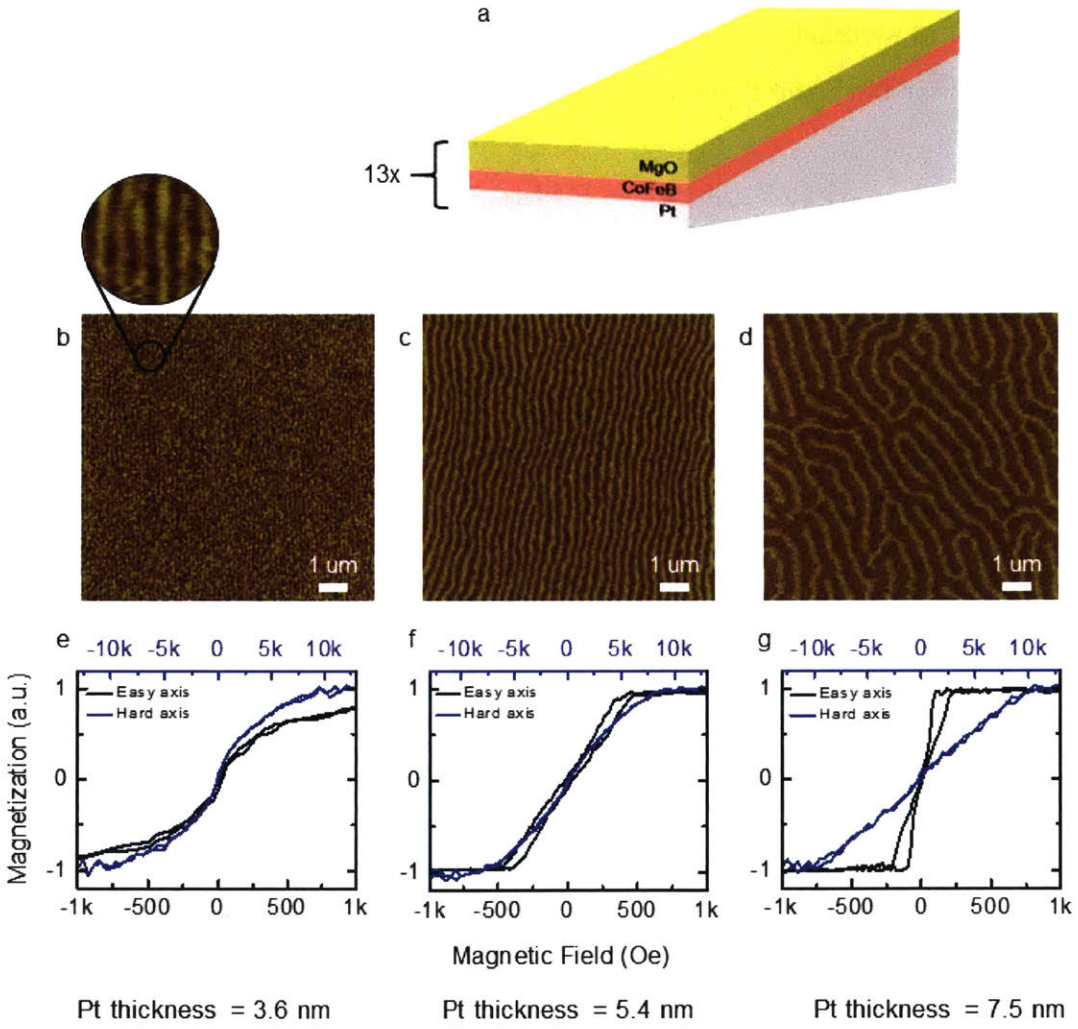

Figure 5-7: a) Schematic of asymmetric multi-layer magnetic film with Pt layer wedged across the wafer. b) - d) 10×10 µm MFM images showing stripe domains for Pt thicknesses 3.6 nm, 5.4 nm and 7.5 nm per repeating layer respectively. Inset of b) shows a 10 × magnified image of stripe domains. e)-g) Easy- and hard- axis hysteresis loops for Pt thicknesses 3.6 nm, 5.4 nm and 7.5 nm per repeating layer respectively.

tally observed values were best fit by the polynomial function:

$$K_{hys} = (9 \pm 1) \times 10^6 - (9 \pm 2) \times 10^7 f + (2 \pm 1) \times 10^8 f^2 \tag{5.17}$$

where f is the scaling factor and K_{hys} is in erg/cc. This variation in anisotropy energy might be a manifestation of the film growth mechanism (directional deposition of Pt as opposed to rotational sputtering which gives a more uniform layer) which could induce variations in grain size or roughness with changing thickness of the Pt layer [94], [95]. We measured low-angle Reciprocal Space Maps (RSM) [96] to see if there was any systematic variation in correlated roughness between the layers with Pt thickness but could not obtain any conclusive results. In future, characterization of interfaces via TEM can be carried out to study the interface characteristics as a function of Pt thickness.

Figure 5-8b shows a plot of domain sizes obtained from MFM images with scaling factor for the asymmetric stack. The error bars correspond to the variation in domain sizes as measured from the uncertainty in frequency in Fourier Transform of the MFM images. No fit to this measured domain width data could be obtained without accounting for the anisotropy variation experimentally observed in Figure 5-8a. The blue curve shows fit with model 3 (described in Section 5.2.4) with PMA variation of Equation (5.17) and D as the only fitting parameter. An optimized value of $D = 1.6$ mJ/m^2 was obtained. M_S was varied within the experimental error range, however no significant changes were seen in the optimized value of D with variation of M_S. The value of D measured using our method is similar to the $D = 1.2$ mJ/m^2 measured for [Pt(3 nm)/CoFe(0.6 nm)/MgO(1.8 nm)] film by domain wall motion experiments [74], and $D = 1.8$ mJ/m^2 measured for [Pt(4 nm)/CoFeB(1 nm)/MgO(2 nm)] by spin Hall switching experiments [97].

A large variation in perpendicular magnetic anisotropy across the wedge (as seen in Figure 5-8a) seems to indicate that the interface quality is varying in some systematic way across the wedge. This would indicate that DMI, which also comes from interfaces, must vary systematically across the wedge. To test this hypothesis, DMI

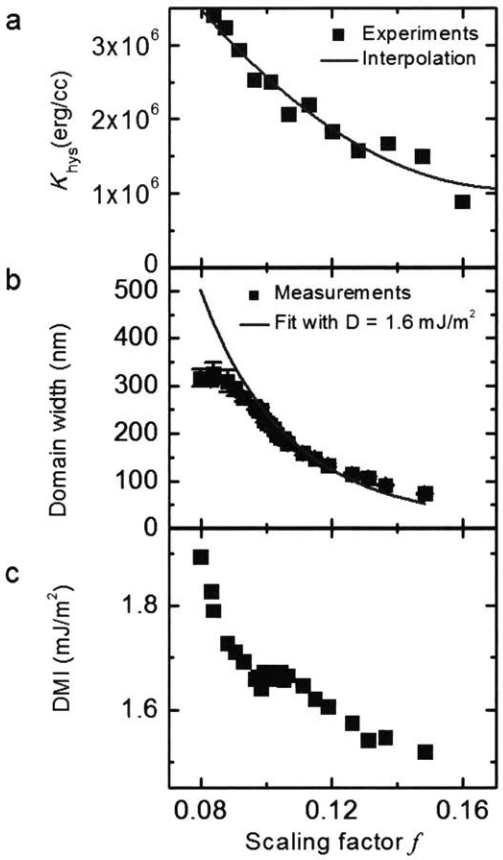

Figure 5-8: Measurement of DMI for $[Pt/CoFeB/MgO]_{13}$ wedge. a) Anisotropy obtained from hysteresis loops as a function of scaling factor, f, b) variation of domain size with scaling factor, f, showing fit with model 3 with D as fitting parameter (blue), c) D calculated separately for different positions along the wedge (black squares).

was calculated separately for different Pt thicknesses using model 3 and the corresponding K_{hys} (from Figure 5-8a). As seen in Figure 5-8c, the DMI values indeed show a systematic trend following the same pattern as that of K_{hys}. D_{thr} as described in Section 5.2.3 for this sample was < 0.1 mJ/m^2 across the wedge which is significantly smaller than the DMI values measured. This confirms our assumption of Néel walls with ψ = -90°. In principle, and for low DMI samples, the walls might be transient with ψ in between 0° and -90°.

5.3.3 Symmetric film with no DMI

Similar analysis was carried out for the symmetric stack. The average saturation magnetization across the wedge was measured to be 1420 $\pm$ 75 emu/cc. The easy axis hysteresis loops showed a higher coercivity, as compared to the asymmetric film, with remanence of 1. The hard axis loops were observed to be more linear (Figure 5-9 e-g) than those of the asymmetric film. The variation in the shape of the hysteresis loops across the symmetric wedge was seen to be much weaker in comparison with the asymmetric stack, especially for the hard-axis loops.

Figure 5-10 shows the DMI calculation for the symmetric sample. Here again, anisotropy variation was observed across the wedge (Figure 5-10b) in the changing shapes of the hysteresis loops and quantified as:

$$K_{hys} = (8.1 \pm 0.7) \times 10^6 - (1.5 \pm 0.6) \times 10^7 f \tag{5.18}$$

where f is the scaling factor and K_{hys} is in erg/cc. Figure 5-10b shows decreasing domain size obtained from MFM images (black squares) with increasing scaling factor for the asymmetric stack. Note that the domain sizes for the symmetric stack are much larger than that of the asymmetric one (Figure 5-10b) showing a higher domain wall energy in the symmetric film. The blue curve shows the fit of the domain size vs scaling factor data to the model with $D = 4 \times 10^{-8}$ mJ/m^2. The very small D obtained is consistent with the cancellation of interfacial DMI in symmetric magnetic multilayer films predicted in literature [98], [99]. In fact the domain walls show a Bloch character since the D value obtained was close to zero and below D_{thr}. The domain wall angle was also found to be almost zero (of the order of 10^{-8}) across the wedge.

5.4 Sources of errors

In this section, we plot domain size, d, as a function of DMI in Figure 5-11. The general trend is for d to decrease with increasing DMI, D, due to the reduction in

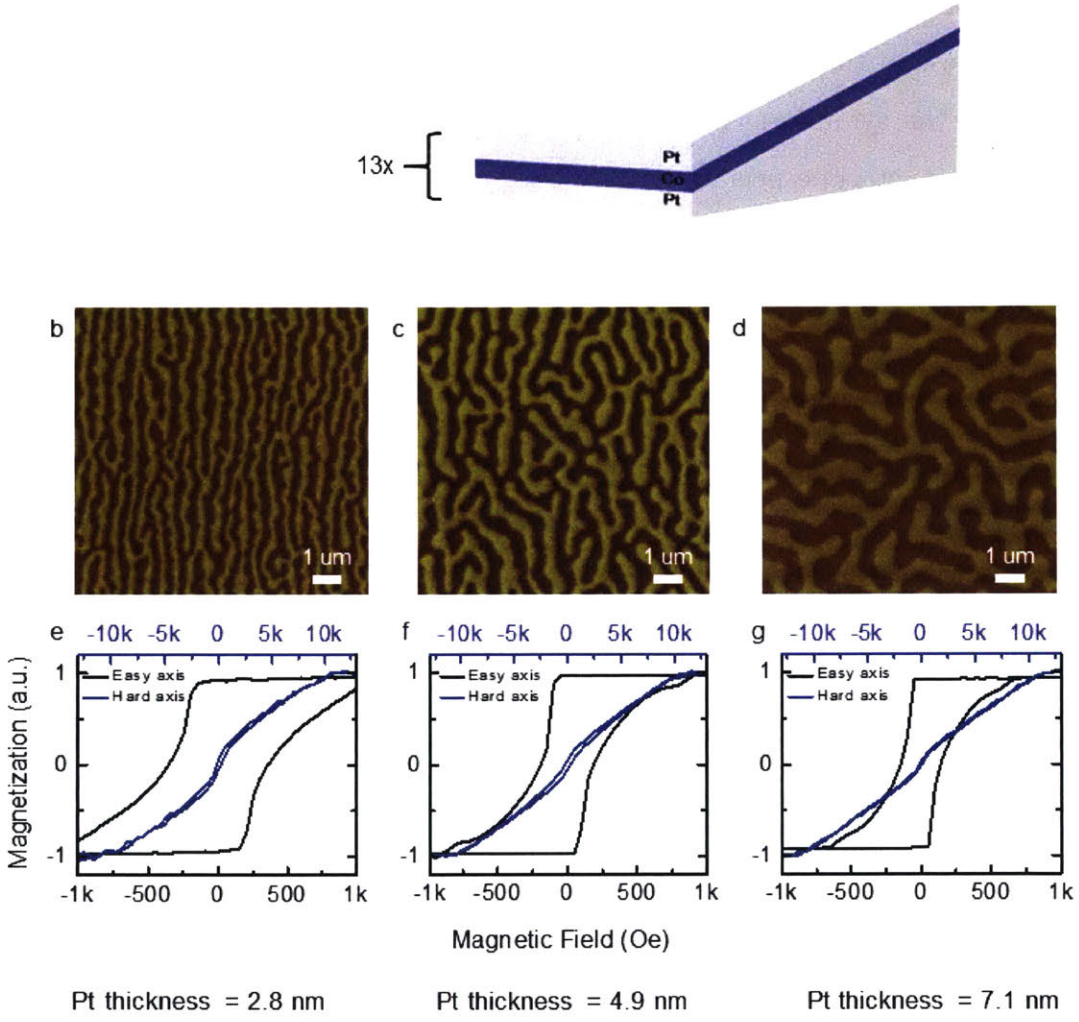

Figure 5-9: a) Schematic of symmetric multi-layer magnetic film with Pt layer wedged across the wafer. b)-d) 10×10 µm MFM images showing stripe domains at different Pt thicknesses. e)-g) Easy- and hard- axis hysteresis loops across the wedged multi-layer stack.

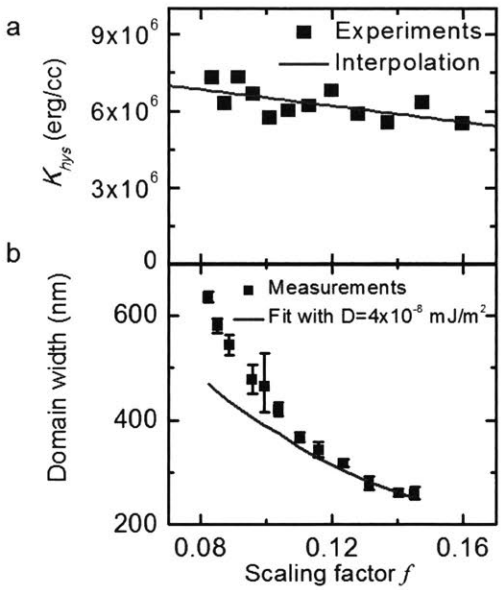

Figure 5-10: DMI calculation in $[Pt/Co/Pt]_{13}$ wedge. a) Anisotropy obtained from hysteresis loops as a function of scaling factor, f. b) Variation of domain size with scaling factor, f, showing fit with model 3 (blue curve) for $D = 4 \times 10^{-8}$ mJ/m^2 with anisotropy variation of a included in the model.

domain wall energy. Further, we show the sensitivity of the extracted DMI values on uncertainties in the input parameters. The grey regions denote the family of $d - D$ curves for 10% error in the given material parameter. Similar to existing experimental films that have demonstrated skyrmions [11]–[13], the film parameters were chosen to be $M_S = 7{\times}10^5$ A/m, $A_{ex} = 10^{-11}$ J/m, $K_U = 5 \times 10^5$ J/m^3, $T = 0.9$ nm, $\lambda = 4.9$ nm, and $N = 15$. The saturation magnetization is one of the strongest influences on estimated DMI as can be seen in Figure 5-11a since d depends on the square of M_S from Equation (5.5). Increasing M_S serves to increase magnetostatic energy thereby decreasing the domain size. A 10% change in M_S would result in $\sim$ 50% error in estimation of DMI for the same d. Figure 5-11b and c show the effects of errors in magnetic anisotropy, K_U, and exchange energy, A_{ex}, respectively. The errors in DMI calculation are smaller for these parameters. Both K_U and A_{ex} serve to increase domain wall energy and therefore increase the remnant domain sizes. However, a 10% error in K_U and 20% error in A_{ex} gives $< 20\%$ error in estimated D.

While this analysis reveals M_S to be a strong factor influencing DMI, the D

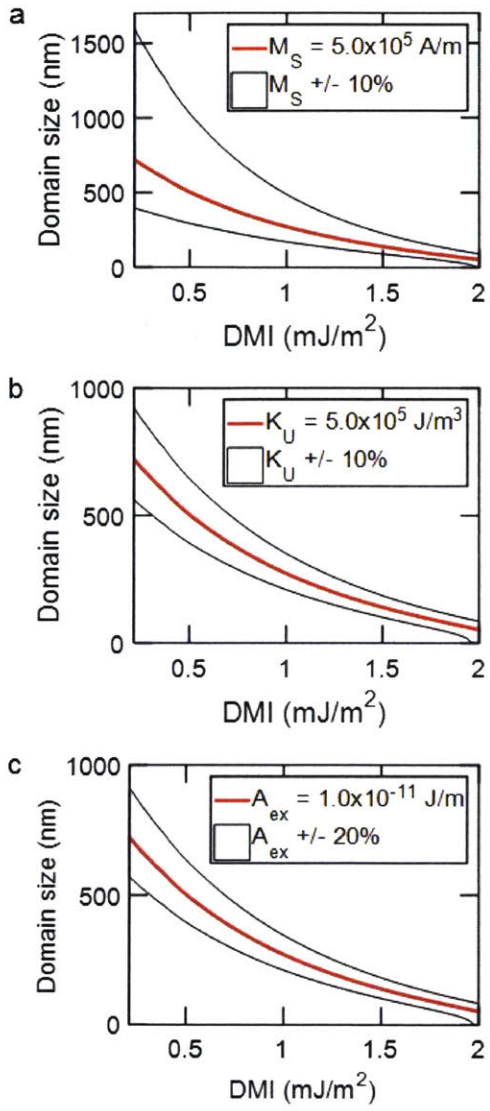

Figure 5-11: Domain size dependence on DMI and the effect of errors in different material parameters: a) saturation magnetization M_S, b) magnetic anisotropy K_U, c) exchange constant A_{ex}.

calculated for experimental films analyzed in Section 5.3 didn't change significantly within the experimental limits of error in saturation magnetization, i.e., $M_S \pm 10\%$ entered in the model. We believe that this might be due to the fact that multiple data points were used in the measurement of DMI.

5.5 Conclusion

Measurement of DMI in experimentally grown single- and multi-layered magnetic thin films is necessary for assessing their potential as materials for skyrmionic memory applications. In this chapter, we have shown that DMI strength can be measured using well-established static magnetic characterization techniques. Different models of stripe and labyrinth domains in demagnetized single and multi-layer magnetic films were introduced along with their limitations. The model that fits best to magnetic thin films with DMI and Néel domain walls is identified with the help of micromagnetic simulations. Thereafter, the best model is used to measure DMI in two experimentally grown wedged magnetic multi-layer films. The first one shows a strong DMI with $D = 1.6$ mJ/m^2 and the second one shows $D = 0$ mJ/m^2. The DMI calculated for both films is found to be consistent with values expected from theoretical predictions and observed in literature.

Thus, we have developed a simple and reliable tool for experimental materials scientists to determine DMI in experimentally grown multi-layer magnetic films. We also analyzed the role of errors in measurement of three material paramaters - M_S, A_{ex} and K_U on the estimated DMI. In the next chapter, the roles of different design variables within a magnetic multi-layer film are discussed. It is shown that the manipulation of the relative strengths of these interactions is essential to obtaining a desired stripe domain size which in effect determines the size of the skyrmions that can be realized in magnetic thin films.

Chapter 6

Design variables for tuning domain size

In Chapter 5, we showed how models of stripe domains can be combined with static magnetic characterization tools to measure difficult-to-access material parameters such as DMI, D, for various micromagnetically simulated and experimentally grown magnetic multi-layer films. In this chapter, we draw insights from the stripe domains theory and explore the dependencies of d on various design variables accessible to an experimental materials scientist. The sizes of skyrmions in the skyrmion lattices formed in magnetic multi-layers so far [11]–[13] have been influenced by stripe domain widths d in those films. Therefore, understanding how to control d by changing the design variables will help engineer multi-layers with desirable skyrmion radii.

6.1 Magnetic layer

The magnetic layer is the most important design variable. The choice of the material and its growth mechanism affects the saturation magnetization, M_S, and exchange energy, A_{ex}, while the thickness of the magnetic layer affects the scaling factor, f, and total thickness, t, of the multi-layer.

Figure 6-1 shows the variation of domain size with saturation magnetization, M_S, and exchange stiffness, A_{ex}. Increasing M_S increases the demagnetizing energy

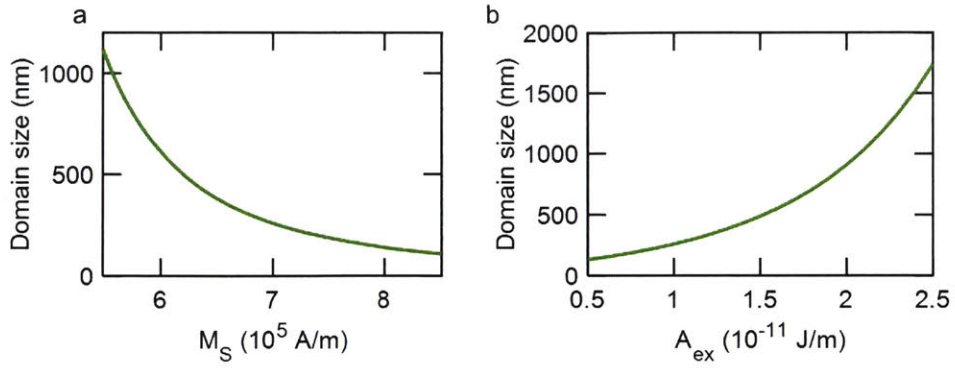

Figure 6-1: Domain size variation with saturation magnetization, M_S (a), and exchange stiffness, A_{ex} (b).

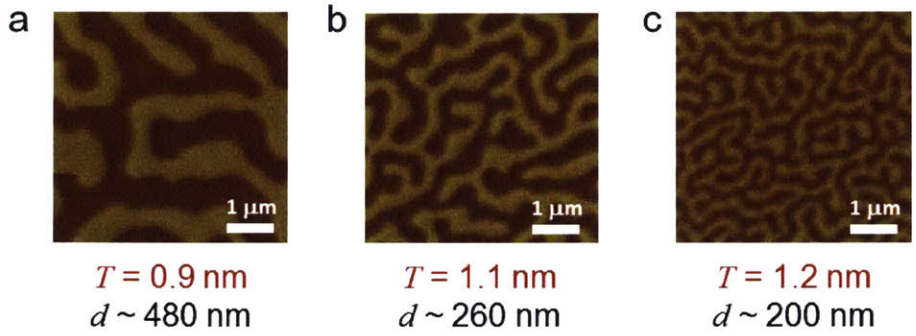

Figure 6-2: Domain size variation with thickness of magnetic layer. a-c) 5×5 μm MFM images showing decreasing domain size, d, with increasing thickness, T, of Co layer in $[\mathrm{Pt(3\ nm)/Co}(T)/\mathrm{GdOx(3nm)}]_{15}$ films.

thereby increasing the preference for domain formation, and therefore, decreasing domain size. The strong dependence of d on M_S is due to the fact that the demagnetizing energy is a function of M_S^2. Increasing A_{ex} has the opposite effect. A stronger exchange between neighboring magnetic moments increases the domain wall energy thereby making it less energetically favorable to form domain walls, and therefore increasing the domain size.

MFM images in Figure 6-2 show decreasing domain size with increasing magnetic layer thickness , T, in $[\mathrm{Pt(3\ nm)/Co}(T)/\mathrm{GdOx(3nm)}]_{15}$ films. Thicker magnetic layers lead to higher magnetostatic coupling and smaller domains.

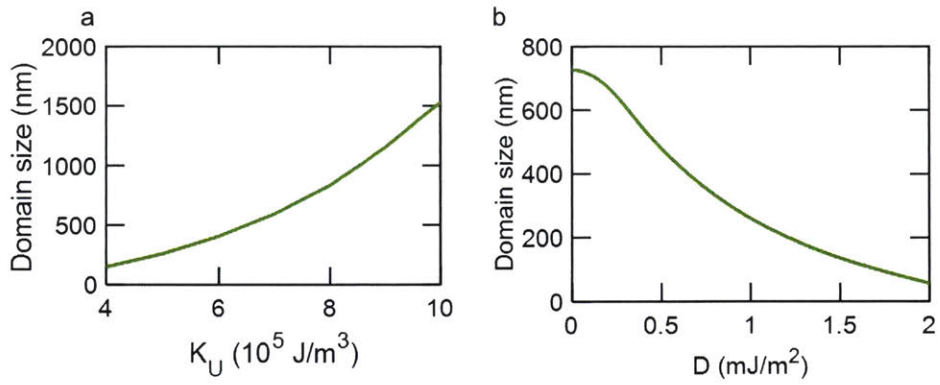

Figure 6-3: Domain size variation with interfacial anisotropy, K_U (a), and Dzyaloshinskii-Moriya interaction, D (b).

6.2 Non-magnetic layer

The non-magnetic or spacer layer in a magnetic multi-layer film affects several key parameters such as interfacial anisotropy, K_U, and DMI, D, both of which primarily come from the spin-orbit coupling of non-magnetic atoms with magnetic atoms at the interface (Section 2.1.5). Ideally, we would like to choose non-magnetic layers with high spin-orbit coupling, such as heavy metals. The choice of whether the same non-magnetic layer is used as both the top and bottom interface of the magnetic layer or not also influences DMI. When the top and bottom layers are identical, the system has inversion symmetry, therefore, the DMI from the top layer cancels out the DMI from the bottom layer as in the symmetric multi-layer film studied in Section 5.3.3. A multi-layer film with high DMI often involves inversion asymmetry, i.e., two different materials on either side of the magnetic layer, preferably having D of opposite signs [32], [81], [100], [101].

Figure 6-3 shows the variation of domain size with interfacial anisotropy, K_U, and Dzyaloshinskii-Moriya interaction, D. Increasing K_U has a similar effect as that of increasing A_{ex} (Figure 6-1b) since both these energies increase domain wall energy and reduce the tendency of domain formation. Domain size decreases with Dzyaloshinskii-Moriya interaction, D, since it reduces domain wall energy and promotes the formation of domain walls in the system. The effects of DMI on domain sizes have also been seen in Chapters 4 and 5.

6.3 Scaling factor

The thickness of the magnetic layer can be varied over a few monolayers from about 0.6 nm - 1.2 nm. The lattice constant of magnetic elements like Co and Fe is $\sim$ 0.6 nm. The minimum thickness, therefore, corresponds to $\sim$ one monolayer of magnetic element or the minimum thickness required to have a continuous film as opposed to isolated islands during sputter deposition. The upper limit is decided by the transition from out-of-plane to in-plane magnetization (Figure 2-2). The maximum possible magnetic layer thickness is the thickness at which the magnetization is still out-of-plane. Figure 6-2 shows a qualitative decrease in domain size with increasing magnetic thickness, T. Quantitatively, this decrease in domain width is seen in Figure 6-4b. Increasing the thickness of the magnetic layer while keeping the thickness of the non-magnetic layer, M_S, K_U, and A_{ex} unchanged increases f without changing magnetic energies, thereby increasing energy densities and promoting smaller domains.

The range of variation allowed in the thickness of the non-magnetic layers is larger. The minimum thickness is determined by anisotropy requirements. K_U depends on the thickness of the non-magnetic layers up to a few monolayers, after which the thickness of the non-magnetic layer should not affect the interface quality and thus not affect K_U (however, in Chapter 5, we see a dependence of K_U on non-magnetic layer thickness in experimental films). The maximum thickness is determined by the requirement for the magnetic layers to still be able to interact with each other such that magnetostatics play a role in determining domain widths. In principle, if the non-magnetic spacer layer is too thick, the individual magnetic layers in the stack would behave independently. The scaling factor, f, which is the ratio of magnetic layer thickness, T, to the total thickness of the repeating layer, λ, in a multi-layer film, provides an easy way to tune the level of dilution of magnetic energies in the system without changing other key material parameters like M_S, D, A_{ex}, and K_U. Figure 6-4a shows the variation of domain size with thickness of non-magnetic layer. Increasing the thickness of the non-magnetic layer increases the overall thickness and volume of the film without changing the magnetic energies, thereby reducing the ratio

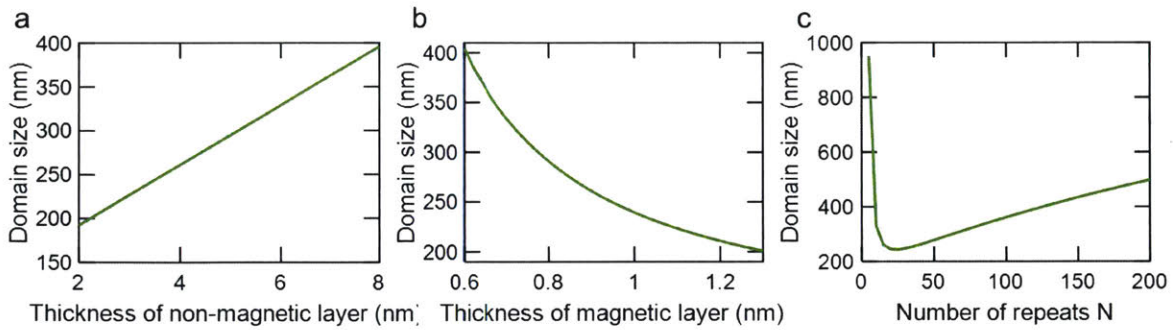

Figure 6-4: Domain size variation with thickness of non-magnetic layer (a), thickness of magnetic layer (b), and number of repeats (c).

of energy to volume. This can also be expressed as a reduction in the scaling factor, f. The result is weaker magnetostatic interactions and larger domain sizes.

Another design variable accessible to us is the number of repeats in the multi-layer magnetic film. This is the same as increasing the total thickness of the film or scaling up the system without changing the interfacial interactions. The plot of domain size as a function of number of repeats in the multi-layer film (Figure 6-4c) mimics the $d - t$ plots seen in Figure 5-3, confirming the role of N in determining the domain size.

6.4 Geometry and size

The last variable we study is geometrical confinement or reduction in the lateral dimensions of the magnetic thin film to impose restrictions on the allowed domain shapes and sizes. Stripe or labyrinth domains are the lowest energy domain configuration in infinite films, or films where the x and y dimensions are much larger than domain size. However, when the lateral dimensions of the film become comparable to domain width, the domain shapes and sizes are affected by the requirements of fitting integer domains in the confined structure. The effects of geometrical confinement on domain patterns have been extensively studied in perpendicularly magnetized films of thicknesses of the order of $\sim$ 100 nm [102]–[106] for perpendicular magnetic recording media.

Lateral confinement is of further interest because it brings additional stability to skyrmions due to topological edge replusion and curling of magnetization at the edges [73]. Several recent studies have shown the effects of geometrical confinement on skyrmions in μm or nm sized patterned magnetic thin films with DMI [107], [108]. The observations we made are qualitatively consistent with the observations in literature.

$[Pt(3\ nm)/Co(0.9\ nm)/GdOx(3\ nm)]_{15}$ films and $[Pt(3\ nm)/Co(1.2\ nm)/GdOx(3\ nm)]_{15}$ films were deposited using DC magnetron sputtering at room temperature and at 3mTorr Ar pressure. Thin films were patterned into arrays of dots which are cylindrical structures with diameters ranging from a few μm to a few hundreds of nm and thickness equal to film thickness $\sim$ 100 nm. The patterning was carried out via electron-beam lithography (EBL) and liftoff (process described in Section 3.1.2).

Figure 6-5 shows domain sizes as a function of dot diameter for $[Pt(3\ nm)/Co(0.9\ nm)/GdOx(3\ nm)]_{15}$ film. The top row shows the domain sizes right after film deposition without the application of any external magnetic fields. Even though the infinite thin film of $[Pt(3\ nm)/Co(0.9\ nm)/GdOx(3\ nm)]_{15}$ showed labyrinth domains, the patterned dots show uniform magnetization in the as-grown state. The bottom row shows the domain sizes after demagnetization by temporary application of an in-plane magnetic field of $\sim$ 4000 Oe. The method of creating multi-domain states via the application of in-plane field is explained in Chapter 4. The demagnetization process creates stripe domains (i-l) in the dots that were uniformly magnetized as grown (a-d). When the dot diameter becomes comparable ($<$ 1 μm) to equilibrium domain widths ($\sim$ 500 nm) in the infinite film, only uniform magnetization is stable (o,p).

Figure 6-6 shows dots for a $[Pt(3\ nm)/Co(1.2\ nm)/GdOx(3\ nm)]_{15}$ film with a thicker magnetic (Co) layer than the previous film. In this case, the dots show labyrinth domains even in the as-grown state (a-h) because of a higher stray field energy. No change is seen in the periodicity of the domain pattern after an in-plane field induced demagnetization for most large diameter dots (i-l).

Micromagnetic simulations confirmed the variation of domain patterns with dot diameters as seen in sputtered films in Figures 6-5 and 6-6. The material parameters

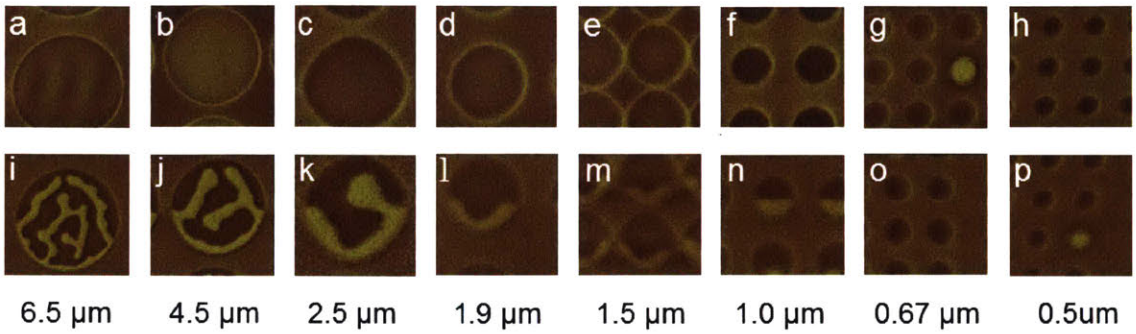

Figure 6-5: Domain patterns in µm sized dots of [Pt(3 nm)/Co(0.9 nm)/GdOx(3 nm)]$_{15}$ films. Dot diameter (bottom label) decreases from left to right. Top row (a-h) shows dots in the as-grown state while bottom row (i-p) shows dots in demagnetized state. While stripe domains are seen in larger discs, smaller dots exhibit domains aligned with the circumference (k-m) and semi-circular domains (n). The smallest dots (o,p) exhibit uniform magnetization even in the demagnetized state.

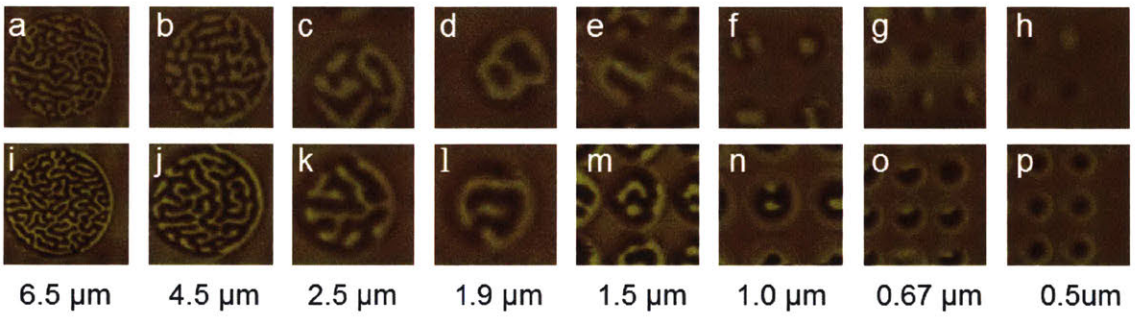

Figure 6-6: Domain patterns in µm sized dots of [Pt(3 nm)/Co(1.2 nm)/GdOx(3 nm)]$_{15}$ films. Dot diameter (bottom label) decreases from left to right. Top row (a-h) shows dots in the as-grown state while bottom row (i-p) shows dots in demagnetized state. Labyrinth domains are seen in larger discs (columns 1-3 from left). h,p) Uniform magnetization is seen in 0.5 µm discs, while some circular skyrmions are seen in f,m,n.

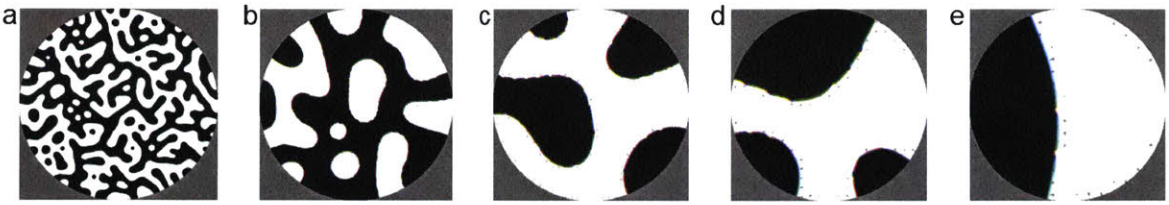

Figure 6-7: Variation of domain patterns with size in micromagnetically simulated dots with parameters $M_S = 8.655 \times 10^5$ A/m, $A_{ex} = 10^{-11}$ J/m, $K_U = 8.027 \times 10^5$ J/m^3, $T = 1.1$ nm, $\lambda = 7.1$ nm, $N = 15$, and $D =$ -0.785 mJ/m^2. Dot diameter decreases from left to right and is given by a) 6.5 µm, b) 1.9 µm, c) 1 µm, d) 0.67 µm, e) 0.5 µm. Labyrinth domain patterns are seen in larger dots (a,b) whereas discrete magnetization states are seen in smaller dots (c-e). Two skyrmions are also seen in b.

chosen for simulations were $M_S = 8.655 \times 10^5$ A/m, $A_{ex} = 10^{-11}$ J/m, $K_U = 8.027 \times 10^5$ J/m^3, $T = 1.1$ nm, $\lambda = 7.1$ nm, $N = 15$, and $D =$ -0.785 mJ/m^2, similar to the experimental films with patterned dots studied above. (The symbols are described in Chapter 5). The magnetization was chosen to be random at the start of the relaxation process. Figure 6-7 shows the variation of domain pattern with dot diameter for the micromagnetically simulated multi-layer thin film. The number of magnetic domains observed in a patterned dot is given by the ratio of dot diameter to stripe domain width in an infinite film of the same composition [102]. The stripe domain width for a demagnetized infinite thin film, with material parameters used for simulations, is 335 nm. Using this domain width, we calculated the number of magnetic domains predicted for each dot in Figure 6-7, and found this ratio to be a) 19.4 for the 6.5 µm dot, b) 5.67 for the 1.9 µm dot, c) 2.98 for the 1 µm dot, d) 2 for the 0.67 µm dot, and e) 1.49 for the 0.5 µm dot. Indeed, the number of magnetic domains seen in these dots is approximately consistent with these ratios.

For micromagnetic simulations, the magnetization state at the start of the relaxation process seemed to affect the final domain pattern, as seen in Figure 6-8 for dots of diameter 0.5 µm. We suspect that this is because the relaxation process doesn't find the lowest energy domain configuration but rather one of several local energy minima. Initializing the magnetization as random was found to generate the labyrinth domains similar to the demagnetized state in experiments. The simulation parameters used

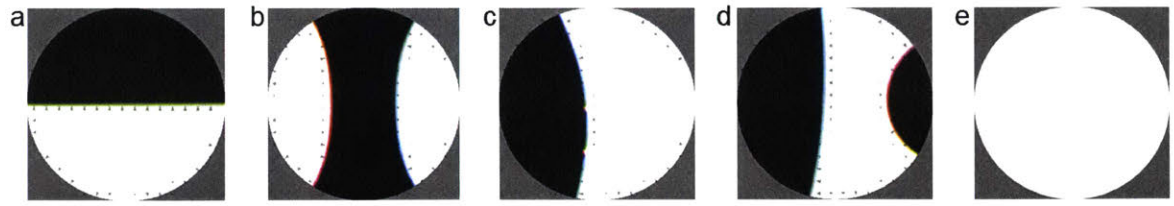

Figure 6-8: Variation of final domain patterns with initial state of magnetization in micromagnetically simulated 0.5 µm discs. The initial magnetic states were: a) uniform in the plane of the film along $\hat{i} + \hat{j}$, b) two in-plane magnetized domains, c) random magnetization, d) stripe domains, e) uniform magnetization perpendicular to the film plane ($\hat{k}$).

for Figure 6-8 are the same as those for Figure 6-7. For sputtered films, the equivalent of changing the initial magnetization is an alteration of the magnetic domain pattern via field application. For instance, in-plane (out-of-plane) fields could be used to generate magnetic domain patterns similar to Figure 6-8a (Figure 6-8e).

Circular domains seen in Figure 6-6 f,m,n and Figure 6-7 a,b are skyrmions since they have Néel domain walls. Figure 6-9a shows domain patterns in a dot of diameter 1 µm with film parameters: $M_S = 8.655 \times 10^5$ A/m, $A_{ex} = 10^{-11}$ J/m, $K_U = 1.9488 \times 10^5$ J/m^3, $T = 1.1$ nm, $\lambda = 7.1$ nm, $N = 15$, and $D = 0$ mJ/m^2. Figure 6-9b shows a 5× zoomed-in inset of Figure 6-9a. The grey triangles seen at the domain boundary indicate the direction of magnetization along the domain wall, indicating Bloch domain walls, as is expected from a system with no DMI. Figure 6-9c shows domain patterns in a dot of diameter 1 µm with film parameters held constant as Figure 6-9a but with D = -0.785 mJ/m^2. The domain sizes are smaller in Figure 6-9c as compared to Figure 6-9a since DMI lowers domain wall energy and promotes the formation of domains in the system. Figure 6-9d shows a 5× zoomed-in inset of Figure 6-9c. The grey triangles in this case are pointing perpendicular to the domain wall as expected for a Néel wall. These Néel walls were seen in all micromagnetically simulated dots with DMI.

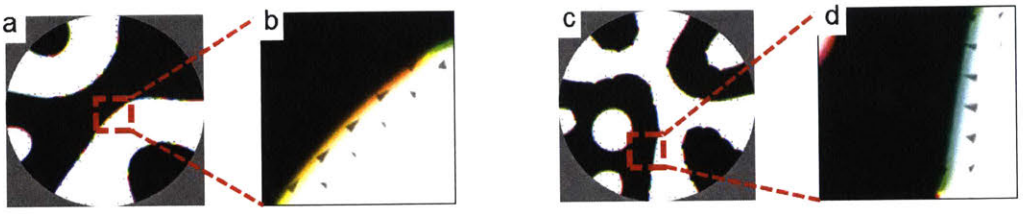

Figure 6-9: Micromagnetic simulations show that the presence of DMI in magnetic thin film changes the preferred orientation of domain walls from Bloch to Néel.

6.5 Conclusion

In summary, we investigated the role of several design variables: M_S, A_{ex}, K_U, D, the number of repeats, and the thicknesses of magnetic and non-magnetic layers in controlling the equilibrium domain size in magnetic multi-layer films. While not all these variables are independent of each other, many of them have competing effects on the domain size allowing for very specific tailoring of domain sizes in magnetic multi-layer films. Several studies have tried to capture the role of each of these variables by continuous varying any one of them while keeping the others unchanged.

Another variable that is often used to create and stabilize skyrmions and that we didn't discuss here, is an applied external out-of-plane magnetic field. Many interesting skyrmion phases (cycloids, skyrmion lattices) can be created by external magnetic field stabilization [11], [13], [107]–[109]. However, eventually for a memory device based on skyrmions in magnetic thin films, the stabilization of skyrmions with the help of external magnetic fields would be difficult to implement.

Chapter 7

Conclusion and outlook

7.1 Summary of this thesis

In this thesis, we have presented magnetic thin films as a system of interest for spintronic memory applications. We started by laying out the framework of various magnetic interactions in magnetic thin films. We highlighted the competing tendencies of exchange energy that prefers parallel neighboring spins and the Dzyaloshinskii-Moriya interaction that prefers perpendicularly aligned neighboring spins, the result of which are several interesting chiral spin textures. We also highlight the role of various other physical properties, namely spin-orbit coupling, inversion asymmetry and perpendicular magnetic anisotropy in magnetic thin films which help realize chiral spin textures. For magnetic memory applications, the most relevant of these spin structures is the skyrmion due to its small size, topological stability and potential to move at high speeds.

The experimental and simulation methods used in this thesis are outlined in Chapter 3. We then outline a way of creating chiral multi-domain phases in single- and multi-layer films by the application of a magnetic field in the plane of the film in Chapter 4. Through this chapter, the role of in-plane fields in lowering the domain wall energy of the system and thus enabling the creation of multi-domain phases is highlighted.

In Chapter 5, we develop a sense of the scale of the different competing interactions

in perpendicularly magnetized thin films and show that the net macroscopic result of minimization of energy is the formation of stripe or labyrinth domains in magnetic single- and multi-layered films. Moreover, the chiral stripe and labyrinth domains have the potential to be transformed into skyrmion lattices as has been shown by several recent works. We develop a method to accurately predict the domain size of the multi-domain stripe or labyrinth domain configuration in magnetic thin films. We take this framework further to measure the strength of the Dzyaloshinskii-Moriya interaction for micromagnetically simulated films to within 1% of the theoretically predicted value. After verifying the model with simulations, we apply it to experimentally grown films - one with inversion asymmetry and the other without. Accounting for the variations in perpendicular magnetic anisotropy due to film growth conditions, we are able to predict the DMI strength in these films reliably. The symmetric film shows no DMI while the asymmetric film shows $D = 1.6$ mJ/m^2, similar to the DMI measured via domain wall dynamics experiments for similar film structures. We also observe a small trend in anisotropy variation with thickness of non-magnetic spacer layer in both asymmetric and symmetric multi-layer films. In the symmetric film, this trend was found to correlate with the trend in DMI strength, indicating some systematic variation in interface quality with non-magnetic layer thickness.

Finally, in Chapter 6, we introduce several design variables in magnetic multi-layer films that influence the domain size. These variables are magnetic layer thickness, non-magnetic layer thickness, exchange energy, saturation magnetization, Dzyaloshinskii-Moriya interaction, perpendicular magnetic anisotropy and number of repeats. While many of these are interrelated, they still span a huge parameter space and allow for many different combinations of multi-layer magnetic films giving similar domain sizes. This gives materials engineers large flexibility in designing materials with specific combinations of material properties.

This thesis, thus, serves the purpose of providing detailed characterization of magnetic multi-layer films along with the underlying physics. By applying the theoretical models to experimentally grown films, we demonstrate the applicability of the theory and provide essential tools for further design and engineering of these films for

magnetic memory applications.

7.2 Future work

Moore's law has been the driving force for advancements in the semiconductor industry for the last few decades giving rise to smaller and faster processors every few years [110]. However, the limits of the law are being reached now as Joule heating becomes a critical limiting factor for performance and reliability of transistors [111]. In this context, the field of spintronics holds great promise to not only solve several key challenges faced by the Si-based transistor designs, but also enable faster, cheaper and cooler memory technologies [112].

7.2.1 Skyrmion based memory

The primary application of the magnetic films studied in this thesis is in domain wall-based and skyrmion-based logic and memory devices. Various designs have been envisaged for such devices including shift registers, 2D skyrmion racetrack memory (Sky-RM) [23], [113], [114], 3D domain-wall racetrack memory (DW-RM) [5], and isolated skyrmion based cells [115]. The idea of these devices would be to create skyrmions deterministically at well-defined locations in magnetic materials with external stimuli such as electric current, temperature control, geometrical confinement, magnetic field and electric field. These skyrmions would store information in the form of magnetization pointing up or down.

The goal of maximizing storage density would require the minimization of skyrmion diameter. Since skyrmions have been primarily created by length-wise shrinking of stripe domains, optimizing the magnetic multi-layer film via methods outlined in this thesis would be a way to generate the narrowest possible stripes, which would then pave the way to create the smallest skyrmions stable only by magnetostatics. Some other challenges lie in identifying reliable ways of switching skyrmions, from up to down or vice versa, without affecting the skyrmions nearby. Finally, to enable fast readout of information stored in the device, it should be possible to move a train of

skyrmions in a fast, efficient and reliable fashion.

Some of these challenges have been adressed as in the creation of skyrmions with applied fields [13], currents [11] and current-induced skyrmion motion [11], [114], [116]. However, many challenges remain. One big challenge is the problem of pinning of domain walls [28], [86], [117] in magnetic films, due to inevitable defects such as grain boundaries, which significantly inhibits fast skyrmion motion predicted by micromagnetic simulations. The other challenge is the limits of topological protection of skyrmions. Recent studies [118], [119] have shown that skyrmions are readily annihilated with certain magnetic fields and current pulses. Further in-depth understanding of the creation process of skyrmions and their response to external stimuli is needed before they can be used for memory applications.

7.2.2 Other materials of interest

While the focus of this thesis has been primarily on heavy metal/ferromagnetic metal/oxide or another heavy metal sandwich structures, there are several other interesting materials of interest for skyrmion memory applications. The choice of the magnetic medium could encompass ferrimagnets [120], bulk ferromagnets, antiferromagnets [121] and perpendicularly magnetized ferromagnetic insulators (FMI). Bulk ferromagnets like TbCo are attractive since they can provide thermal stability while achieving magnetization switching at current densities comparable to perpendicularly magnetized thin films [122]. The use of perpendicularly magnetized ferromagnetic insulators (FMI) such as thulium iron garnet in place of ferromagnetic metals has been shown [123] to have a higher efficiency of spin-orbit torques. This is because in a heavy metal/FMI layer structure, charge current flows primarily through the non-magnetic SOC material giving rise to higher spin current insertion in to the neighboring FMI layer. Thus magnetization switching occurs at lower charge current densities enabling low power spintronics devices.

The primary role of the non-magnetic layer in multi-layer magnetic films for skyrmion memory applications is to provide strong spin-orbit coupling (SOC). The spin Hall effect (SHE) is the conversion of charge current to spin current mediated

via high SOC atoms in non-magnetic layer. A non-magnetic metal with strong SOC placed next to the ferromagnetic metal can act as a source of spin current effectively producing magnetization reversal of the ferromagnetic metal at very low charge currents. Other than heavy metals, strong SOC is found in topological insulators (TI), such that in these materials, the relative orientation between an itinerant electron's spin and direction of flow is fixed [33]. This means that TIs show very strong spin Hall effects, sometimes orders of magnitude stronger than those shown by heavy metals [34]. If they could be incorporated in skyrmion devices, even smaller currents would be required to switch magnetization.

Another interesting class of materials are metallic antiferromagnets like IrMn. When placed next to a ferromagnet, they can bias the ferromagnet giving rise to an effective field that could cant the ferromagnetic magnetization. This would eliminate the need for canting by external fields to achieve deterministic spin orbit torque switching, which is a major obstacle for realizing device applications. Additionally, if the antiferromagnetic metal has a strong SHE, it could also act as a source of spin current [124]. Moreover, antiferromagnets have zero net magnetization and are therefore less susceptible to external magnetic fields. This makes them attractive candidates for application in magnetic devices.

Bibliography

[1] S. A. Wolf, J. Lu, M. R. Stan, E. Chen, and D. M. Treger, "The Promise of Nanomagnetics and Spintronics for Future Logic and Universal Memory", *Proceedings of the IEEE*, vol. 98, no. 12, pp. 2155–2168, Dec. 2010, ISSN: 0018-9219. DOI: 10.1109/JPROC.2010.2064150. [Online]. Available: http://ieeexplore.ieee.org/document/5575377/.

[2] J. Meena, S. Sze, U. Chand, and T.-Y. Tseng, "Overview of Emerging Nonvolatile Memory Technologies", *Nanoscale Research Letters*, vol. 9, no. 1, 526(33), 2014, ISSN: 1556-276X. DOI: 10.1186/1556-276X-9-526. [Online]. Available: http://nanoscalereslett.springeropen.com/articles/10.1186/1556-276X-9-526.

[3] M. Kryder and C. S. Kim, "After Hard Drives—What Comes Next?", *IEEE Transactions on Magnetics*, vol. 45, no. 10, pp. 3406–3413, Oct. 2009, ISSN: 0018-9464. DOI: 10.1109/TMAG.2009.2024163. [Online]. Available: http://ieeexplore.ieee.org/document/5257331/.

[4] S. Parkin, Xin Jiang, C. Kaiser, A. Panchula, K. Roche, and M. Samant, "Magnetically Engineered Spintronic Sensors and Memory", *Proceedings of the IEEE*, vol. 91, no. 5, pp. 661–680, May 2003, ISSN: 0018-9219. DOI: 10.1109/JPROC.2003.811807. [Online]. Available: http://ieeexplore.ieee.org/document/1200120/.

[5] S. Parkin and S.-H. Yang, "Memory on the Racetrack.", *Nature nanotechnology*, vol. 10, no. 3, pp. 195–198, Mar. 2015, ISSN: 1748-3395. DOI: 10.1038/

nnano.2015.41. [Online]. Available: http://dx.doi.org/10.1038/nnano.2015.41.

[6] S. S. P. Parkin, M. Hayashi, and L. Thomas, "Magnetic Domain-Wall Racetrack Memory", *Science (New York, N.Y.)*, vol. 320, no. 5873, pp. 190–4, Apr. 2008, ISSN: 1095-9203. DOI: 10.1126/science.1145799. [Online]. Available: http://www.ncbi.nlm.nih.gov/pubmed/18403702.

[7] G. Beach, M. Tsoi, and J. L. Erskine, "Current-Induced Domain Wall Motion", *Journal of Magnetism and Magnetic Materials*, vol. 320, no. 7, pp. 1272–1281, Apr. 2008, ISSN: 03048853. DOI: 10.1016/j.jmmm.2007.12.021. [Online]. Available: http://linkinghub.elsevier.com/retrieve/pii/S0304885307010141%20http://ac.els-cdn.com/S0304885307010141/1-s2.0-S0304885307010141-main.pdf?%7B%5C_%7Dtid=6a849d04-7601-11e7-95ef-00000aacb362%7B%5C&%7Dacdnat=1501513592%7B%5C_%7D.

[8] A. Thiaville, Y. Nakatani, J. Miltat, and Y. Suzuki, "Micromagnetic Understanding of Current-Driven Domain Wall Motion in Patterned Nanowires", *Europhysics Letters*, vol. 69, no. 6, pp. 990–996, 2005. DOI: 10.1209/epl/i2004-10452-6. [Online]. Available: http://iopscience.iop.org/0295-5075/69/6/990.

[9] I. M. Miron, T. Moore, H. Szambolics, L. D. Buda-Prejbeanu, S. Auffret, B. Rodmacq, S. Pizzini, J. Vogel, M. Bonfim, A. Schuhl, and G. Gaudin, "Fast Current-Induced Domain-Wall Motion Controlled by the Rashba Effect.", *Nature materials*, vol. 10, no. 6, pp. 419–423, Jun. 2011, ISSN: 1476-1122. DOI: 10.1038/nmat3020. [Online]. Available: http://www.ncbi.nlm.nih.gov/pubmed/21572411%20http://www.nature.com/doifinder/10.1038/nmat3020.

[10] K. Obata and G. Tatara, "Current-Induced Domain Wall Motion in Rashba Spin-Orbit System", *Physical Review B*, vol. 77, no. 21, 214429(12), Jun. 2008, ISSN: 1098-0121. DOI: 10.1103/PhysRevB.77.214429. [Online]. Available: https://link.aps.org/doi/10.1103/PhysRevB.77.214429.

[11] S. Woo, K. Litzius, B. Krüger, M.-Y. Im, L. Caretta, K. Richter, M. Mann, A. Krone, R. M. Reeve, M. Weigand, P. Agrawal, I. Lemesh, M.-A. Mawass, P. Fischer, M. Kläui, and G. S. D. Beach, "Observation of Room-Temperature Magnetic Skyrmions and Their Current-Driven Dynamics in Ultrathin Metallic Ferromagnets", *Nature Materials*, vol. 15, no. 5, pp. 501–506, Feb. 2016, ISSN: 1476-1122. DOI: 10.1038/nmat4593. [Online]. Available: http://dx.doi.org/10.1038/nmat4593%20http://www.nature.com/doifinder/10.1038/nmat4593.

[12] W. Jiang, P. Upadhyaya, W. Zhang, G. Yu, M. B. Jungfleisch, F. Y. Fradin, J. E. Pearson, Y. Tserkovnyak, K. L. Wang, O. Heinonen, S. G. E. te Velthuis, and A. Hoffmann, "Blowing Magnetic Skyrmion Bubbles", en, *Science*, vol. 349, no. 6245, pp. 283–286, Jul. 2015, ISSN: 1095-9203. DOI: 10.1126/science.aaa1442. [Online]. Available: http://www.ncbi.nlm.nih.gov/pubmed/26067256%20http://science.sciencemag.org/content/349/6245/283.abstract%20http://science.sciencemag.org/content/sci/349/6245/283.full.pdf?explicitversion=true.

[13] C. Moreau-Luchaire, C. Moutafis, N. Reyren, J. Sampaio, C. A. F. Vaz, N. V. Horne, K. Bouzehouane, K. Garcia, C. Deranlot, P. Warnicke, P. Wohlhüter, J.-M. George, M. Weigand, J. Raabe, V. Cros, and A. Fert, "Additive Interfacial Chiral Interaction in Multilayers for Stabilization of Small Individual Skyrmions at Room Temperature", *Nature nanotechnology*, vol. 11, 2016. DOI: 10.1038/NNANO.2015.313. [Online]. Available: https://www.nature.com/nnano/journal/v11/n5/pdf/nnano.2015.313.pdf.

[14] S. Krause and R. Wiesendanger, "Spintronics: Skyrmionics Gets Hot", *Nature Materials*, vol. 15, no. 5, pp. 493–494, Apr. 2016, ISSN: 1476-1122. DOI: 10.1038/nmat4615. [Online]. Available: http://www.nature.com/doifinder/10.1038/nmat4615.

[15] N. S. Kiselev, A. N. Bogdanov, R. Schäfer, and U. K. Rößler, "Chiral Skyrmions in Thin Magnetic Films: New Objects for Magnetic Storage Technologies?",

Journal of Physics D: Applied Physics, vol. 44, no. 39, p. 392 001, Oct. 2011, ISSN: 0022-3727. DOI: 10.1088/0022-3727/44/39/392001. [Online]. Available: http://stacks.iop.org/0022-3727/44/i=39/a=392001.

[16] A. Fert, V. Cros, and J. Sampaio, "Skyrmions on the Track", *Nature nanotechnology*, vol. 8, no. 3, pp. 152–156, Mar. 2013, ISSN: 1748-3395. DOI: 10.1038/nnano.2013.29. [Online]. Available: http://dx.doi.org/10.1038/nnano.2013.29%20https://www.nature.com/nnano/journal/v8/n3/pdf/nnano.2013.29.pdf.

[17] G. Finocchio, F. Büttner, R. Tomasello, M. Carpentieri, and M. Klaui, "Magnetic Skyrmions: from Fundamental to Applications", *J. Phys. D: Appl. Phys*, vol. 49, no. 42, p. 423 001, 2016. [Online]. Available: http://iopscience.iop.org/0022-3727/49/42/423001.

[18] S. Mühlbauer, B. Binz, F. Jonietz, C. Pfleiderer, A. Rosch, A. Neubauer, R. Georgii, and P. Böni, "Skyrmion Lattice in a Chiral Magnet.", *Science (New York, N.Y.)*, vol. 323, no. 5916, pp. 915–9, Feb. 2009, ISSN: 1095-9203. DOI: 10.1126/science.1166767. [Online]. Available: http://www.sciencemag.org/content/323/5916/915.full%20http://www.ncbi.nlm.nih.gov/pubmed/19213914%20http://science.sciencemag.org/content/323/5916/915.full%20http://www.sciencemag.org/content/323/5916/915.abstract.

[19] X. Z. Yu, Y. Onose, N. Kanazawa, J. H. Park, J. H. Han, Y. Matsui, N. Nagaosa, and Y. Tokura, "Real-Space Observation of a Two-Dimensional Skyrmion Crystal", *Nature*, vol. 465, no. 7300, pp. 901–904, Jun. 2010, ISSN: 1476-4687. DOI: 10.1038/nature09124. [Online]. Available: http://www.ncbi.nlm.nih.gov/pubmed/20559382%20https://www.nature.com/nature/journal/v465/n7300/pdf/nature09124.pdf.

[20] S. Heinze, K. Von Bergmann, M. Menzel, J. Brede, A. Kubetzka, R. Wiesendanger, G. Bihlmayer, and S. Blügel, "Spontaneous Atomic-Scale Magnetic Skyrmion Lattice in Two Dimensions", en, *Nature Physics*, vol. 7, no. 9, pp. 713–718, Jul. 2011, ISSN: 1745-2473. DOI: 10.1038/nphys2045. [Online]. Available:

http://www.nature.com/nphys/journal/v7/n9/full/nphys2045.html%7B%5C#%7Dincom.

[21] S. Emori, U. Bauer, S.-M. Ahn, E. Martinez, and G. S. D. Beach, "Current-Driven Dynamics of Chiral Ferromagnetic Domain Walls", *Nature materials*, vol. 12, no. 7, pp. 611–6, Jul. 2013, ISSN: 1476-1122. DOI: 10.1038/nmat3675. [Online]. Available: http://www.ncbi.nlm.nih.gov/pubmed/23770726.

[22] K.-S. Ryu, L. Thomas, S.-H. Yang, and S. Parkin, "Chiral Spin Torque at Magnetic Domain Walls", *Nature nanotechnology*, vol. 8, no. 7, pp. 527–33, Jul. 2013, ISSN: 1748-3395. DOI: 10.1038/NNANO.2013.102. [Online]. Available: http://dx.doi.org/10.1038/nnano.2013.102%20https://www.nature.com/nnano/journal/v8/n7/pdf/nnano.2013.102.pdf.

[23] X. Zhang, G. P. Zhao, H. Fangohr, J. P. Liu, W. X. Xia, J. Xia, and F. J. Morvan, "Skyrmion-Skyrmion and Skyrmion-Edge Repulsions in Skyrmion-Based Racetrack Memory", *Scientific Reports*, vol. 5, 07643(6), 2015. DOI: 10.1038/srep07643. [Online]. Available: https://www.nature.com/articles/srep07643.pdf.

[24] R. C. O'Handley, *Modern Magnetic Materials : Principles and Applications*. Wiley, 2000, ISBN: 0471155667.

[25] S.-i. Iwasaki, "Perpendicular Magnetic Recording-its Development and Realization.", *Proceedings of the Japan Academy. Series B, Physical and biological sciences*, vol. 85, no. 2, pp. 37–54, 2009, ISSN: 1349-2896. DOI: 10.2183/pjab.85.37. [Online]. Available: http://www.ncbi.nlm.nih.gov/pubmed/19212097%20http://www.pubmedcentral.nih.gov/articlerender.fcgi?artid=PMC3524294.

[26] M. T. Johnson, P. J. H. Bloemen, F. J. a. D. Broeder, and J. J. D. Vries, "Magnetic Anisotropy in Metallic Multilayers", *Reports on Progress in Physics*, vol. 59, no. 11, pp. 1409–1458, 1999, ISSN: 0034-4885. DOI: 10.1088/0034-4885/59/11/002.

[27] S. Mcvitie and J. N. Chapman, "Measurement of Domain Wall Widths in Permalloy Using Differential Phase Contrast Imaging in STEM", *Journal of Magnetism and Magnetic Materials*, vol. 83, no. 1-3, pp. 97–98, 1990. [Online]. Available: http://ac.els-cdn.com/030488539090445V/1-s2.0-030488539090445V-main.pdf?%7B%5C_%7Dtid=265f14c6-9319-11e7-9f0e-00000aab0f02%7B%5C&%7Dacdnat=1504712368%7B%5C_%7D.

[28] T. Koyama, D. Chiba, K. Ueda, K. Kondou, H. Tanigawa, S. Fukami, T. Suzuki, N. Ohshima, N. Ishiwata, Y. Nakatani, K. Kobayashi, and T. Ono, "Observation of the Intrinsic Pinning of a Magnetic Domain Wall in a Ferromagnetic Nanowire.", *Nature materials*, vol. 10, no. 3, pp. 194–197, Mar. 2011, ISSN: 1476-1122. DOI: 10.1038/NMAT2961. [Online]. Available: https://www.nature.com/nmat/journal/v10/n3/pdf/nmat2961.pdf%20http://www.ncbi.nlm.nih.gov/pubmed/21336264.

[29] P. Sethi, S. Krishnia, S. H. Li, and W. S. Lew, "Modulation of Spin-Orbit Torque Efficiency by Thickness Control of Heavy Metal Layers in Co/Pt Multilayers", *Journal of Magnetism and Magnetic Materials*, vol. 426, pp. 497–503, 2017. DOI: 10.1016/j.jmmm.2016.11.130. [Online]. Available: www.elsevier.com/locate/jmmm.

[30] L. Liu, R. A. Buhrman, and D. C. Ralph, "Review and Analysis of Measurements of the Spin Hall Effect in Platinum", *arXiv preprint arXiv: 1111.3702*, p. 32, Nov. 2011. arXiv: 1111.3702. [Online]. Available: http://arxiv.org/abs/1111.3702.

[31] A. Soumyanarayanan, N. Reyren, A. Fert, and C. Panagopoulos, "Emergent Phenomena Induced by Spin– Orbit Coupling at Surfaces and Interfaces", *Nature*, vol. 539, pp. 509–517, 2016. DOI: 10.1038/nature19820. [Online]. Available: https://www.nature.com/nature/journal/v539/n7630/pdf/nature19820.pdf.

[32] S. Woo, M. Mann, A. J. Tan, L. Caretta, and G. S. D. Beach, "Enhanced Spin-Orbit Torques in Pt/Co/Ta Heterostructures", *Applied Physics Letters*,

vol. 105, no. 21, 212404(5), 2014. DOI: 10.1063/1.4902529. [Online]. Available: http://beach.mit.edu/wp-content/uploads/2014/11/PtCoTa%7B%5C_%7DSOT.pdf.

[33] J. E. Moore, "The birth of Topological Insulators.", *Nature*, vol. 464, no. 7286, pp. 194–198, Mar. 2010, ISSN: 0028-0836. DOI: 10.1038/nature08916. [Online]. Available: http://www.nature.com/doifinder/10.1038/nature08916%20http://dx.doi.org/10.1038/nature08916.

[34] L. Liu, A. Richardella, I. Garate, Y. Zhu, N. Samarth, and C.-T. Chen, "Spin-Polarized Tunneling Study of Spin-Momentum Locking in Topological Insulators", *Physical Review B*, vol. 91, no. 23, p. 235 437, Jun. 2015, ISSN: 1098-0121. DOI: 10.1103/PhysRevB.91.235437. [Online]. Available: http://link.aps.org/doi/10.1103/PhysRevB.91.235437.

[35] A. A. Burkov and D. G. Hawthorn, "Spin and Charge Transport on the Surface of a Topological Insulator", *Physical Review Letters*, vol. 105, no. 6, 066802(4), 2010. DOI: 10.1103/PhysRevLett.105.066802. [Online]. Available: https://journals.aps.org/prl/pdf/10.1103/PhysRevLett.105.066802.

[36] I. Dzyaloshinsky, "A Thermodynamic Theory of "Weak" Ferromagnetism of Antiferromagnetics", *Journal of Physics and Chemistry of Solids*, vol. 4, no. 4, pp. 241–255, Jan. 1958, ISSN: 00223697. DOI: 10.1016/0022-3697(58)90076-3. [Online]. Available: http://linkinghub.elsevier.com/retrieve/pii/0022369758900763.

[37] T. Moriya, "Anisotropic Superexchange Interaction and Weak Ferromagnetism", *Physical Review*, vol. 120, no. 1, pp. 91–98, Oct. 1960, ISSN: 0031-899X. DOI: 10.1103/PhysRev.120.91. [Online]. Available: https://link.aps.org/doi/10.1103/PhysRev.120.91.

[38] A. Fert and P. M. Levy, "Role of Anisotropic Exchange Interactions in Determining the Properties of Spin-Glasses", *Physical Review Letters*, vol. 44, no. 23, pp. 1538–1541, Jun. 1980, ISSN: 0031-9007. DOI: 10.1103/PhysRevLett.

44 . 1538. [Online]. Available: https : / / link . aps . org / doi / 10 . 1103 / PhysRevLett . 44 . 1538.

[39] E. Stoner and E. Wohlfarth, "A Mechanism of Magnetic Hysteresis in Heterogeneous Alloys", *Philosophical Transactions of the Royal Society of London. Series A, Mathematical and Physical Sciences*, vol. 240, no. 826, pp. 599–642, 1948. [Online]. Available: http : / / spin . nanophys . kth . se / spin / stoner - wohlfarth . pdf.

[40] R. M. H. New, "Submicron Patterning of Thin Cobalt Films for Magnetic Storage", *Journal of Vacuum Science & Technology B: Microelectronics and Nanometer Structures*, vol. 12, no. 6, pp. 3196–3201, Nov. 1994, ISSN: 0734211X. DOI: 10 . 1116 / 1 . 587499. [Online]. Available: http : / / scitation . aip . org / content / avs / journal / jvstb / 12 / 6 / 10 . 1116 / 1 . 587499.

[41] D. Thompson, L. Romankiw, and A. Mayadas, "Thin Film Magnetoresistors in Memory, Storage, and Related Applications", *IEEE Transactions on Magnetics*, vol. 11, no. 4, pp. 1039–1050, Jul. 1975, ISSN: 0018-9464. DOI: 10 . 1109 / TMAG . 1975 . 1058786. [Online]. Available: http : / / ieeexplore . ieee . org / document / 1058786 /.

[42] N. Imamura and C. Ota, "Experimental Study on Magneto-Optical Disk Exerciser with the Laser Diode and Amorphous Magnetic Thin Films", *Japanese Journal of Applied Physics*, vol. 19, no. 12, pp. L731–L734, Dec. 1980, ISSN: 0021-4922. DOI: 10 . 1143 / JJAP . 19 . L731. [Online]. Available: http : / / stacks . iop . org / 1347 - 4065 / 19 / L731.

[43] R. C. Sherwood, E. A. Nesbitt, J. H. Wernick, D. D. Bacon, A. J. Kurtzig, and R. Wolfe, "MnAlGe Films for Magneto-Optic Applications", *Journal of Applied Physics*, vol. 42, no. 4, pp. 1704–1705, Mar. 1971, ISSN: 0021-8979. DOI: 10 . 1063 / 1 . 1660401. [Online]. Available: http : / / aip . scitation . org / doi / 10 . 1063 / 1 . 1660401.

[44] J. F. Scott and C. A. P. D. Araujo, *Ferroelectric Memories*, 1989. DOI: 10.2307/1704896. [Online]. Available: http://www.jstor.org/stable/pdf/1704896.pdf.

[45] N. Setter, D. Damjanovic, L. Eng, G. Fox, S. Gevorgian, S. Hong, A. Kingon, H. Kohlstedt, N. Y. Park, G. B. Stephenson, I. Stolitchnov, A. K. Taganstev, D. V. Taylor, T. Yamada, and S. Streiffer, "Ferroelectric Thin Films: Review of Materials, Properties, and Applications", *Journal of Applied Physics*, vol. 100, no. 5, 051606(46), Sep. 2006, ISSN: 0021-8979. DOI: 10.1063/1.2336999. [Online]. Available: http://aip.scitation.org/doi/10.1063/1.2336999.

[46] S. S. P. Parkin, K. P. Roche, M. G. Samant, P. M. Rice, R. B. Beyers, R. E. Scheuerlein, E. J. O'Sullivan, S. L. Brown, J. Bucchigano, D. W. Abraham, Y. Lu, M. Rooks, P. L. Trouilloud, R. A. Wanner, and W. J. Gallagher, "Exchange-Biased Magnetic Tunnel Junctions and Application to Nonvolatile Magnetic Random Access Memory (invited)", *Journal of Applied Physics*, vol. 85, no. 8, pp. 5828–5833, Apr. 1999. DOI: 10.1063/1.369932. [Online]. Available: http://aip.scitation.org/doi/abs/10.1063/1.369932.

[47] S. Tehrani, J. Slaughter, M. Deherrera, B. Engel, N. Rizzo, J. Salter, M. Durlam, R. Dave, J. Janesky, B. Butcher, K. Smith, and G. Grynkewich, "Magnetoresistive Random Access Memory Using Magnetic Tunnel Junctions", *Proceedings of the IEEE*, vol. 91, no. 5, pp. 703–714, May 2003, ISSN: 0018-9219. DOI: 10.1109/JPROC.2003.811804. [Online]. Available: http://ieeexplore.ieee.org/document/1200123/.

[48] J. Sampaio, V. Cros, S. Rohart, A. Thiaville, and A. Fert, "Nucleation, Stability and Current-Induced Motion of Isolated Magnetic Skyrmions in Nanostructures", *Nature nanotechnology*, vol. 8, no. 11, pp. 839–44, Nov. 2013, ISSN: 1748-3395. DOI: 10.1038/nnano.2013.210. [Online]. Available: http://dx.doi.org/10.1038/nnano.2013.210.

[49] A. Thiaville, S. Rohart, É. Jué, V. Cros, and A. Fert, "Dynamics of Dzyaloshinskii Domain Walls in Ultrathin Magnetic Films", en, *EPL (Europhysics Let-*

ters), vol. 100, no. 5, p. 57 002, Dec. 2012, ISSN: 0295-5075. DOI: 10.1209/0295-5075/100/57002. [Online]. Available: http://iopscience.iop.org/article/10.1209/0295-5075/100/57002.

[50] I. M. Miron, K. Garello, G. Gaudin, P.-J. Zermatten, M. V. Costache, S. Auffret, S. Bandiera, B. Rodmacq, A. Schuhl, and P. Gambardella, "Perpendicular Switching of a Single Ferromagnetic Layer Induced by In-Plane Current Injection", *Nature*, vol. 476, no. 7359, pp. 189–193, Aug. 2011, ISSN: 1476-4687. DOI: 10.1038/nature10309. [Online]. Available: http://dx.doi.org/10.1038/nature10309.

[51] C.-F. Pai, L. Liu, Y. Li, H. W. Tseng, D. C. Ralph, and R. A. Buhrman, "Spin Transfer Torque Devices Utilizing the Giant Spin Hall Effect of Tungsten", *Applied Physics Letters*, vol. 101, no. 12, p. 122 404, Sep. 2012, ISSN: 00036951. DOI: 10.1063/1.4753947. [Online]. Available: http://scitation.aip.org/content/aip/journal/apl/101/12/10.1063/1.4753947.

[52] C. Kooy and U. Enz, "Experimental and Theoretical Study of the Domain Configuration in Thin Layers of BaFe_12O_9", *Philips Research Reports*, vol. 15, pp. 7–29, 1960, ISSN: 07408188. DOI: 10.1080/10643389.2012.728825.

[53] Z. Malek and V. Kambersky, "On the theory of the Domain Structure of Thin Films of Magnetically Uni-axial Materials", *Czechosl. Journ. Phys.*, vol. 8, no. 1, pp. 416–421, 1958.

[54] D. M. Donnet, K. M. Krishnan, and Y. Yajima, "Domain Structures in Epitaxially Grown Cobalt Thin Films", *Journal of Physics D: Applied Physics*, vol. 28, no. 9, pp. 1942–1950, Sep. 1995, ISSN: 0022-3727. DOI: 10.1088/0022-3727/28/9/023. [Online]. Available: http://stacks.iop.org/0022-3727/28/i=9/a=023?key=crossref.6737c797c184aefd783d25c34932b839.

[55] M. Hehn, S. Padovani, K. Ounadjela, and J. P. Bucher, "Nanoscale Magnetic Domain Structures in Epitaxial Cobalt Films", *Physical Review B*, vol. 54, no. 5, pp. 3428–3433, Aug. 1996, ISSN: 0163-1829. DOI: 10.1103/PhysRevB.54.

3428. [Online]. Available: https://link.aps.org/doi/10.1103/PhysRevB.54.3428.

[56] N. Saito, H. Fujiwara, and Y. Sugita, "A New Type of Magnetic Domain Structure in Negative Magnetostriction Ni-Fe Films", *Journal of the Physical Society of Japan*, vol. 19, no. 7, pp. 1116–1125, Jul. 1964, ISSN: 0031-9015. DOI: 10.1143/JPSJ.19.1116. [Online]. Available: http://journals.jps.jp/doi/10.1143/JPSJ.19.1116.

[57] V. Kamberský, P. de Haan, J. Šimšová, S. Porthun, R. Gemperle, and J. Lodder, "Domain Wall Theory and Exchange Stiffness in Co/Pd Multilayers", *Journal of Magnetism and Magnetic Materials*, vol. 157-158, pp. 301–302, May 1996, ISSN: 03048853. DOI: 10.1016/0304-8853(95)01162-5. [Online]. Available: http://linkinghub.elsevier.com/retrieve/pii/0304885395011625.

[58] H. Kwon and C. Won, "Effects of Dzyaloshinskii–Moriya interaction on Magnetic Stripe Domains", *Journal of Magnetism and Magnetic Materials*, vol. 351, pp. 8–15, Feb. 2014, ISSN: 03048853. DOI: 10.1016/j.jmmm.2013.09.056. [Online]. Available: http://linkinghub.elsevier.com/retrieve/pii/S0304885313007154.

[59] C. Castro, R. Sanjines, C. Pulgarin, P. Osorio, S. Giraldo, and J. Kiwi, "Structure–Reactivity Relations for DC-Magnetron Sputtered Cu-layers During E. coli Inactivation in the Dark and Under Light", *Journal of Photochemistry and Photobiology A: Chemistry*, vol. 216, no. 2-3, pp. 295–302, Dec. 2010, ISSN: 10106030. DOI: 10.1016/j.jphotochem.2010.06.030. [Online]. Available: http://linkinghub.elsevier.com/retrieve/pii/S1010603010002376.

[60] S. Woo, "Manipulation of Spin Textures by Unconventional Spin Torques", PhD thesis, Massachusetts Institute of Technology, 2015. [Online]. Available: https://dspace.mit.edu/bitstream/handle/1721.1/98577/920881880-MIT.pdf;sequence=1.

[61] S. Foner, "Versatile and Sensitive Vibrating-Sample Magnetometer", *Review of Scientific Instruments*, vol. 30, no. 7, pp. 548–557, Jul. 1959, ISSN: 0034-6748. DOI: 10.1063/1.1716679. [Online]. Available: http://aip.scitation.org/doi/10.1063/1.1716679.

[62] W. H. Hayt, *Engineering Electromagnetics*. McGraw-Hill, 1989, p. 472, ISBN: 9780070274068.

[63] E. C. Jordan and K. G. Balmain, *Electromagnetic Waves and Radiating Systems*. Prentice-Hall, 1968. [Online]. Available: http://trove.nla.gov.au/work/10781571?selectedversion=NBD702783.

[64] C. Nistor, G. S. D. Beach, and J. L. Erskine, "Versatile Magneto-optic Kerr Effect Polarimeter for Studies of Domain-Wall Dynamics in Magnetic Nanostructures", *Review of Scientific Instruments*, vol. 77, no. 10, 103901(11), Oct. 2006, ISSN: 0034-6748. DOI: 10.1063/1.2356856. [Online]. Available: http://aip.scitation.org/doi/10.1063/1.2356856.

[65] S. D. Bader and J. L. Erskine, "Magneto-Optical Effects in Ultrathin Magnetic Structures", in *Ultrathin Magnetic Structures II*, Berlin, Heidelberg: Springer Berlin Heidelberg, 1994, pp. 297–325. DOI: 10.1007/3-540-27166-X_4. [Online]. Available: http://link.springer.com/10.1007/3-540-27166-X%7B%5C_%7D4.

[66] S. Emori, "Magnetic Domain Walls Driven by Interfacial Phenomena", PhD thesis, Massachusetts Institute of Technology, 2013. [Online]. Available: https://dspace.mit.edu/handle/1721.1/88371.

[67] Y. Martin and H. K. Wickramasinghe, "Magnetic Imaging by "Force Microscopy" with 1000 Å Resolution", *Applied Physics Letters*, vol. 50, no. 20, pp. 1455–1457, May 1987, ISSN: 0003-6951. DOI: 10.1063/1.97800. [Online]. Available: http://aip.scitation.org/doi/10.1063/1.97800.

[68] W. F. Brown, *Micromagnetics*. New York : Interscience Publishers, 1963.

[69] L. Landau and E. Lifshits, "On the Theory of the Dispersion of Magnetic Permeability in Ferromagnetic Bodies", *Phys. Zeitsch. Der Sow*, vol. 53, no. Special Issue, pp. 153–169, 1935. [Online]. Available: http://www.ujp.bitp.kiev.ua/files/journals/53/si/53SI06p.pdf.

[70] T. Gilbert, "A Phenomenological Theory of Damping in Ferromagnetic Materials", *IEEE Transactions on Magnetics*, vol. 40, no. 6, pp. 3443–3449, Nov. 2004, ISSN: 0018-9464. DOI: 10.1109/TMAG.2004.836740. [Online]. Available: http://ieeexplore.ieee.org/document/1353448/.

[71] A. Vansteenkiste, J. Leliaert, M. Dvornik, M. Helsen, F. Garcia-Sanchez, and B. Van Waeyenberge, "The Design and Verification of MuMax3", *AIP Advances*, vol. 4, no. 10, 107133(22), Oct. 2014, ISSN: 2158-3226. DOI: 10.1063/1.4899186. [Online]. Available: http://aip.scitation.org/doi/10.1063/1.4899186.

[72] P. Agrawal, U. Bauer, and G. S. D. Beach, "Spontaneous Domain Nucleation under In-Plane Fields in Ultrathin Films with Dzyaloshinskii-Moriya Interaction", *Journal of Applied Physics*, vol. 117, no. 17, p. 17C744, May 2015, ISSN: 0021-8979. DOI: 10.1063/1.4917057. [Online]. Available: http://dx.doi.org/10.1063/1.4917057%20http://scitation.aip.org/content/aip/journal/jap/117/17?ver=pdfcov%20http://scitation.aip.org/content/aip/journal/jap/117/17/10.1063/1.4917057.

[73] S. Rohart and A. Thiaville, "Skyrmion Confinement in Ultrathin Film Nanostructures in the Presence of Dzyaloshinskii-Moriya Interaction", *Physical Review B*, vol. 88, no. 18, 184422(8), Nov. 2013, ISSN: 1098-0121. DOI: 10.1103/PhysRevB.88.184422. [Online]. Available: https://link.aps.org/doi/10.1103/PhysRevB.88.184422.

[74] S. Emori, E. Martinez, K.-J. Lee, H.-W. Lee, U. Bauer, S.-M. Ahn, P. Agrawal, D. C. Bono, and G. S. D. Beach, "Spin Hall Torque Magnetometry of Dzyaloshinskii Domain Walls", *Physical Review B*, vol. 90, no. 18, p. 184 427, Nov. 2014,

ISSN: 1098-0121. DOI: 10.1103/PhysRevB.90.184427. [Online]. Available: http://journals.aps.org/prb/abstract/10.1103/PhysRevB.90.184427.

[75] N. Perez, E. Martinez, L. Torres, S.-H. Woo, S. Emori, and G. S. D. Beach, "Chiral Magnetization Textures Stabilized by the Dzyaloshinskii-Moriya Interaction During Spin-Orbit Torque Switching", *Applied Physics Letters*, vol. 104, no. 9, p. 092403, Mar. 2014, ISSN: 0003-6951. DOI: 10.1063/1.4867199. [Online]. Available: http://scitation.aip.org/content/aip/journal/apl/104/9/10.1063/1.4867199.

[76] S.-g. Je, D.-h. Kim, S.-C. Yoo, B.-C. Min, S.-b. Choe, K.-J. Lee, and S.-b. Choe, "Asymmetric Magnetic Domain-Wall Motion by the Dzyaloshinskii-Moriya Interaction", *Physical Review B*, vol. 88, no. 21, p. 214401, Dec. 2013, ISSN: 1098-0121. DOI: 10.1103/PhysRevB.88.214401. [Online]. Available: https://link.aps.org/doi/10.1103/PhysRevB.88.214401%20http://journals.aps.org/prb/abstract/10.1103/PhysRevB.88.214401.

[77] O. Hellwig, A. Berger, J. B. Kortright, and E. E. Fullerton, "Domain Structure and Magnetization Reversal of Antiferromagnetically Coupled Perpendicular Anisotropy Films", *Journal of Magnetism and Magnetic Materials*, vol. 319, no. 1-2, pp. 13–55, Dec. 2007, ISSN: 03048853. DOI: 10.1016/j.jmmm.2007.04.035. [Online]. Available: http://www.sciencedirect.com/science/article/pii/S030488530700649X.

[78] A. Rosch, "Skyrmions: Moving with the Current.", *Nature nanotechnology*, vol. 8, no. 3, pp. 160–1, Mar. 2013, ISSN: 1748-3395. DOI: 10.1038/nnano.2013.21. [Online]. Available: http://dx.doi.org/10.1038/nnano.2013.21.

[79] H. Yang, A. Thiaville, S. Rohart, A. Fert, and M. Chshiev, "Anatomy of Dzyaloshinskii-Moriya Interaction at Co / Pt Interfaces", *Physical Review Letters*, vol. 115, no. 26, p. 267210, Dec. 2015, ISSN: 0031-9007. DOI: 10.1103/PhysRevLett.115.267210. [Online]. Available: https://link.aps.org/doi/10.1103/PhysRevLett.115.267210.

[80] M. Heide, G. Bihlmayer, and S. Blügel, "Describing Dzyaloshinskii–Moriya Spirals from First Principles", *Physica B: Condensed Matter*, vol. 404, no. 18, pp. 2678–2683, 2009, ISSN: 09214526. DOI: 10.1016/j.physb.2009.06.070. [Online]. Available: http://www.sciencedirect.com/science/article/pii/S0921452609004177.

[81] A. Hrabec, N. A. Porter, A. Wells, M. J. Benitez, G. Burnell, S. McVitie, D. McGrouther, T. A. Moore, and C. H. Marrows, "Measuring and Tailoring the Dzyaloshinskii-Moriya Interaction in Perpendicularly Magnetized Thin Films", *Physical Review B*, vol. 90, no. 2, p. 020 402, Jul. 2014, ISSN: 1098-0121. DOI: 10.1103/PhysRevB.90.020402. [Online]. Available: https://link.aps.org/doi/10.1103/PhysRevB.90.020402.

[82] R. Lavrijsen, D. M. F. Hartmann, A. van den Brink, Y. Yin, B. Barcones, R. A. Duine, M. A. Verheijen, H. J. M. Swagten, and B. Koopmans, "Asymmetric Magnetic Bubble Expansion under In-Plane Field in Pt/Co/Pt: Effect of Interface Engineering", *Physical Review B*, vol. 91, no. 10, 104414(8), Mar. 2015, ISSN: 1098-0121. DOI: 10.1103/PhysRevB.91.104414. [Online]. Available: http://journals.aps.org/prb/abstract/10.1103/PhysRevB.91.104414%7B%5C#%7Dfulltext%20https://link.aps.org/doi/10.1103/PhysRevB.91.104414.

[83] J. M. Lee, C. Jang, B.-C. Min, S.-W. Lee, K.-J. Lee, and J. Chang, "All-Electrical Measurement of Interfacial Dzyaloshinskii-Moriya Interaction Using Collective Spin-Wave Dynamics", *Nano letters*, vol. 16, pp. 62–67, 2016. DOI: 10.1021/acs.nanolett.5b02732. [Online]. Available: http://pubs.acs.org/doi/pdf/10.1021/acs.nanolett.5b02732.

[84] H. T. Nembach, J. M. Shaw, M. Weiler, E. Jué, and T. J. Silva, "Linear Relation between Heisenberg Exchange and Interfacial Dzyaloshinskii–Moriya Interaction in Metal Films", *Nature Physics*, vol. 11, no. 10, pp. 825–829, Aug. 2015, ISSN: 1745-2473. DOI: 10.1038/nphys3418. [Online]. Available: http://www.nature.com/doifinder/10.1038/nphys3418.

[85] Y. Yoshimura, K.-J. Kim, T. Taniguchi, T. Tono, K. Ueda, R. Hiramatsu, T. Moriyama, K. Yamada, Y. Nakatani, and T. Ono, "Soliton-Like Magnetic Domain Wall Motion Induced by the Interfacial Dzyaloshinskii–Moriya Interaction", *Nature Physics*, vol. 12, 2016. DOI: 10.1038/NPHYS3535. [Online]. Available: https://www.nature.com/nphys/journal/v12/n2/pdf/nphys3535.pdf.

[86] C. Hanneken, A. Kubetzka, K. von Bergmann, and R. Wiesendanger, "Pinning and Movement of Individual Nanoscale Magnetic Skyrmions via Defects", *New Journal of Physics*, vol. 18, no. 5, 055009(6), May 2016, ISSN: 1367-2630. DOI: 10.1088/1367-2630/18/5/055009. [Online]. Available: http://stacks.iop.org/1367-2630/18/i=5/a=055009?key=crossref.de4228d74a32563495ffbddec7755da6.

[87] I. Lemesh, F. Büttner, and G. S. D. Beach, "Accurate Model of the Stripe Domain Phase of Perpendicularly Magnetized Multilayers", *Physical Review B*, vol. 95, no. 17, p. 174 423, May 2017, ISSN: 2469-9950. DOI: 10.1103/PhysRevB.95.174423. [Online]. Available: http://link.aps.org/doi/10.1103/PhysRevB.95.174423.

[88] C. Kittel, "Physical Theory of Ferromagnetic Domains", *Reviews of Modern Physics*, vol. 21, no. 4, pp. 541–583, Oct. 1949, ISSN: 0034-6861. DOI: 10.1103/RevModPhys.21.541. [Online]. Available: https://link.aps.org/doi/10.1103/RevModPhys.21.541.

[89] A. Suna, "Perpendicular Magnetic Ground State of a Multilayer Film", *Journal of Applied Physics*, vol. 59, no. 2, pp. 313–316, 1986, ISSN: 00218979. DOI: 10.1063/1.336684.

[90] T. H. Johansen, A. V. Pan, and Y. M. Galperin, "Exact Asymptotic Behavior of Magnetic Stripe Domain Arrays", *Phys. Rev. B*, vol. 87, no. 6, 060402(4), 2013. [Online]. Available: http://ro.uow.edu.au/cgi/viewcontent.cgi?article=1587%7B%5C&%7Dcontext=aiimpapers.

[91] A. P. Malozemoff and J. C. Slonczewski, *Magnetic Domain Walls in Bubble Materials*. Academic Press, 1979, p. 326, ISBN: 9780120029518. [Online]. Available: http://www.sciencedirect.com/science/book/9780120029518.

[92] F. Büttner, B. Krüger, S. Eisebitt, and M. Kläui, "Accurate Calculation of the Transverse Anisotropy of a Magnetic Domain Wall in Perpendicularly Magnetized Multilayers", *Physical Review B*, vol. 92, no. 5, p. 054 408, Aug. 2015, ISSN: 1098-0121. DOI: 10.1103/PhysRevB.92.054408. [Online]. Available: http://link.aps.org/doi/10.1103/PhysRevB.92.054408.

[93] H. J. G. Draaisma and W. J. M. De Jonge, "Magnetization Curves of Pd/Co Multilayers with Perpendicular Anisotropy", *Journal of Applied Physics*, vol. 621, no. 10, 1987. DOI: 10.1063/1.339345. [Online]. Available: http://dx.doi.org/10.1063/1.339345%20http://aip.scitation.org/toc/jap/62/8.

[94] S. U. Jen, Y. D. Yao, Y. T. Chen, J. M. Wu, C. C. Lee, T. L. Tsai, and Y. C. Chang, "Magnetic and Electrical Properties of Amorphous CoFeB Films", *Journal of Applied Physics*, vol. 99, no. 5, 053701(5), 2006. DOI: 10.1063/1.2174113ÍÎ. [Online]. Available: http://nthur.lib.nthu.edu.tw/bitstream/987654321/52265/1/2020301010006.pdf.

[95] Y.-T. Chen and C. Chang, "Effect of Grain Size on Magnetic and Nanomechanical Properties of Co_60Fe_20B_20 Thin Films", *Journal of Alloys and Compounds*, vol. 498, no. 2, pp. 113–117, 2010, ISSN: 09258388. DOI: 10.1016/j.jallcom.2010.03.141. [Online]. Available: http://www.sciencedirect.com/science/article/pii/S0925838810006468.

[96] M. A. Tagliente, A. Del Vecchio, L. Tapfer, C. Coccorese, L. Mercaldo, L. Maritato, J. M. Slaughter, and C. M. Falco, "Glancing-Incidence X-ray Characterization of Nb/Pd Multilayers", *Il Nuovo Cimento D*, vol. 19D, no. 2-4, pp. 473–480, 1997. [Online]. Available: https://link.springer.com/content/pdf/10.1007/BF03041007.pdf.

[97] C.-F. Pai, M. Mann, A. J. Tan, and G. S. D. Beach, "Determination of Spin Torque Efficiencies in Heterostructures with Perpendicular Magnetic Anisotropy",

PHYSICAL REVIEW B, vol. 93, no. 14, 144409(7), 2016. DOI: 10.1103/PhysRevB.93.144409. [Online]. Available: http://beach.mit.edu/wp-content/uploads/2016/07/PhysRevB.93.144409.pdf.

[98] P. P. J. Haazen, E. Murè, J. H. Franken, R. Lavrijsen, H. J. M. Swagten, and B. Koopmans, "Domain Wall Depinning Governed by the Spin Hall Effect", *Nature Materials*, vol. 12, no. 3553, pp. 299–303, 2013. DOI: 10.1038/NMAT3553. [Online]. Available: https://www.nature.com/nmat/journal/v12/n4/pdf/nmat3553.pdf.

[99] J. Cho, N.-H. Kim, S. Lee, J.-S. Kim, R. Lavrijsen, A. Solignac, Y. Yin, D.-S. Han, N. J. J. van Hoof, H. J. M. Swagten, B. Koopmans, and C.-Y. You, "Thickness Dependence of the Interfacial Dzyaloshinskii–Moriya Interaction in Inversion Symmetry Broken Systems", *Nature Communications*, vol. 6, p. 7635, Jul. 2015, ISSN: 2041-1723. DOI: 10.1038/ncomms8635. [Online]. Available: http://www.nature.com/doifinder/10.1038/ncomms8635.

[100] M. Bode, M. Heide, K. von Bergmann, P. Ferriani, S. Heinze, G. Bihlmayer, A. Kubetzka, O. Pietzsch, S. Blügel, and R. Wiesendanger, "Chiral Magnetic Order at Surfaces Driven by Inversion Asymmetry", *Nature*, vol. 447, no. 7141, pp. 190–193, May 2007, ISSN: 0028-0836. DOI: 10.1038/nature05802. [Online]. Available: http://www.ncbi.nlm.nih.gov/pubmed/17495922%20http://www.nature.com/doifinder/10.1038/nature05802.

[101] S. Emori, D. C. Bono, and G. S. D. Beach, "Interfacial Current-Induced Torques in Pt/Co/GdOx", *Applied Physics Letters*, vol. 101, no. 4, 042405(4), 2012, ISSN: 00036951. DOI: 10.1063/1.4737899. [Online]. Available: http://scitation.aip.org/content/aip/journal/apl/101/4/10.1063/1.4737899.

[102] P. Eames and E. D. Dahlberg, "Characterization of Domain States in Submicron Sized Permalloy Particles with Perpendicular Anisotropy", *Journal of Applied Physics*, vol. 91, no. 10, pp. 7986–7988, 2002, ISSN: 00218979. DOI:

10.1063/1.1453319. [Online]. Available: http://scitation.aip.org/content/aip/journal/jap/91/10/10.1063/1.1453319.

[103] M. Hehn, K. Ounadjela, J.-P. Bucher, F. Rousseaux, D. Decanini, B. Bartenlian, and C. Chappert, "Nanoscale Magnetic Domains in Mesoscopic Magnets", *Science*, vol. 272, no. 5269, pp. 1782–1785, 1996. [Online]. Available: http://science.sciencemag.org/content/272/5269/1782/tab-pdf.

[104] C. Haginoya, S. Heike, M. Ishibashi, K. Nakamura, K. Koike, T. Yoshimura, J. Yamamoto, and Y. Hirayama, "Magnetic Nanoparticle Array with Perpendicular Crystal Magnetic Anisotropy", *Journal of Applied Physics*, vol. 85, no. 12, pp. 8327–8331, 1999. DOI: 10.1063/1.370678. [Online]. Available: http://dx.doi.org/10.1063/1.370678%20http://aip.scitation.org/toc/jap/85/12.

[105] M. Haast, J. Schuurhuis, L. Abelmann, J. Lodder, and T. Popma, "Reversal Mechanism of Submicron Patterned CoNi/Pt Multilayers", *IEEE Transactions on Magnetics*, vol. 34, no. 4, pp. 1006–1008, Jul. 1998, ISSN: 00189464. DOI: 10.1109/20.706339. [Online]. Available: http://ieeexplore.ieee.org/document/706339/.

[106] A. Fernandez, P. Bedrossian, S. Baker, S. Vernon, and D. Kania, "Magnetic Force Microscopy of Single-Domain Cobalt Dots Patterned Using Interference Lithography", *IEEE Transactions on Magnetics*, vol. 32, no. 5, pp. 4472–4474, 1996, ISSN: 00189464. DOI: 10.1109/20.538901. [Online]. Available: http://ieeexplore.ieee.org/document/538901/.

[107] C. Jin, Z.-A. Li, A. Kovács, J. Caron, F. Zheng, F. N. Rybakov, N. S. Kiselev, H. Du, S. Blügel, M. Tian, Y. Zhang, M. Farle, and R. E. Dunin-Borkowski, "Control of Morphology and Formation of Highly Geometrically Confined Magnetic Skyrmions", *Nature Communications*, vol. 8, 15569(9), 2017. DOI: 10.1038/ncomms15569. [Online]. Available: https://www.nature.com/articles/ncomms15569.pdf.

[108] R. Juge, S.-G. Je, D. d. S. Chaves, S. Pizzini, L. D. Buda-Prejbeanu, L. Aballe, M. Foerster, A. Locatelli, T. O. Menteş, A. Sala, F. Maccherozzi, S. S. Dhesi, S. Auffret, G. Gaudin, J. Vogel, and O. Boulle, "Magnetic Skyrmions in Confined Geometries : Effect of the Magnetic Field and the Disorder", *arXiv preprint arXiv: 1706.01726*, Jun. 2017. arXiv: 1706.01726. [Online]. Available: http://arxiv.org/abs/1706.01726.

[109] N. Romming, A. Kubetzka, C. Hanneken, K. von Bergmann, and R. Wiesendanger, "Field-dependent Size and Shape of Single Magnetic Skyrmions", *Physical review letters*, vol. 114, no. 17, 177203(5), May 2015, ISSN: 1079-7114. DOI: 10.1103/PhysRevLett.114.177203. [Online]. Available: http://www.ncbi.nlm.nih.gov/pubmed/25978258%20https://link.aps.org/doi/10.1103/PhysRevLett.114.177203.

[110] C. Mack, "The Multiple Lives of Moore's Law", *IEEE Spectrum*, vol. 52, no. 4, pp. 31–37, Apr. 2015, ISSN: 0018-9235. DOI: 10.1109/MSPEC.2015.7065415. [Online]. Available: http://ieeexplore.ieee.org/document/7065415/.

[111] S. V. Garimella, A. S. Fleischer, J. Y. Murthy, A. Keshavarzi, R. Prasher, C. Patel, S. H. Bhavnani, R. Venkatasubramanian, R. Mahajan, Y. Joshi, B. Sammakia, B. A. Myers, L. Chorosinski, M. Baelmans, P. Sathyamurthy, and P. E. Raad, "Thermal Challenges in Next-Generation Electronic Systems", *IEEE Transactions on Components and Packaging Technologies*, vol. 31, no. 4, pp. 801–815, Dec. 2008, ISSN: 1521-3331. DOI: 10.1109/TCAPT.2008.2001197. [Online]. Available: http://ieeexplore.ieee.org/document/4675673/.

[112] A. Hoffmann and S. D. Bader, "Opportunities at the Frontiers of Spintronics", *Physical Review Applied*, vol. 4, no. 4, 047001(18), 2015. DOI: 10.1103/PhysRevApplied.4.047001. [Online]. Available: https://journals.aps.org/prapplied/pdf/10.1103/PhysRevApplied.4.047001.

[113] R. Tomasello, E. Martinez, R. Zivieri, L. Torres, M. Carpentieri, and G. Finocchio, "A strategy for the Design of Skyrmion Racetrack Memories", *Scientific*

Reports, vol. 4, p. 6784, Oct. 2014, ISSN: 2045-2322. DOI: 10.1038/srep06784. [Online]. Available: http://www.nature.com/articles/srep06784.

[114] W. Kang, Y. Huang, C. Zheng, W. Lv, N. Lei, Y. Zhang, X. Zhang, Y. Zhou, and W. Zhao, "Voltage Controlled Magnetic Skyrmion Motion for Racetrack Memory", *Scientific Reports*, vol. 6, no. 23164, pp. 1–11, 2016. DOI: 10.1038/srep23164. [Online]. Available: https://www.nature.com/articles/srep23164.pdf.

[115] W. Koshibae, Y. Kaneko, J. Iwasaki, M. Kawasaki, Y. Tokura, and N. Nagaosa, "Memory Functions of Magnetic Skyrmions", *Japanese Journal of Applied Physics*, vol. 54, no. 5, 053001(8), May 2015, ISSN: 0021-4922. DOI: 10.7567/JJAP.54.053001. [Online]. Available: http://stacks.iop.org/1347-4065/54/i=5/a=053001?key=crossref.090e0ea92e08e49bfdded76a54e9ff48.

[116] C. Wang, D. Xiao, X. Zhang, J. Müller, J. Xia, X. Liu, and Y. Zhou, "Motion of Skyrmions in Nanowires Driven by Magnonic Momentum-Transfer Forces", *New Journal of Physics*, vol. 19, 065001(10), 2017. [Online]. Available: http://iopscience.iop.org/1367-2630/19/6/065001.

[117] W. Legrand, D. Maccariello, N. Reyren, K. Garcia, C. Moutafis, C. Moreau-Luchaire, S. Collin, K. Bouzehouane, V. Cros, and A. Fert, "Room-Temperature Current-Induced Generation and Motion of sub-100 nm Skyrmions", *Nano Letters*, vol. 17, no. 4, pp. 2703–2712, Apr. 2017, ISSN: 1530-6984. DOI: 10.1021/acs.nanolett.7b00649. [Online]. Available: http://pubs.acs.org/doi/abs/10.1021/acs.nanolett.7b00649.

[118] F. Büttner, I. Lemesh, and G. S. D. Beach, "Full Phase Diagram of Isolated Skyrmions in a Ferromagnet", *arXiv preprint arXiv:1704.08489*, Apr. 2017. arXiv: 1704.08489. [Online]. Available: http://arxiv.org/abs/1704.08489.

[119] A. De Lucia, K. Litzius, B. Krüger, O. A. Tretiakov, and M. Kläui, "Multiscale Simulations of Topological Transformations in Magnetic Skyrmions", *arXiv preprint arXiv: 1702.05767v1*, Feb. 2017. DOI: 10.1103/PhysRevB.96.020405.

arXiv: 1702.05767. [Online]. Available: http://arxiv.org/abs/1702.05767%20http://dx.doi.org/10.1103/PhysRevB.96.020405.

[120] S. K. Kim, K.-J. Lee, and Y. Tserkovnyak, "Self-Focusing Skyrmion Racetracks in Ferrimagnets", *PHYSICAL REVIEW B*, vol. 95, no. 14, 140404(5), 2017. DOI: 10.1103/PhysRevB.95.140404. [Online]. Available: https://journals.aps.org/prb/pdf/10.1103/PhysRevB.95.140404.

[121] X. Zhang, Y. Zhou, and M. Ezawa, "Antiferromagnetic Skyrmion: Stability, Creation and Manipulation", *Scientific Reports*, vol. 6, no. 24795, pp. 1–8, 2016. DOI: 10.1038/srep24795. [Online]. Available: https://www.nature.com/articles/srep24795.pdf.

[122] K. Ueda, M. Mann, C.-F. Pai, A.-J. Tan, and G. S. D. Beach, "Spin-Orbit Torques in Ta/TbxCo100-x Ferrimagnetic Alloy Films with Bulk Perpendicular Magnetic Anisotropy", *Applied Physics Letters*, vol. 109, no. 23, 232403(5), Dec. 2016, ISSN: 0003-6951. DOI: 10.1063/1.4971393. [Online]. Available: http://aip.scitation.org/doi/10.1063/1.4971393.

[123] C. O. Avci, A. Quindeau, M. Mann, C.-F. Pai, C. A. Ross, and G. S. D. Beach, "Spin Transport in As-Grown and Annealed Thulium Iron Garnet/Platinum Bilayers with Perpendicular Magnetic Anisotropy", *Physical Review B*, vol. 95, no. 11, 115428(9), Mar. 2017, ISSN: 2469-9950. DOI: 10.1103/PhysRevB.95.115428. [Online]. Available: https://link.aps.org/doi/10.1103/PhysRevB.95.115428.

[124] A. B. Shick, S. Khmelevskyi, O. N. Mryasov, J. Wunderlich, and T. Jungwirth, "Spin-Orbit Coupling Induced Anisotropy Effects in Bimetallic Antiferromagnets: A Route Towards Antiferromagnetic Spintronics", *Physical Review B*, vol. 81, no. 21, 212409(4), Jun. 2010, ISSN: 1098-0121. DOI: 10.1103/PhysRevB.81.212409. [Online]. Available: http://link.aps.org/doi/10.1103/PhysRevB.81.212409%20https://link.aps.org/doi/10.1103/PhysRevB.81.212409.